Illinois Water Resources Center
Annual Technical Report
FY 2016

Introduction

In 2016, the Illinois Water Resources Center secured over $2.5 million in base and leveraged funding to work on water resources issues in Illinois. Leveraged funds include an award from US EPA to conduct research and Extension throughout the Great Lakes on projects such as nutrient loss mitigation, community support for sediment remediation projects, Great Lakes monitoring and research integration, and emerging contaminants research and outreach. Other leveraged funding includes assistance to private wellowners, small water supply operators, the State of Illinois for its nutrient loss reduction efforts, and several research projects that connect university researchers to USGS scientists.

Research Program Introduction

IWRC research resulted in many findings. Two of the most notable are:

Michael Lydy's 104G project offers compelling evidence that pyrethroid contamination is an important source of toxicity to sediments-dwelling organism in urban streams.

Bruce Rhoads and Quinn Lewis, University of Illinois, found that Large-Scale Particle Image Velocimetry velocity fields are an important complement to traditional river flow velocity measurements especially in complex flows, and cameras deployed both in fixed and UAS configurations can yield rapid, accurate mean flow and discharge measurements in a variety of field conditions.

Improving Morphodynamic Predictions in Rivers

Basic Information

Title:	Improving Morphodynamic Predictions in Rivers
Project Number:	2014IL292S
USGS Grant Number:	
Sponsoring Agency:	USGS
Start Date:	8/16/2015
End Date:	8/15/2016
Funding Source:	104S
Congressional District:	IL-015
Research Category:	Climate and Hydrologic Processes
Focus Category:	Models, Geomorphological Processes, Solute Transport
Descriptors:	None
Principal Investigators:	Gary Parker

Publications

There are no publications.

Numerical simulation of large-scale bedload particle tracer advection-dispersion in rivers with free bars

Toshiki IWASAKI[1,2], Jonathan NELSON[2], Yasuyuki SHIMIZU[3] and Gary PARKER[1,4]

[1]Department of Civil and Environmental Engineering, University of Illinois at Urbana-Champaign, 205 N Mathews Avenue, Urbana, Illinois, 61801, USA

[2]U.S. Geological Survey, Geomorphology and Sediment Transport Laboratory, Golden, Colorado, 80403, USA

[3]Laboratory of Hydraulic Research, Graduate School of Engineering, Hokkaido University, N13, W8, Kita-ku, Sapporo, 0608628, Japan

[4]Department of Geology, University of Illinois at Urbana-Champaign, 156 Computing App. Bldg., 605 E. Springfield Avenue, Champaign, Illinois, 61820, USA

*Corresponding author: Toshiki IWASAKI, toshia413@gmail.com

Key points:

- Tracer pebbles both advect and disperse over a plane, mobile bed, but the dispersion rate is dramatically increased by the alternate bars
- We show how the scour and fill associated with alternate bars achieves this asymptotic bedload tracer advection-dispersion

ABSTRACT

Asymptotic characteristics of the transport of bedload tracer particles in rivers have been described by advection-dispersion equations. Here we perform numerical simulations designed to study the role of free bars, and more specifically single-row alternate bars, on streamwise tracer particle dispersion. In treating the conservation of tracer particle mass, we use two alternative formulations for the Exner equation of sediment mass conservation; the flux-based formulation, in which bed elevation varies with the divergence of the bedload transport rate, and the entrainment-based formulation, in which bed elevation changes with the net deposition rate. Under the condition of no net bed aggradation/degradation, a 1D flux-based deterministic model that does not describe free bars yields no streamwise dispersion. The entrainment-based 1D formulation, on the other hand, models stochasticity via the PDF of particle step length, and as a result does show tracer dispersion. When the formulation is generalized to 2D to include free alternate bars, however, both models yield almost identical asymptotic advection-dispersion characteristics, in which streamwise dispersion is dominated by randomness inherent in free bar morphodynamics. This randomness can result in a heavy-tailed PDF of waiting time. In addition, migrating bars may constrain the travel distance through temporary burial, causing a thin-tailed PDF of travel distance. The superdiffusive character of streamwise particle dispersion predicted by the model is attributable to the interaction of these two effects.

57

58 **Index terms:**

59 0744 Rivers, 1825 Geomorphology: fluvial, 1862 Sediment transport

60

61 **Keywords:**

62 bedload tracers, advection-dispersion, free single-row alternate bars, normal dispersion,

63 anomalous dispersion

64

65

66

67

68

69

70

71

72

73

74

1. INTRODUCTION

An understanding of the detailed mechanisms of bedload transport is of central importance for elucidating a wide spectrum of morphodynamic processes in rivers [e.g., *Einstein*, 1937; *Meyer, Peter and Müller*, 1948; *Nakagawa and Tsujimoto*, 1978; *Ashida and Michiue*, 1972; *Kovacs and Parker*, 1994; *Parker et al.*, 2000; *Seminara et al.*, 2002; *Parker et al.*, 2003; *Ancey*, 2010; *Furbish et al.*, 2010; *Schmeeckle*, 2015], as well as the fate of sediment-bound substances such as nutrients, metals, and radionuclides in river systems [e.g., *Falkowska and Falkowski*, 2015; *Iwasaki et al.*, 2015]. Tracer particles that are distinguishable from the ambient bed sediment only via passive markers that do not affect transport dynamics (e.g. color, magnetic properties, radioisotope signature, etc.) have been widely used to measure and quantify bedload transport. The tracking of tracer particles that are initially deployed on the bed surface provides data regarding temporal and spatial changes in tracer distribution [*Sayre and Hubbell*, 1965; *Hoey*, 1996], and gives insight into characteristics of bedload transport, such as travel distance and waiting time distribution [*Einstein*, 1937; *Ferguson and Hoey*, 2002; *Pyrce and Ashmore*, 2003; *Wong et al.*, 2007; *Martin et al.*, 2012; *Roseberry et al.*, 2012; *Hassan et al.*, 2013; *Haschenburger*, 2013]. Such measurements have shown that tracers advect downstream, and disperse in space in the streamwise, transverse and vertical directions. The collective asymptotic behavior of tracers has been described in terms of advection-dispersion. An understanding of this advection-dispersion allows better understanding of bedload transport itself and

97 associated bed morphodynamics and is central to the estimation of how fast and far
98 sediment-bound substances can be transported.

99 *Einstein* [1937] first treated the bedload transport phenomenon as a stochastic
100 process using the statistical characteristics of bedload, i.e., travel distance and waiting
101 time. These statistical quantities are key factors for modeling the streamwise
102 advection-dispersion of bedload tracers. *Einstein* [1937] suggested an exponential
103 distribution of travel distance and waiting time based on experiments. In the context of
104 a random walk model, thin-tailed PDF's of travel distance and waiting time
105 asymptotically results in normal advection-dispersion [*Schumer et al.*, 2009; *Ganti et*
106 *al.*, 2010], according to which the streamwise standard deviation σ of an ensemble of
107 tracers increases as $t^{1/2}$, where t denotes time. However, recent detailed measurements
108 of tracers in experiments and field studies have suggested the possibility of
109 heavy-tailed PDF's for step length and waiting time (e.g. power distributions) that, for
110 example, do not have finite second moments. This can lead anomalous dispersion
111 instead of normal dispersion, leading to faster (superdiffusive, i.e. $\sigma \sim t^{\gamma}$, where $\gamma >$
112 1/2) or slower (subdiffusive, i.e. $\gamma <$ 1/2) dispersion of tracers than normal dispersion
113 [*Schumer et al.*, 2009; *Bradley et al.*, 2010; *Ganti et al.*, 2010; *Zhang et al.*, 2012].
114 Since differences in the dispersion rate are critical to a full understanding of bedload
115 transport and subsequent bedload-bound substances dispersal in rivers, there has been
116 a long debate as to what factors control travel distance, waiting time distribution and
117 the associated characteristics of tracer advection-dispersion.

118 Several experimental, numerical, and field studies have been performed to address

119 these issues. These studies have yielded, however, different results for travel distance
120 and waiting time, and therefore different dispersion features. This is in part because of
121 differences in the temporal and spatial scales considered. *Nikora et al.* [2002]
122 proposed a framework to describe tracer dispersion regime over a broad range of
123 temporal and spatial scales, suggesting three diffusive regimes for bedload particles,
124 i.e. local (ballistic diffusion), intermediate (normal or superdiffusion), and global
125 (subdiffusion) regimes. Although this framework needs to be validated based on
126 several datasets, it is novel in that it suggests that scale dependency is a dominant
127 mechanism controlling the characteristics of bedload transport. In their model, the
128 local regime explains bedload motion due to the collision of two particles, and the
129 intermediate regime describes bedload transport within at least two successive rests.
130 This indicates that the diffusive mechanisms at these scales might be related to
131 microscopic (particle scale) phenomena such as particle-particle or particle-bed
132 interactions, as well as turbulent structures in the flow near the bed surface. Recent
133 advances in measurement techniques [e.g., *Roseberry et al.*, 2012; *Campagnol et al.*,
134 2015] and computational technologies using highly resolved detailed physically-based
135 numerical models [e.g., *Schmeeckle*, 2014, 2015] have contributed to a comprehensive
136 understanding of the bedload transport phenomena at these scales. Conversely, the
137 global regime is associated with a large collection of particle motions at the
138 intermediate regime, so that this regime represents particle behaviors associated with
139 tens to millions of steps and rests. As a consequence, the dominant diffusive
140 mechanisms at the global scale are more complex; in addition to particle-scale
141 phenomena, the complexity of the system associated with the bed and planform

142 morphology and morphodynamics, sediment composition, and unsteady flow regimes
143 in rivers all affect tracer behavior. Because of this, the scale dependence of the
144 dominant diffusive mechanism is poorly understood. An understanding of streamwise
145 tracer dispersion at the global scale remains one of the challenges in the field of
146 geomorphology and river engineering.

147 Dynamic measurements of large-scale bedload motions are required in order to
148 understand the characteristics of bedload transport at the global scale [*Hassan et al.*,
149 2013]. However, detailed measurements of particle motion with sufficient temporal
150 and spatial resolution are still limited to experimental scales [*Lajeunesse et al.*, 2010;
151 *Roseberry et al.*, 2012; *Campagnol et al.*, 2015]. Alternative advanced methods, such
152 as accelerometer-embedded cobble tracers [*Olinde and Johnson*, 2015] are necessary
153 at field scale. In general, measurable quantification of tracer behavior at field scale
154 correspond to cumulative quantities evaluated over specified durations. These
155 quantities and their statistical features are strongly affected by a larger variety of
156 physical mechanisms than those at intermediate scale. For instance, *Philips et al.*
157 [2013] and *Olinde and Johnson* [2015] measured long-term and large-scale tracer
158 behaviors using active and passive tracer techniques under the influence of unsteady
159 flows. The results showed a thin-tailed travel distance and heavy-tailed waiting time,
160 suggesting superdiffusive dispersion. Effects of graded sediment, in which each
161 particle size has different mobility, result in more complex patterns of total grain
162 displacement [e.g., *Hashenburger*, 2013], resulting in anomalous dispersion of the
163 grain size mixture even when each grain size range disperses normally [*Ganti et al.*,
164 2010] and significant streamwise advective slowdown of tracers [*Ferguson and Hoey*,

165 2002]. Among the many relevant factors affecting tracer transport, however, bed
166 surface morphology and its dynamics are likely to be the most important. Bed
167 morphology is the main factor affecting storage of sediments in rivers, so this strongly
168 affects the waiting time characteristics [*Hashenburger*, 2013]. Moreover, large-scale
169 bedforms and planform features (i.e., dunes, bars, meandering) constrain the length
170 scale of bedload motion [*Pyrce and Ashmore*, 2003, 2005; *Kasprak et al.*, 2015], thus
171 controlling cumulative travel distance. Analysis by *Hassan et al.* [2013] of large field
172 measurement datasets regarding tracer transport in several rivers have indicated that
173 bed geometry impacts travel distance more significantly than flow regime. The same
174 authors also showed that the PDF of travel distance is likely to be thin-tailed rather
175 than heavy-tailed because of separate transport events during multiple floods. In
176 addition to the effect of bed geometry, dynamic morphological changes of the bed
177 surface cause vertical mixing of bedload particles [*Hassan and Church*, 1994; *Parker*
178 *et al.*, 2000; *Ferguson and Hoey*, 2002; *Blom and Parker*, 2004; *Wong et al.*, 2007;
179 *Blom et al.*, 2008], which complicates the pattern of overall tracer transport and
180 dispersal. Bedload transport at the global scale, therefore, is a multi-scale phenomenon
181 associated with the complexity of the system at a broad range of temporal and spatial
182 scales, rendering the identification of a single dominant mechanism of tracer
183 advection-dispersion problematic. Field measurements often fail to provide the
184 instantaneous location of all tracers, because some of tracers are lost via deep burial or
185 leave the reach of interest. These limitations to field studies makes this large-scale and
186 long-term phenomenon difficult to understand. In small-scale experimental flumes on
187 the other hand, we can measure detailed flow structures, tracer dispersal, and

188 morphodynamics under well-controlled conditions, but the inherent limitation on
189 spatial scale places a severe constraint on the understanding of dispersal at a global
190 scale.

191 Numerical models are powerful tools used to overcome these limitations. Because
192 bedload tracer transport can be treated as a random process, simple stochastic models
193 (e.g., Markov process, random walk model) have been proposed to capture the
194 horizontal and vertical mixing of tracers [*Sayre and Hubbell*, 1965; *Yang and Sayre*,
195 1971; *Hassan and Church*, 1994; *Ferguson and Hoey*, 2002; *Schumer et al.*, 2009].
196 Physically based models that include the origin of this stochasticity, for instance, the
197 probability of bed surface fluctuation, entrainment, and deposition [*Parker et al.*,
198 2000; *Ancey*, 2010; *Pelosi et al.*, 2014; *Pelosi et al.*, 2016]; the irregularity of bedform
199 dimensions [*Blom and Parker*, 2004]; and the velocity variability of bedload particles
200 [*Furbish et al.*, 2012], have led to the derivation of master equations describing tracer
201 dispersal. A key question for each of these approaches is how to model the
202 stochasticity of bedload motion under the influence of physical phenomena such as
203 bedforms and planform variation. On the other hand, recent advances in numerical
204 modeling have made it possible to directly resolve complex phenomena such as bars.
205 In particular, the modeling framework for reproducing reach-scale morphological
206 changes of bed surfaces such as bars, meandering and braiding, have been well
207 documented in the literature, and a variety of numerical models that capture
208 morphodynamic complexity are now available publicly such as Delft3D
209 (http://www.deltares.nl) [e.g., *Lesser et al.*, 2004], TELEMAC
210 (http://www.opentelemac.org) [e.g., *Langendoen et al.*, 2016], iRIC

211 (http://www.i-ric.org) [*Nelson et al.*, 2016]. A coupled model that includes a
212 sophisticated morphodynamic submodel such as one of the above and a tracer
213 transport submodel may capture the physics of long-term and large-scale tracer
214 behavior under the influence of complex bed geometry and its morphological change,
215 so yielding new insight into advection-dispersion characteristics at the global scale. As
216 far as we know, however no numerical models have been proposed for capturing tracer
217 advection-dispersion under the influence of complex bed morphodynamics generated
218 within the model itself.

219 Here we present a first step toward combining a submodel that captures self-formed
220 morphodynamic complexity at global scale with two alternative submodels that
221 describe tracer dispersal. Our morphodynamic model captures self-formed free
222 alternate bars at field scale, as earlier described by e.g. *Tubino et al.* [1999], that is,
223 under typical reach-scale dynamic bed morphodynamics in rivers. We adopt two
224 different submodels describing sediment tracer conservation: a flux-based model and
225 an entrainment-based model [*Parker et al.*, 2000]. Our bedload transport model
226 employ captures the tracer behavior induced by bedload motion (intermediate regime),
227 and the combination of the tracer conservation and morphodyamic submodels directly
228 resolve large-scale tracer transport associated with mutual interactions among flow,
229 bedload, and free bar dynamics (global regime).

230 In this paper, we 1) illustrate how the flux- and entrainment-based tracer
231 conservation models affect tracer advection-dispersion, 2) describe effects of dynamic
232 bed evolution associated with migrating free bars on large-scale tracer

advection-dispersion, and 3) quantify dominant mechanisms controlling asymptotic tracer dispersion features under the influence of free bars. This is a first attempt to explicitly resolve the effects of dynamic bed evolutions on tracer advection-dispersion at global scales.

2. MODEL

The numerical model used in this study consists of a morphodynamic module and a tracer transport module. A key element of these modules is the treatment of bedload transport; this determines the tracer advection-dispersion associated with the bedload, as well as how bedload transport affects free bar dynamics. Two different formulations have been proposed to handle sediment conservation under the condition of bedload transport, i.e. a flux-based model and an entrainment-based model [*Parker et al.*, 2000]. Below, we address how these models describe tracer transport.

2.1 Flux- and entrainment-based models: Tracer advection-dispersion

Exner [1925] proposed the first morphodynamic model that takes into account morphological changes of the bed surface associated with bedload transport. A 1D version of the model, which corresponds to sediment mass conservation, can be written as:

253 $$\frac{\partial \eta}{\partial t} + \frac{1}{1-\lambda_p}\frac{\partial q_b}{\partial x} = 0, \quad (1)$$

254 where t is time, x is the streamwise coordinate, η is the bed surface elevation, q_b is the
255 volume bedload transport rate per unit width, and λ_p is the porosity of bed. (In the
256 above form, the model described sediment volume conservation; this translates to
257 sediment mass conservation assuming that the sediment has constant density.) This
258 model treats bedload transport in terms of the differential flux of sediment volume
259 parallel to the bed. The divergence of the flux drives bed elevation change. This
260 classical flux-based model for sediment conservation [e.g. *Parker et al.*, 2000] is the
261 most common one used in morphodynamic calculations, and has been widely applied
262 within mathematical and numerical models to describe fluvial and related processes on
263 the Earth's surface. The flux-based, however, is limited in its ability to handle the
264 dispersion of bedload tracers, because the bedload transport rate q_b inherently
265 represents a bulk average that does not account for stochastic variations.

266 Here we show that this limitation precludes the quantification of tracer dispersion in
267 a simple 1D model. By introducing an active layer model [*Hirano*, 1971], we can
268 obtain a flux-based relation for the conservation of tracer volume that corresponds
269 precisely to Eq. (1) [*Parker et al.*, 2000]:

270 $$L_a \frac{\partial f_a}{\partial t} + f_I \frac{\partial \eta}{\partial t} + \frac{1}{1-\lambda_p}\frac{\partial q_b f_a}{\partial x} = 0, \quad (2)$$

271 where f_a is the fraction of tracers in the active layer, L_a is the active layer thickness,
272 and f_I is the fraction of tracers exchanged at the interface between the active layer and

273 the substrate as the bed aggrades or degrades. This fraction is given by the following
274 relation:

275 $$f_I = \begin{cases} f_a & , \quad \dfrac{\partial \eta}{\partial t} > 0 \\ f_t & , \quad \dfrac{\partial \eta}{\partial t} < 0 \end{cases}, \tag{3}$$

276 where f_t is the fraction of tracers in the substrate at the interface between the active
277 layer and the substrate. The second and third terms on left-hand side of Eq. (2)
278 represent the exchange of tracers between the active layer and the substrate as a result
279 of bed elevation change and volumetric gradient in the bedload flux of tracers
280 respectively. Experiments have demonstrated that tracers in the bedload disperse by
281 stochastic motion, even under the condition of dynamic equilibrium of the bed surface
282 (i.e., $\partial \eta / \partial t = 0$) [e.g., *Wong et al.*, 2007; *Martin et al.*, 2013]. This dispersion,
283 however, cannot be captured by Eq. (2), because it reduces precise to the kinematic
284 wave equation with no diffusive term at dynamic equilibrium:

285 $$\frac{\partial f_a}{\partial t} + \frac{q_b}{L_a\left(1-\lambda_p\right)} \frac{\partial f_a}{\partial x} = 0. \tag{4}$$

286 The classic flux-based model thus cannot explain tracer dispersion.

287 Several attempts have been made to include stochastic behavior of particles moving
288 as bedload into morphodynamic models [e.g., *Einstein*, 1937; *Nakagawa and*
289 *Tsujimoto*, 1980; *Parker et al*., 2000; *Ancey*, 2010; *Furbish et al.*, 2012; *Bohorquez*
290 *and Ancey*, 2015]. This has most commonly been done in terms of an
291 entrainment-based form for the Exner equation of sediment conservation:

$$\frac{\partial \eta}{\partial t} = \frac{1}{1-\lambda_p}\left(D - E\right), \tag{5}$$

where E is the volumetric entrainment rate of sediment per unit bed area into the bedload, and D is the volumetric deposition rate of sediment per unit area onto the bed. In this model framework, an imbalance of the vertical flux of sediment volume between the bedload and the substrate causes bed elevation change. Stochastic behavior is brought into the model in terms of the deposition rate. A particle entrained into the bedload is assumed to travel a distance, i.e. step length r before depositing again, where r is assumed to be a random variable with PDF $f_p(r)$. The deposition rate $D(x)$ is then given as:

$$D\left(x\right) = \int_0^\infty E\left(x-r\right) f_p\left(r\right) dr. \tag{6}$$

The corresponding relation for conservation of tracers can be written as follows [*Parker et al.*, 2000]:

$$\left(1-\lambda_p\right)\left(L_a \frac{\partial f_a}{\partial t} + f_I \frac{\partial \eta}{\partial t}\right) = \int_0^\infty f_a\left(x-r\right) E\left(x-r\right) f_p\left(r\right) dr - f_a\left(x\right) E\left(x\right). \tag{7}$$

At dynamic equilibrium, i.e. $\partial\eta/\partial t = 0$, this relation reduces to:

$$\left(1-\lambda_p\right)\frac{L_a}{E}\frac{\partial f_a}{\partial t} = \int_0^\infty f_a\left(x-r\right) f_p\left(r\right) dr - f_a\left(x\right). \tag{8}$$

Taylor expanding for $f_a(x\text{-}r)$ in Eq. (8) and dropping terms higher than 2nd order term yields:

$$\left(1-\lambda_p\right)\frac{L_a}{E}\frac{\partial f_a}{\partial t}=-\mu_1\frac{\partial f_a}{\partial x}+\frac{\mu_2}{2}\frac{\partial^2 f_a}{\partial x^2}, \tag{9}$$

where μ_1 and μ_2 are the first and second moments of the step length PDF, respectively. In the case of an exponential (thin-tailed) PDF for step length [e.g., *Nakagawa and Tsujimoto*, 1980], i.e.:

$$f_p\left(r\right)=\frac{1}{L_s}\exp\left(-\frac{r}{L_s}\right), \tag{10}$$

it is found that μ_1 and μ_2 take the values L_s and $2L_s^2$, respectively, in which L_s denotes the mean step length. At dynamic equilibrium, the bedload transport rate is given by the following relation [*Nakagawa and Tsujimoto*, 1980]:

$$q_b = EL_s. \tag{11}$$

Consequently, Eq. (9) reduces as follows at dynamic equilibrium:

$$\frac{\partial f_a}{\partial t}+\frac{q_b}{L_a\left(1-\lambda_p\right)}\frac{\partial f_a}{\partial x}=\frac{q_b L_s}{L_a\left(1-\lambda_p\right)}\frac{\partial^2 f_a}{\partial x^2}. \tag{12}$$

As opposed to the flux-based kinematic wave equation corresponding to Eq. (4), Eq. (12) is an advection-diffusion equation, so demonstrating that the entrainment-based model does indeed describe the dispersion of tracers associated with bedload transport [*Ganti et al.*, 2010; *Lajeunesse et al.*, 2013]. The scale of step length is intermediate in the sense of *Nikora et al.* [2002], so the diffusion effect in Eq. (12) may be related to dispersion at the intermediate scale.

2.2 Model framework and numerical technique

Here we couple the Exner relations for morphodynamics and tracer conservation with an unsteady shallow water flow model. The model we use, which can be implemented in both 1D and 2D models is essentially the same as *Jang and Shimizu* [2005], to which we refer the reader for details. The Manning roughness closure is used to evaluate the bed shear stress. The governing equations are discretized on a staggered grid system based on a finite difference scheme. The momentum equations of the flow model are decomposed into advective and non-advective terms that include the pressure and roughness terms, and the continuity equation of water and the non-advective terms are solved implicitly by an iterative method. The flow velocities predicted in this way are then updated using the advection terms with the Constrained Interpolation Profile (CIP) method to minimize numerical diffusion [*Yabe et al.*, 1991].

In the entrainment-based model, we evaluated the local entrainment rate from the following relation based on Eq. (11);

$$E = \frac{q_{be}}{L_s}, \tag{13}$$

where q_{be} is the local bedload transport rate that would prevail were it to be in equilibrium with the local bed shear stress (as is assumed in the flux-based model). We further computed q_{be} from the Meyer-Peter and Müller formula [*Meyer, Peter and Muller*, 1948]. The effect of transverse bed slope on bedload is taken into account using the linearized formula proposed by *Hasegawa* [1981] (see also *Kovacs and Parker* [1994] and *Parker et al.* [2003] for fully nonlinearized formulations). The

348 effect of secondary flow on the bedload transport direction is neglected herein for
349 simplicity, since it plays only a minor role in free bar dynamics in a straight channel at
350 the nonlinear level. The divergence of the bedload fluxes yields bed elevation changes
351 for the flux-based model. In addition, the vector field of the bedload flux is used to
352 calculate the trajectory of the bedload particles in the entrainment-based model. In a
353 1D model, a single bedload step is directed downstream. In a 2D model, however, the
354 trajectory of a step is described by a 2D path. The appropriate trajectories are most
355 easily described in terms of what might be called "bedload streamlines" (in analogy to
356 flow streamlines), along which the path is everywhere parallel to the local bedload
357 vector. The model framework and detailed numerical procedures used to discretize the
358 entrainment-based model are presented in Appendix A.

359 To reduce the computational cost of simulating long-term morphological changes of
360 free bars and the associated pattern of asymptotic tracer advection-dispersion, we
361 introduce a morphological factor that accelerates bed evolution changes. This
362 numerical parameter, as defined in e.g. *Roelvink* [2006], *Nabi et al.* [2013a], and
363 *Schuurman et al.* [2016] does not play a critical role in the governing bed
364 morphodynamic processes as long as it is not too large. We set this parameter as 5,
365 which is reasonable for free bar simulations [*Crosato et al*., 2011; *Schuurman et al.*,
366 2013; *Duro et al.*, 2016].

367 A constant discharge and a corresponding bedload supply necessary to maintain the
368 elevation of the upstream end set in the initial conditions are imposed at the upstream
369 boundary. Numerical models generally need a perturbation as a trigger for the

370 inception of free bars [e.g., *Defina*, 2003]. In addition, to get continuous bar inception,
371 the perturbation needs to be maintained over the entire calculation [*Federici and*
372 *Seminara*, 2003]. In this study, we maintain a small perturbation with a random
373 transverse distribution into the water discharge at the upstream end. Free flux
374 boundary conditions for both flow and bedload are employed at the downstream
375 boundary. The sidewall boundary conditions are set those of vanishing transverse flux
376 of water and bedload.

377 As mentioned in the model explanation, the flux-based model does not yield a
378 diffusion term for tracer transport for the case of dynamic equilibrium. However, since
379 the governing equation of tracer volumetric conservation in the active layer (i.e., Eq.
380 (2)) is a pure advection equation, an inappropriate numerical scheme will yield
381 numerical diffusion. For example, a low order scheme (e.g., first order upwind
382 scheme) introduces non-negligible numerical diffusion for tracers. We thus use a
383 discretization of the divergence term of tracer flux (last term of left hand side of Eq.
384 (2)) chosen for optimal accuracy but minimal numerical diffusion. More specifically,
385 we use the 5^{th} order Weighted Essentially Non-Oscillatory (WENO) scheme [*Liu et al.*,
386 1994] to discretize that term to minimize numerical diffusion and achieve stable
387 computations.

388 Aggradation/degradation causes volumetric exchange of tracers between the active
389 layer and the substrate in this model framework, so we need to store a fraction of the
390 tracers on the substrate. For this, we use a simple multi-layer approach proposed by
391 *Ashida et al.* [1990], which was proposed for computing size-sorting of graded

392 sediment. This model is similar to the stratigraphy-storing models of *Viparelli et al.*
393 [2010], *Stecca et al.* [2014] and *Stecca et al.* [2016]. The model discretizes the
394 substrate as a number of layers with constant thickness, and calculates the exchange of
395 tracers between the active layer and only the top layer of the substrate, which is called
396 the transition layer. The treatment of the substrate in model of *Ashida et al.* [1990] is
397 more similar to the model of *Viparelli et al.* [2010] than either that of *Stecca et al.*
398 [2014], which generalizes the exchange of sediment between the active layer and other
399 substrate layers, or the model proposed by *Pelosi et al.* [2014], which does not use any
400 active layer assumption.

401

402 **3. RESULTS**

403 We perform 1D and 2D calculations of tracer advection-dispersion, using the flux-
404 and entrainment-based models described above, under equivalent conditions. Since the
405 1D model cannot capture free bars, comparison of the 1D and 2D results demonstrates
406 how the presence of single-row free bars affects the characteristics of tracer
407 advection-dispersion.

408 We use a straight channel that is 62.5 m wide and 20 km long for the computations.
409 The hydraulic conditions are determined in accordance with a linear stability analysis
410 of free bars so that the initial state is indeed subject to single-row alternate bar
411 instability. We performed this linear stability analysis using the relations presented
412 above, with the methodology of *Colombini et al.* [1987]. We accordingly selected
413 constant flow discharge of 305.7 m^3/s, an initial bed slope (S) of 0.00461, and a grain

414 size of 44.25 mm. These correspond to an initial Froude number (F_r) of 0.85, an initial
415 Shields number (θ) of 0.095, and an initial width-to-depth ratio (β) of 41.7, all
416 computed for the initial flat-bed case (i.e., in the absence of free bars). At the dynamic
417 equilibrium attained in the presence of free bars, the values of S, Fr, θ and β based on
418 cross-sectionally averaged parameters did not deviate strongly from these initial values,
419 although in some local shallow zones Fr deviated significantly from the initial value.
420 The grid sizes in the streamwise and transverse direction are 5 and 2.5 m, respectively.
421 The active layer thickness is twice the grain size. The mean step length used for the
422 entrainment-based model is set to be 100 times the grain size [*Einstein*, 1950]. With
423 these conditions, we first run the models to obtain well-developed single-row alternate
424 bars in the computational domain. These bars appear clearly only after a relaxation
425 distance from the inlet. A rectangular patch of tracers is then placed in the active layer
426 at the upstream end of the simulated free bar train. The discretized step size used to
427 calculate the deposition rate for the entrainment-based model is set to be half of the
428 minimum grid size, which is 1.25 m in this case. We found through trial runs that this
429 step size needs to be smaller than at least either half of the minimum grid size or one
430 tenth of the mean step length.

431 Figures 1 and 2 show the temporal changes of alternate bar morphology and the
432 spatial distribution of vertically integrated tracer amounts simulated by the 2D
433 entrainment- and flux-based models, respectively. These figures demonstrate that
434 simulated alternate bar morphology and its development between the two models are
435 consistent. Tracer transport characteristics, on the other hand, are somewhat different,
436 particularly in the early stage of the computations. The tracer transport in these

437 simulations can be categorized into three stages: 1) absence of the bars (a-2, b-2 of
438 Figures 1 and 2), 2) when the tracer plume just encounters the bars (c-2 of the same
439 two figures), and 3) in the presence of bars (d-2, e-2 of the same two figures). In the
440 first stage, the tracer plume advects downstream. This advecting tracer plume is seen
441 to disperse in the streamwise direction in the entrainment-based model, but is seen to
442 translate without dispersion in the flux-based model, as demonstrated in the model
443 explanation above. By comparing (a-2) and (b-2) of Figure 2 with the corresponding
444 panels of Figure 1, it can be clearly seen that at dynamic equilibrium in the absence of
445 bars (i.e. equivalent to 1D conditions) we need a stochastic bedload transport model to
446 reproduce the tracer dispersion; the entrainment-based model is an appropriate
447 approach to model this dispersion.

448 Since there is only a minor transverse component of bedload in the first stage, the
449 tracer plume simply advects downstream, and the shape of the tracer plume does not
450 change, except for the streamwise dispersion of the entrainment-based model. The
451 migrating alternate bars, however, significantly deform the shape of the tracer plume.
452 The alternate bars generate a meandering flow and associated complex bedload
453 transport and bed elevation variation in the streamwise and transverse directions; as
454 such, the tracer plume is horizontally stretched. In addition, because of the dynamic
455 bed evolution processes (i.e., migrating bars), the tracers in the active layer deposit
456 within the substrate (i.e., within the bars) and spend a longer waiting time before
457 re-entrainment than the tracers in the active layer. The tracer transport in the second
458 stage corresponds to a transition phase from the first to the third stage. The tracer
459 distribution in the second stage is thus discontinuous in space. After this transition

process, the migrating alternate bars mix the tracers well. Thus at the third stage, tracers buried in the bars are re-entrained because of their migration, and then transported again on the bed surface. Consequently, the tracer distribution becomes spatially smooth, tending to converge to a distribution that is symmetrical in the streamwise direction.

We define the vertical integral of tracer fraction F as:

$$F\left(x,y\right)=\int_{-\infty}^{\eta} f\left(x,y,z\right)dz, \tag{14}$$

where f is the local fraction of tracers within the layer corresponding to elevation z, and the corresponding width-averaged value $\overline{F}\left(x\right)$ as:

$$\overline{F}\left(x\right)=\frac{1}{B}\int_{-B/2}^{B/2}\int_{-\infty}^{\eta} f\left(x,y,z\right)dzdy, \tag{15}$$

where B is the channel width.

Figure 3 shows the temporal change of vertically-integrated, width-averaged tracer amount $\overline{F}$ in the longitudinal direction at this stage (i.e., stage 3, when the alternate bars are significantly affecting the tracers). The figure demonstrates that the fluctuations associated with bars drives a spatial distribution of tracers that asymptotically approaches a bell-shaped distribution at time passes. This implies that the long-term influence of the bars leads to an asymptotic pattern of dispersion of the tracers. Interestingly, the asymptotic behavior obtained from the flux-based and entrainment-based models are very similar, indicating the dominant role of alternate

479 bars in driving dispersion.

480 To discuss the results in detail, we quantify the tracer transport characteristics using
481 the tracer plume advection velocity, c and the standard deviation of the plume of
482 tracers in the longitudinal direction, σ. These are obtained from the 2D calculation
483 results as follows:

484
$$c = \frac{d\overline{x}}{dt}, \qquad \overline{x} = \frac{\int_0^{\infty}\int_{-B/2}^{B/2} xF(x,y)\,dydx}{\int_0^{\infty}\int_{-B/2}^{B/2} F(x,y)\,dydx}, \tag{16}$$

485
$$\sigma^2 = \frac{\int_0^{\infty}\int_{-B/2}^{B/2} (x-\overline{x})^2 F(x,y)dydx}{\int_0^{\infty}\int_{-B/2}^{B/2} F(x,y)dydx}, \tag{17}$$

486 where $\overline{x}$ is the centroid of tracers in the longitudinal direction. The temporal change
487 of the standard deviation of tracers can be used to characterize streamwise dispersion.
488 A pattern of normal dispersion (normal diffusion) leads to the power relationship, $\sigma \sim$
489 t^{γ}, with $\gamma = 0.5$. Here, γ is a scaling exponent characterizing the pattern of dispersion.
490 As noted above, deviation of the scaling exponent from 0.5 indicates anomalous
491 dispersion, specifically, superdiffusive dispersion for $\gamma > 0.5$, and subdiffusive
492 dispersion for $\gamma < 0.5$; superdiffusive (subdiffusive) dispersion results in faster
493 (slower) dispersion of tracers than normal dispersion [*e.g. Schumer et al., 2009*].

494 Figure 4a shows the temporal change of the advection velocity of the tracer plume
495 in all of four cases (i.e., 1D and 2D, flux- and entrainment-models). This figure

496 demonstrates that 1) in the absence of bars, the advection velocity is constant and
497 same for all cases, and 2) alternate bars slow the tracer plume down significantly. This
498 velocity slowdown is attributed to the intermittent burial of tracers within the bars (i.e.,
499 increasing waiting time).

500 We explain this by first considering the case of 1D dunes. If every bedload particle
501 is captured on the lee side of a dune, without throughput transport, then the bedload
502 transport rate can be calculated directly from the product of the mean dune height and
503 migration rate [*Simons et al.,* 1965]. This means that every particle is buried after
504 traveling the length of one dune. Here we find that alternate bars play a similar role to
505 dunes. That is, most of the bedload is bound up in bar migration rather than throughput,
506 thus implying repeated burial after transport on the order of one bar wavelength. This
507 makes the plume advection velocity extremely slow, since most of tracer transport is
508 bound up in bar migration. When stage 3 is reached, the deposition rate of tracers
509 within the bars coincides with their re-entrainment rate as bars pass through, exposing
510 zones of low elevation. After a sufficiently long time, the mean advection velocity
511 approaches a constant value which is considerably slower than the early (stage 1)
512 velocity, as well as the velocity simulated by the 1D models.

513 The presence of the bars plays a key role in the dispersion of tracers as well. Figure
514 4b shows that 1) in the absence of bars, the 1D and 2D models yield identical patterns
515 of dispersion features, i.e., no dispersion for the flux-based model and normal
516 dispersion for the entrainment-based model; 2) the onset of the influence of bars
517 greatly disperses the trace plume, causing a deviation from the 1D calculation; and

most importantly 3) the asymptotic pattern of dispersion after a sufficiently long time is somewhat superdiffusive dispersion, regardless of whether a flux-based or entrainment-based model is used.

At stage 1, e.g. hours 1 – 3 in Figure 4b, bars are absent, and the asymptotic pattern of dispersion obtained from the numerical model is consistent with the analytical forms of Eqs. (4) and (12); advection without dispersion in the flux-based model, and advection with normal dispersion in the entrainment-based model. During stage 2, when the tracer plume encounters bars, the dispersion becomes strongly superdiffusive (e.g. hours 7 – 20 in Figure 4b), followed by a short period of slightly subdiffusive behavior (e.g. hours 20 – 40 in Figure 4b). The strongly superdiffusive behavior is caused by horizontal stretching of the tracer plume and deposition of tracers within the bars, and the subsequent short period of slightly subdiffusive behavior may be attributed to the fact that most of the tracers stay within a bar until new bars migrate from upstream and re-entrain them. After that, repeated of transport, deposition, and re-entrainment events during stage 3 lead asymptotically to mildly superdiffusive behavior (e.g. after 100 hours in Figure 4b). Importantly, the flux-based model shows the same asymptotic behavior as the entrainment-based model. This indicates that the migrating alternate bars themselves drive dispersion much more effectively than particle-scale stochastic motion of the bedload.

This implication motivates us to perform numerical experiments for a sensitivity analysis of tracer advection-dispersion associated with single-row free bars. For this analysis, we use the flux-based model only, as the entrainment-based model shows

similar behavior at large times (Figure 4). Hereafter, we define the 2D flux-based run above as Case 1; Table 1 summarizes the set of parameters and cases for the analysis. We choose cases corresponding to three dimensionless parameters, i.e., the Froude number, Shields number, and width-to-depth ratio. The other parameters, conditions, and grid sizes used for all the cases are identical to those of Case 1. To make the morphodynamic features in all cases consistent, the combination of parameters has been specifically chosen to yield migrating alternate bars. Figure 5 shows the combination of parameters for all cases of bar regime criteria delineated based on the linear stability analysis of *Kuroki and Kishi* [1984], confirming our result that all the runs of Table 1 do indeed fall within the single-row alternate bar regime.

Figure 6 shows the tracer plume advection-dispersion characteristics for all cases. Their general characteristics are quite consistent. The migrating bars cause the slowdown of advection velocity and disperse the tracers. With passage of sufficient time, the tracer transport approaches an asymptotic form corresponding to constant advection velocity and the power dependence $\sigma \sim t^{\gamma}$ characterizing dispersion. Table 2 summarizes the results of asymptotic advection velocity and the scaling exponent, γ. With respect to tracer dispersion, the results suggest that 1) the scaling exponent is slightly different in each case, but nevertheless 2) the asymptotic dispersive behavior is either normal or weakly superdiffusive, but not subdiffusive. A high Froude number Fr and width/depth ratio β, and a low Shields number θ tend to increase the scaling exponent, and thus superdiffusive behavior.

The concepts embodied in the random walk model allow interpretation of the

562 physical mechanisms governing this large-scale dispersion and the origin of
563 superdiffusive behavior. In the framework of random walk model, random motion of
564 the walkers asymptotically leads to normal diffusion in accordance with Central Limit
565 Theorem (CLT) [e.g., *Schumer et al.*, 2009]. Anomalous diffusion is associated with
566 conditions that break the CLT. In linear and nonlinear stability theory, single-row and
567 multiple-row alternate bars are idealized as phenomena that show purely deterministic
568 spatiotemporal variation [*e.g. Colombini et al.,* 1987]. Such bars have no random
569 element, and cannot be expected to cause asymptotic tracer dispersion that is either
570 normal or anomalous. Indeed free bars and associated tracer transport are not purely
571 random and stochastic processes; migrating bars tend to be relatively well-ordered,
572 and the bars constrain the length scale of tracer motion [*Pyrce and Ashmore*, 2003,
573 2005]. Nevertheless, the properties of free bars (i.e., wavelength, waveheight, celerity,
574 and transverse mode) generally show some stochastic variation in space and time.
575 Even under the simple conditions adopted herein (i.e., steady water discharge and
576 bedload supply, uniform grain size, and straight channel with constant slope), our
577 model reproduces this stochasticity. The irregularity of individual bars gives some
578 randomness to the system, resulting in tracer dispersion. This randomness inherent to
579 the model can be expected to cause normal diffusion, as would be the case with a
580 random walk model, as long as the CLT is satisfied. We investigate whether or not this
581 is the case below. While doing this, it is worthwhile to investigate the probability
582 density functions (PDFs) of tracer of travel distance and waiting time, because
583 whether or not the tails of these distributions are heavy or thin can influence whether
584 or not dispersion is normal or anomalous. With this in mind, we interpret the

585 simulation results in the context of probability.

586 The model we use for the simulations is Eulerian-based, so we cannot calculate the
587 precise probability distributions of the travel distance and waiting time. In principle,
588 we would need to track all individual particles to do so [*Lajeunesse et al.*, 2010;
589 *Roseberry et al.*, 2012; *Campagnol et al.*, 2015]. We describe alternatives to such a
590 Lagrangian description below.

591 *Voepel et al.* [2013] estimated a PDF of particle waiting time from an experimental
592 time series data of bed surface elevation. They assumed that when the local bed
593 surface rises at a given elevation, a tracer particle must have deposited onto the bed at
594 that elevation, and when the bed surface falls at a given elevation, a bed particle there
595 must have been entrained. The duration between these events characterizes particle
596 waiting time. By discretizing the bed elevation between the maximum and minimum
597 elevation recorded within a sampling period, they calculated the conditional
598 probability of waiting time for a bed particle at each discretized elevation. This
599 probability is in turn weighted based on the probability $p_e(z)$ of the bed surface
600 elevation being at each discretized elevation z when calculating an unconditional
601 waiting time for a bed particle. We apply this method to time series data of bed
602 elevation generated by the numerical model at each grid point along a cross section
603 where bars are well developed. In principle, the relevant PDF's should be based on
604 averaging over the entire reach along which alternate bars are developed. If, however,
605 the statistical characteristics of the alternate bars (e.g. average bar height, wavelength
606 and migration speed) are invariant along the reach in question, it suffices to obtain the

607 PDF's characterizing waiting time based on data corresponding to grid points along a
608 single cross-section.

609 We denote the probability density that the bed is at elevation z at transverse position
610 y on the cross-section as $p_e(z,y)$, and the corresponding conditional probability that
611 waiting time T exceeds τ at elevation z and transverse position y as $P(T>\tau| z, y)$. Figure
612 7 shows two examples of time series of bed elevation variation produced by the model
613 for Case 1. The left-hand side of panel a) corresponds to the time series for left bank of
614 a cross section, and the left-hand side of panel b) corresponds to channel center. The
615 corresponding time series of waiting times are denoted by the lengths of the gray lines
616 connecting times when the bed moves upward across a given elevation z to when the
617 bed subsequently next moves downward across this same elevation. Illustrated on the
618 right-hand side for each panel in the figure is the corresponding PDF p_e for elevation.
619 Note that since our simulation is 2D horizontal, the probability of bed surface
620 elevation becomes a function of both the transverse (y) and vertical (z) coordinates.
621 The unconditional exceedance probability distribution of waiting time can be
622 calculated as follows:

623 $$P(T>\tau)=\int\int P(T>\tau \mid z,y)\, p_e(z,y)\,dzdy \tag{18}$$

624 where τ is the waiting time, $p_e(z,y)$ is the probability density that of the bed surface is
625 at (z, y), and $P(T>\tau)$ is the exceedance probability of waiting time.

626 We can now obtain an estimate of the probability distribution of travel distance in
627 one transport "event". In order to do this, we repeat the calculation of Cases 1 – 7

above, but with the following constraint; once a tracer particle is deposited in the substrate (i.e. buried within the bars), it is not allowed to be re-entrained (i.e., by setting f_I in Eq. (2) equal to zero whenever the bed degrades due to bar passage). We then define the duration of the "event" as the time required for a specified large fraction (e.g. 0.999) such that nearly all of the initially deployed particles are buried in the substrate. The spatial variation of distance to burial at the end of this "event" then serves as a surrogate for the PDF of travel distance. That is, the simulated tracer distribution at the end of the "event" normalized by the total amount of tracers serves as the probability density function of the travel distance within that "event". This, of course does not represent the true travel distance in the system, because re-entrainment is not allowed. The cumulative travel distance distribution, however, can be approximated as the sum of many such single transport "events" [*Hassan et al.*, 2013]. Since the flux-based model does not calculate the trajectory of tracers, we cannot measure the exact travel distance along any bedload streamline (i.e. path everywhere parallel to the bedload vector). With this in mind, we define travel distance in terms of downstream distance as measured along the x coordinate rather than path length.

Figure 8 shows the estimated exceedance probability of travel distance, l, and waiting time, τ, from the calculation results for all seven runs. The slope of this log-log plot, α, indicates the characteristics of the tails associated with long travel distance or waiting time; a slope with $\alpha < 2$ implies a heavy-tailed distribution; whereas a slope with $\alpha > 2$ implies a thin-tailed distribution. The threshold slope between thin- and heavy-tailed feature (e.g., $P(L>l) \sim l^{-2}$) is also shown on the figure.

650 The figures exhibits thin-tailed behavior for travel distance distribution in all cases,
651 implying that the PDF of travel distance feature is unlikely to be the origin of
652 anomalous dispersion. On the other hand, the exceedance probability distribution of
653 waiting time shows more complex behavior than that of the travel distance. The tails
654 for Cases 2, 3 and 5 appear to be thin in Figure 8. In Case 1 there are likely two slope
655 breaks in the tail, similar to a truncated Pareto distribution (combination of
656 exponential and power functions) [*Aban et al.*, 2006], and the tails for Cases 4, 6, and
657 7 appear to be heavy. This heavy-tailed waiting time may be the origin of the
658 anomalous dispersion seen in Cases 1, 4, 6 and 7.

659 *Schumer et al.* [2009] show that in cases when the travel distance distribution is
660 thin-tailed, a heavy-tailed waiting time PDF causes subdiffusive dispersion in the
661 context of a Continuous Time Random Walk (CTRW) model. *Weeks et al.* [1996], on
662 the other hand, suggest that a heavy-tailed waiting time PDF could result in either
663 super- or sub-diffusive dispersion depending on the heaviness of the tail (i.e., α). Both
664 suggest that the tail of waiting time required to generate subdiffusive dispersion needs
665 to be extremely heavy (e.g., $\alpha < 0.5$ [*Weeks et al.*, 1996]), which is unlikely in the
666 present simulations. Our results suggest that a moderately heavy-tailed waiting time
667 (i.e. α slightly less than 2), may be the cause of superdiffusive dispersion, in line with
668 *Weeks et al.* [1996]. This is consistent with the superdiffusive exponent γ in the
669 relation $\sigma \sim t^{\gamma}$ found for several of the results, e.g. 0.68 for Case 1 and 0.63 for Case 4.

670 A physically based description of the behavior generating such PDF tail may be as
671 follows. The free bar morphology and its migration strongly restrict the travel distance

672 of tracers due to the frequent passage of troughs [*Pyrce and Ashmore*, 2003, 2005], so
673 travel distance is strongly bounded by the frequency of encounter with a trough.
674 Although the randomness of free bars gives a certain stochasticity to tracer motion,
675 well-regulated migrating bars act to inhibit the preferential tracer motion necessary to
676 generate a heavy-tailed pattern of tracer dispersal. On the other hand, the randomness
677 of free bars, especially in terms of bar height, plays an important role in the tail of the
678 PDF of waiting time. The randomness of free bar properties introduces a large
679 stochastic variability in bed surface elevation. The PDF of trough elevation in
680 particular plays an important role in this regard [*Blom et al.*, 2003; *van der Mark et al.*,
681 2008]. Deeply-buried particles are only infrequently re-entrained into the active layer,
682 so generating a very long waiting time. Randomness sufficient to generate a
683 heavy-tailed waiting time in the simulation may be, for example a result of nonlinear
684 interaction among different bar modes [*Pornprommin et al.*, 2004; *Watanabe*, 2007].
685 Interestingly, the scaling exponent γ in the dispersion relation tends to be high (i.e.,
686 more superdiffusive) when the flow conditions approach the threshold between
687 alternate bars and multiple bars (Fig. 5), corresponding to a sufficiently wide channel.

688

689 **4. DISCUSSION**

690 The computational conditions of this study are somewhat extreme in terms of the
691 morphological changes of the bed surface, in so far as the alternate bars continue
692 migrating downstream in a relatively regular way. This notwithstanding, the model
693 does capture a stochastic element to bed deformation by alternate bars, particularly in

694 terms of minimum trough elevation. The results reported here are consistent with
695 several important findings based on field observations of long-term tracer
696 advection-dispersion. *Hassan et al.* [2013] suggest that bed morphology is more
697 important for controlling tracer motion than hydraulic regime. They summarize a
698 number of field datasets, showing that the travel distance distribution could be
699 heavy-tailed in a single flood event, but is unlikely to be heavy-tailed after multiple
700 flood events. As we have shown, this is because the bed elevation variation (in this
701 case associated with alternate bars) eventually results in capture of the tracers within
702 the bed, so constraining the length scale of travel distance.

703 The superdiffusive behavior seen in several of the runs reported here, and the
704 associated heavy-tailed waiting time qualitatively agrees with several field
705 observations [e.g., *Phillips et al.*, 2013; *Olinde and Johnson*, 2015]. It should be kept
706 in mind, however, that only the morphodynamics of a single morphological unit, i.e.,
707 that of alternate bars, is considered here. In reality, however, morphological units
708 coevolve in a system and control the overall morphodynamic features. For instance,
709 bedforms (ripples, dunes, and antidunes) [*Blom and Parker*, 2004], multiple-row bars
710 [*Fujita*, 1985; *Shuurman et al.*, 2013], braiding [*Kasprak et al.*, 2015], and meandering
711 [*Asahi et al.*, 2013] are dynamic components that add complexity the problem of tracer
712 dispersal. Corresponding static components include curvature-induced forced bars
713 [*Blondeaux and Seminara*, 1985], mid-channel bars driven by channel width variation
714 [*Zolezzi et al.*, 2012], and floodplains occasionally accessed by the flow [*Lauer and*
715 *Parker*, 2008]. Interactions among components of dynamic bed evolution at different
716 spatial and temporal scales can result in a complex pattern of bed surface elevation

variability, and static components can serve to store large amounts of sediment. These factors all complicate the issue of waiting time distribution. A thorough understanding of how the interaction of multiscale bed morphologies and their dynamics affect tracer advection-dispersion would be key to explaining crucial phenomena we have not touched upon in this paper, including subdiffusive dispersion [*Nikora et al.*, 2002; *Schumer et al.*, 2009; *Zhang et al*., 2012] and advective slowdown [*Ferguson et al.*, 2002; *Haschenburger*, 2013; *Pelosi et al.*, 2016].

As we have shown in our simulations, the waiting time distribution associated with the randomness of free bars is not simply thin-tailed, but neither is it extremely heavy-tailed. This is because the randomness of the simulated alternate bars is not extreme, so that the migrating bars eventually transport all the tracers we deploy. Such conditions are insufficient to achieve a strongly heavy-tailed waiting time distribution leading to subdiffusive dispersion, as suggested by *Weeks et al.* [1996] and *Schumer et al.* [2009]. Extra randomness associated with morphodynamics at different scales may affect the heaviness of the waiting time, possibly pushing the pattern of dispersion from superdiffusive to subdiffusive. Additionally, the migration speed of free bars in nature tends to be relatively slow, even in straight channels, and free bars may in some cases stop migrating [*Crosato et al.*, 2011; *Eekhout et al.*, 2013; *Rodrigues et al.*, 2015]. The retention of tracers in a quasi-static bed morphology would constrain tracer motion, eventually resulting in subdiffusion and advective slowdown as all tracer particles eventually become trapped and stop moving.

Some tracer particles in transport are trapped in the downstream faces of alternate

739 bars, and thus buried, whereas other particles find trajectories that allow them to
740 bypass one or more bars without being trapped. The dispersal pattern of bedload
741 particle tracers under the influence of migrating alternate bars is likely sensitive to the
742 degree of bar trapping versus bypassing. More specifically, the relative importance of
743 these two patterns of behavior likely affect both travel distance and waiting time. For
744 instance, stronger trapping should reduce travel distance and cause longer waiting
745 times, possibly resulting in more subdiffusive behavior. In morphodynamic models
746 such as the present one, this behavior is determined by the aggregate of multiple
747 physical submodels (e.g, gravitational effects acting on bedload transport and three
748 dimensional flow structures such as topographically-induced secondary flow at the
749 downstream side of bars), and is also affected by the numerical scheme itself. Such
750 factors contribute to alternate bar characteristics such as wavelength, wave height and
751 migration speed [e.g., *Nelson*, 1990; *Schuurman et al.*, 2013; *Iwasaki et al.*, 2016].
752 However, it is in general not possible to accurately simulate numerically the full range
753 of behavior observed in experiments or field rivers in the framework of a 2D
754 morphodynamic model [e.g., *Shimizu and Itakura*, 1989; *Defina*, 2003]. Further model
755 validation in terms of a comparison with experimental or field measurements of
756 spatiotemporal changes in alternate bar characteristics, as well as the pattern of tracer
757 particle dispersal among them, are desirable.

758 A critical model constraint of the present analysis is the assumption that the
759 sediment consists of material of uniform grain size. In the case of graded sediment,
760 variability of particle mobility according to size class further complicates tracer
761 transport and dispersion [*Ganti et al.*, 2010; *Hashenburger*, 2013]. In addition to the

762 effects of varying mobility, sediment size gradation also plays a role in shaping
763 bedform characteristics [*Lanzoni and Tubino*, 1999; *Lanzoni*, 2000; *Blom et al.*, 2003]
764 by generating stronger randomness of bedforms than those generated under the
765 constraint of uniform sediment [*Takebayashi and Egashira*, 2008]. All these factors
766 will impact tracer advection-dispersion. The present model thus invites extension to
767 the case of sediment size mixtures [*Blom and Parker*, 2004; *Blom et al.*, 2006; *Blom et*
768 *al.*, 2008; *Viparelli et al.*, 2010; *Stecca et al.*, 2016].

769 Lastly, another model limitation is our use of a discretized layer model (i.e., an
770 active layer and several substrate layers) to calculate tracer transport and to store the
771 stratigraphic record of tracer deposition. *Parker et al.* [2000] showed that the active
772 layer model approximates the probability density function for entrainment as a
773 step-like function, i.e., constant probability within the active layer and no possibility
774 for entrainment in the substrate. Moreover, discretized layer models inject numerical
775 dispersion into any numerical calculation. This creates difficulties in treating
776 deposition and re-entrainment accurately. A more general treatment in terms of a
777 formulation of the Exner equation of sediment continuity that is intrinsically
778 continuous in the vertical, with no active layer, would be of value in future numerical
779 models [*Parker et al.*, 2000; *Blom and Parker*, 2004; *Blom et al.*, 2008; *Stecca et al.*,
780 2016; *Pelosi et al.*, 2016].

781

782 **5. CONCLUSIONS**

783 In this paper we present numerical simulations of large-scale tracer particle

784 advection-dispersion in alluvial rivers. We specifically focus on conditions for which
785 bedload is the dominant mode of sediment transport, and for which the river is subject
786 to the formation of free, migrating alternate bars. We apply two formulations of the
787 Exner equation of sediment conservation; a standard flux form, in which bed elevation
788 change is related to the divergence of the vector of sediment transport rate, and a
789 stochastic entrainment form, in which bed elevation change is related to the net
790 entrainment rate of particles into bedload. In modeling tracer advection-dispersion, we
791 use a single grain size, as well as an active layer formulation in which active layer
792 thickness scales with grain size. We specifically consider conditions so that no bed
793 aggradation or degradation occurs when averaged over the bars.

794 We find that the presence of bars has a dramatic effect on streamwise
795 advection-dispersion of tracer particles. When the flux form of Exner equation is used
796 for the case of a flat bed (no bars), tracer particles advect without dispersing. When the
797 entrainment formulation is applied to the same condition, the particles also disperse, in
798 response to the stochasticity associated with the PDF of particle step length. The effect
799 of bars is to substantially increase the streamwise dispersion rate. The statistics of the
800 pattern of advection-dispersion seen in the presence of bars are to a large degree
801 independent of whether the flux or entrainment forms of Exner equation are used,
802 indicating that dispersion is dominated by the bars themselves.

803 The simulated asymptotic pattern of streamwise tracer advection-dispersion under
804 the influence of free bars is either normal or weakly superdiffusive. The numerical
805 model self-generates stochasticity in bar properties, including wavelength, wave

806 height, and celerity. This in turn imparts a randomness to tracer behavior, resulting in
807 large-scale dispersion. More specifically, the randomness of the alternate bar
808 dimensions renders local bed surface elevation a stochastic quantity. In some cases, the
809 probability distribution of trough elevation is such that it results in a heavy-tailed
810 waiting time distribution; a deeply-buried particle must wait an anomalously long time
811 before it is re-entrained. Migrating bars strongly constrain the length-scale of tracer
812 transport, likely causing a thin-tailed distribution of travel distance. The combination
813 of thin-tailed travel distance and heavy-tailed waiting time may be the cause of the
814 simulated superdiffusive dispersion when it occurs.

815 The morphological evolution of bed surface we consider in the simulation is that of
816 alternate bars only, in the absence of bed aggradation or degradation when averaged
817 over the bars. However, the coexistence of several static and dynamic morphological
818 elements might make the waiting time distribution more complex, perhaps causing
819 other dispersion behavior (e.g., subdiffusive dispersion) and perhaps affecting
820 advection (e.g., advective slowdown), which are not illustrated in this paper. The
821 effects of different bed morphologies (e.g., multiple-row bars, braiding and 3D dunes)
822 and channel planform (e.g., meandering, systematic width variation, and interacting
823 channel and floodplain) on tracer advection-dispersion invite further investigation. In
824 addition, model extensions including e.g. sediment size mixtures, and also describing
825 the bed in terms of a continuous vertical structure rather than the active layer
826 formulation so as to better simulate vertical mixing of tracers in the bed [*e.g. Pelosi et*
827 *al.*, 2014, 2016], are future challenges in the pursuit of a comprehensive understanding
828 of bedload tracer advection-dispersion in nature. This study contributes to a better

829 understanding of tracer advection-dispersion in the global regime [*Nikora et al.*, 2002].

830

831 **APPENDIX**

832 A. Flux- and entrainment-based model: Free bar simulation

833 In this appendix we show how the flux- and the entrainment-based morphodynamic
834 models work for free bar simulations. The model framework using the flux-based
835 model to reproduce free bar inception and development has been well documented in
836 the literature [e.g., *Callendar*, 1969; *Parker*, 1976; *Fredsøe*, 1978; *Kuroki and Kishi*,
837 1984; *Colombini et al.*, 1987; *Shimizu and Itakura*, 1989; *Nelson*, 1990; *Schielen et al.*,
838 1993; *Defina*, 2003; *Federici and Seminara*, 2003; *Pornprommin and Izumi*, 2011;
839 *Crosato et al.*, 2012]. A horizontal 2D morphodynamic model, which consists of a
840 shallow water flow model and a flux-based Exner equation with the appropriate bed
841 slope effect on bedload transport (especially in the transverse direction) is sufficient
842 for reproducing the linear and nonlinear free bar dynamics. As far as we know,
843 however, there has been no attempt to use entrainment-based models for free bar
844 simulations in rivers. A model framework and sensitivity analysis of the results of
845 these morphodynamic models is thus of use.

846 One-dimensional flux- and entrainment-based models of morphodynamics are
847 essentially identical under dynamic equilibrium conditions [*Nakagawa and Tsujimoto*,
848 1980]. Both types of formulations have been coupled with hydrodynamic models to
849 simulate 1D bed evolution (e.g., bedform dynamics and bed aggradation/degradation)

850 [e.g., *Giri and Shimizu*, 2006; *Yamaguchi et al.*, 2009; *Pelosi and Parker*, 2014]. We
851 address the 2D case in this appendix.

852 A key issue for solving the 2D entrainment-based model is the determination of how
853 to compute the deposition rate. The deposition rate at (x, y) is the total amount of
854 bedload that is transported from upstream of (x, y) and deposited onto the bed at (x, y);
855 thus, this term must be calculated based on the trajectory of motion of the bedload
856 particles themselves [*Nagata et al*., 2000]. The flow velocity near the bed surface, as
857 well as the local bed slope, consideration of the effect of which is necessary to achieve
858 a finite wavelength [*Engelund and Skovgaard*, 1973; *Fredsøe*, 1978; *Kuroki and Kishi*,
859 1984], determine the motion of bedload particles on the bed surface. Transverse
860 bedload transport formulas [*Ikeda*, 1982; *Hasegawa*, 1989; *Sekine and Parker*, 1992;
861 *Talmon et al.*, 1995] have been used to describe the direct gravitational effect of bed
862 slope on bedload transport in flux-based morphodynamic models. This suggests that
863 the use of such bedload formulas to compute the trajectory of bedload particles (and
864 thus their deposition rate) would be sufficient to reproduce free bar instability in an
865 entrainment-based model. We thus consider a bedload vector field defined as:

866 $$\frac{dx}{q_{bx}} = \frac{dy}{q_{by}} = \frac{ds}{q_{bs}}, \tag{A1}$$

867 where s is the local "bedload streamline" coordinate (i.e. coordinate along which the
868 differential arc length vector is everywhere parallel to the bedload vector), q_{bs} is the
869 bedload transport rate in the s direction, and q_{bx}, q_{by} are the bedload transport rates in
870 the x and y directions (Cartesian coordinate system) that are obtained in a manner

identical to the flux-based model. Integrating the deposition rate with respect to particle trajectory leads to the following 2D entrainment-based Exner equation:

$$\left(1-\lambda_p\right)\frac{\partial \eta}{\partial t} = -E\left(x,y\right) + \int_0^\infty E\left[x - x'\left(s\right), y - y'\left(s\right)\right] f_p\left(s\right) ds, \tag{A2}$$

where x' and y' are the particle locations along the trajectory of bedload motion. Taylor-expanding E in the integral for deposition rate and retaining only the 1st order term gives, it is found that:

$$\left(1-\lambda_p\right)\frac{\partial \eta}{\partial t} = -\frac{\partial E}{\partial x} L_x - \frac{\partial E}{\partial y} L_y, \tag{A3}$$

in which:

$$L_x = \int_0^\infty x'\left(s\right) f_p\left(s\right) ds, \qquad L_y = \int_0^\infty y'\left(s\right) f_p\left(s\right) ds. \tag{A4}$$

We linearize the problem by considering a locally constant angle of bedload transport direction with respect to the x-axis, θ_s, defined as:

$$\frac{dy}{dx} = \frac{q_{by}}{q_{bx}} = \tan\theta_s. \tag{A5}$$

This gives the following relationships:

$$L_x = L_s \cos\theta_s, \qquad L_y = L_s \sin\theta_s. \tag{A6}$$

This simplification reduces Eq. (A2) to:

886 $$\left(1-\lambda_p\right)\frac{\partial \eta}{\partial t}=-\frac{\partial}{\partial x}\left(EL_x\cos\theta_s\right)-\frac{\partial}{\partial y}\left(EL_x\sin\theta_s\right)=-\frac{\partial q_{bx}}{\partial x}-\frac{\partial q_{by}}{\partial y}. \quad \text{(A7)}$$

887 The derivation above suggests that in correspondence to the 1D case, under the
888 constraint of mobile-bed equilibrium the flux- and entrainment-based models are
889 essentially identical in the 2D case as well. This correspondence implies that in a
890 linear stability analysis, the entrainment formulation predicts the formation of alternate
891 bars similarly to the flux formulation.

892 We elaborate on more specific calculation procedures for the deposition rate as
893 follows. We assume that a bedload particle, which is entrained at the center of each
894 computational cell, represents the motion of all bedload particles that are entrained in
895 each cell, meaning that we calculate the trajectory of each cell [*Nabi et al.*, 2013b] as
896 follows:

897 $$\begin{aligned} x_p{}^n &= x_{entrained}+\sum_{i=1}^{n-1}\Delta s\left(\frac{q_{bx}}{q_{bs}}\right)_{x=x_p{}^i,y=y_p{}^i}, \\ y_p{}^n &= y_{entrained}+\sum_{i=1}^{n-1}\Delta s\left(\frac{q_{by}}{q_{bs}}\right)_{x=x_p{}^i,y=y_p{}^i}, \end{aligned} \quad \text{(A8)}$$

898 where $x_{entrained}$, $y_{entrained}$ is the location where the particle is entrained, Δs is the
899 discretized step size used to compute the trajectory, n is the index number of the
900 discretized steps, and x_p and y_p are the particle locations at the n^{th} discretized step. We
901 continue increasing the number of steps n until the cumulative PDF of step length f_p
902 reaches almost unity, meaning that the entrained bedload has all deposited onto the bed
903 along the computed trajectory so as to satisfy mass conservation of bedload tracer

904 particles. At each n^{th} step, the cell we track in principle overlaps with four
905 computational cells. We compute the deposition rate for these four cells based on the
906 percentage of overlapped area. Note that for this procedure, we calculate q_{bx} and q_{by} at
907 x_p^i and y_p^i based on the exact location of the particle we track. According to our trial
908 calculations, a simple interpolation of bedload fluxes computed at other locations (e.g.,
909 center of cell or boundary of cell) to x_p^i and y_p^i can cause development of very small
910 bars with high transverse mode. This may be because such an interpolation results in
911 use of a wide discrete points in computing the local bed slope, leading to inaccuracy in
912 a parameter that plays an important role in the inception of free bars [*Kuroki and Kishi*,
913 1984] as well as in the stabilization of the computation of bed evolution [*Mosselman*
914 *and Le*, 2016].

915 Lastly, we illustrate the sensitivity of free bar formation to the type of Exner
916 formulation (flux versus entrainment), and to variation in mean step length. The
917 calculations here are at experimental scale: channel width is 0.48 m, grain size is 1.3
918 mm, bed slope is 0.075, and water discharge is 3 *l*/s, corresponding to a Froude
919 number of 0.88, a Shields number of 0.06, and a width-to-depth ratio of 27.7. Mean
920 step length characterizes a lag effect on bedload transport; the longer the step length,
921 the more stable bed perturbations become [*Mosselman and Le*, 2016], suppressing the
922 conditions for the linear development of free bars [*Kuroki and Kishi*, 1984]. Figure A1
923 shows the sensitivity of the wavelength and wave height of free bars to the type of
924 morphodynamic model (flux versus entrainment) and variation in mean step length.
925 According to this sensitivity analysis, the lag effect on the initially selected bar
926 wavelength is fairly strong, whereas the effect on the equilibrium wavelength and

927 wave height is minor.

928

929 **Notations**

930 B : channel width [L]

931 c : tracer plume advection velocity [L/T]

932 D : volumetric deposition rate of sediment per unit area onto the bed [L/T]

933 E : volumetric entrainment rate of sediment into the bedload per unit bed area
934 into the bedload [L/T]

935 F : vertically-integrated tracer amount at (x,y) [L]

936 $\overline{F}(x)$: width-averaged value of vertical integral of tracer fraction [L]

937 F_r : initial Froude number [-]

938 f : the local fraction of tracers [-]

939 f_a : fraction of tracers in the active layer [-]

940 f_I : fraction of tracers exchanged at the interface between the active layer and
941 the substrate [-]

942 f_p : probability density function (PDF) of step length [1/L]

943 f_t : fraction of tracers in the substrate at the interface between the active layer
944 and the substrate [-]

945 l : travel distance [L]

946 L_a : active layer thickness [L]

947 L_s : mean step length [L]

948 n : index number of the discretized steps [-]

949 $P(L>l)$: exceedance probability of travel distance [-]

950 $P(T>\tau)$: exceedance probability of waiting time [-]

951 $p_e(z)$: probability of bed surface elevation being at each discretized elevation [1/L]

952 q_b : volume bedload transport rate per unit width [L^2/T]

953 q_{be} : equilibrium local bedload transport rate per unit width [L^2/T]

954 q_{bx} : volume bedload transport rate per unit width in x direction [L^2/T]

955 q_{by} : volume bedload transport rate per unit width in y direction [L^2/T]

956 q_{bs} : volume bedload transport rate per unit width in s direction [L^2/T]

957 S : initial bed slope [-]

958 s : streamwise coordinate [L]

959 t : time [T]

960 x : streamwise coordinate [L]

961 $\bar{x}$: centroid of tracers in terms of streamwise direction [L]

962 $x_{entrained}$: x where the particle is entrained [L]

963 x_p ,y_p : particle location at n^{th} discretized step [L]

964 y : transverse coordinate [L]

965 $y_{entrained}$: y where the particle is entrained [L]

966 z : vertical coordinate [L]

967 α : indicator of power relation of exceedance probability distribution [-]

968 β : initial width-to-depth ratio (aspect ratio) [-]

969 γ : scaling exponent characterizing the pattern of tracer dispersion in a relation,

970 $\sigma \sim t^{\gamma}$ [-]

971 Δs : discretized step size to compute the trajectory in entrainment-based model

972 [L]

973 η : bed surface elevation [L]

974 θ : initial Shields number [-]

975 θ_s : angle of streamline to x axis [rad]

976 λ_p : porosity of bed [-]

977 μ_1 : first moment of step length PDF [L]

978 μ_2 : second moment of step length PDF [L^2]

979 σ : standard deviation of the plume of tracers in longitudinal direction [L]

980 τ : waiting time [L]

981

982

983 **ACKNOWLEDGEMENTS**

984 T.I. was supported by a research project “Improving Morphodynamic Predictions in
985 Rivers” funded by the U.S. Geological Survey National Research Program. Y.S. was
986 supported by Grant-in-Aid for Scientific Research on Innovative Areas (Grant Number
987 24110006) of the Ministry of Education, Culture, Sports, Science, and Technology in
988 Japan. G.P. was in part supported by the US National Science Foundation (grant no.
989 EAR-1124482).

990

991 **REFERENCES**

992 Aban, I.B., M.M. Meerschaert, and A.K. Panorska (2006), Parameter estimation of the
993 truncated Pareto distribution, *J. Amer. Statist. Assoc.*, 101, doi: 10.1198/
994 016214505000000411.

995 Ancey, C. (2010), Stochastic modeling in sediment dynamics: Exner equation for
996 planar bed incipient bed load transport conditions, *J. Geophys. Res.*, 115, F00A11,
997 doi:10.1029/2009JF001260.

998 Asahi, K., Y. Shimizu, J. Nelson, and G. Parker (2013), Numerical simulation of river
999 meandering with self-evolving banks, *J. Geophys. Res.*, 118(4), 2208–2229,
1000 doi:10.1002/jgrf.20150.

1001 Ashida, K., and M. Michiue (1972), Hydraulic resistance and bed transport rate in
1002 alluvial stream, *Proc. of JSCE*, 201, 59–69. (in Japanese)

1003 Ashida, K., S. Egashira, B. Liu, and M. Umemoto (1990), Sorting and bed topography
1004 in meander channels, *Annuals, Disaster Prevention Research Institute*, Kyoto
1005 University, 33(B-2), 1-19 (in Japanese).

1006 Blom, A., J.S. Ribberink, and H.J. de Vriend (2003), Vertical sorting in bed forms:
1007 Flume experiments with a natural and a trimodal sediment mixture, *Water Resour.*
1008 *Res.*, 39(2), 1025, doi:10.1029/2001WR001088.

1009 Blom, A., and G. Parker (2004), Vertical sorting and the morphodynamics of bed
1010 form-dominated rivers: A modeling framework, *J. Geophys. Res.*, 109, F02007,
1011 doi:10.1029/2003JF000069.

1012 Blom, A., G. Parker, J. S. Ribberink, and H. J. de Vriend (2006), Vertical sorting and
1013 the morphodynamics of bed-form dominated rivers: An equilibrium sorting model,
1014 *J. Geophys. Res.*, 111, F01006, doi:10.1029/2004JF000175.

1015 Blom, A., J.S. Ribberink, and G. Parker (2008), Vertical sorting and the
1016 morphodynamics of bed form-dominated rivers: A sorting evolution model, *J.*
1017 *Geophys. Res.*, 113, F01019, doi:10.1029/2006JF000618.

1018 Bohorquez, P., and C. Ancey (2015), Stochastic-deterministic modeling of bed load
1019 transport in shallow water flow over erodible slope: Linear stability analysis and
1020 numerical simulation, *Adv. Water Resour.*, 83, 36-54, doi:
1021 10.1016/j.advwatres.2015.05.016.

1022 Bradley, D.N., G.E. Tucker, and D.A. Benson (2010), Fractional dispersion in a sand
1023 bed river, *J. Geophys. Res.*, 115, F00A09, doi:10.1029/2009JF001268.

1024 Callander, R.A. (1969), Instability and river channels, *J. Fluid Mech.*, 36, 465-480,
1025 doi:10.1017/S0022112069001765.

1026 Campagnol, J., A. Radice, F. Ballio, and V. Nikora (2015), Particle motion and
1027 diffusion at weak bed load: accounting for unsteadiness effects of entrainment and
1028 disentrainment, *J. Hydraul. Res.*, 53(5), 633-648, doi:
1029 10.1080/00221686.2015.1085920.

1030 Colombini, M., G. Seminara, and M. Tubino (1987), Finite amplitude alternate bars, *J.*
1031 *Fluid Mech.*, 181, 213-232, doi:10.1017/S0022112087002064.

1032 Crosato, A., E. Mosselman, F.B. Desta, and W.S.J. Uijttewaal (2011), Experimental
1033 and numerical evidence for intrinsic nonmigrating bars in alluvial channels, *Water*
1034 *Resour. Res.*, 47, W03511, doi:10.1029/2010WR009714.

1035 Defina, A. (2003), Numerical experiments on bar growth, *Water Resour. Res.*, 39(4),
1036 1092, doi:10.1029/2002WR001455.

1037 Duro, G., A. Crosato, and P. Tassi (2016), Numerical study on river bar response to
1038 spatial variations of channel width, *Adv. Water Resour.*,
1039 doi:10.1016/j.advwatres.2015.10.003.

1040 Eekhout, J.P.C., A.J.F. Hoitink, and E. Mosselman (2013), Field experiment on
1041 alternate bar development in a straight sand-bed stream, *Water Resour. Res.*, 49,
1042 8357-8369, doi:10.1002/2013WR014259.

1043 Einstein, H. 1937. Bedload transport as a probability problem, Ph.D thesis, Colorado
1044 State University, Fort Collins, Colorado.

1045 Einstein, H. (1950), The bed-load function for sediment transportation in open channel
1046 flows, *Technical Bulletin 1026*, *US Dept. of the Army*, *Soil Conservation Service*,
1047 *Washington*, *DC*.

1048 Engelund, F. and O. Skovgaard (1973), On the origin of meandering and braiding in
1049 alluvial streams, *J. Fluid Mech.*, 57(2), 289-302, doi:
1050 10.1017/S0022112073001163.

1051 Exner, F. M. (1925), U ber die wechselwirkung zwischen wasser undgeschiebe in
1052 flussen, Akad.Wiss.Wien Math. Naturwiss. Klasse,134, 165– 204.

1053 Falkowska, E. and T. Falkowski (2015), Trace metals distribution pattern in floodplain
1054 sediments of a lowland river in relation of contemporary valley bottom
1055 morphodynamics, *Earth Surf. Proc. Land.*, 40, 876-887, doi: 10.1002/esp.3680.

1056 Federici, B. and G. Seminara (2003), On the convective nature of bar instability, *J.*
1057 *Fluid Mech.*, 487, 125-145, doi:10.1017/S0022112003004737.

1058 Ferguson, R.I. and T.B. Hoey (2002), Long-term slowdown of river tracer pebbles:
1059 Generic models and implications for interpreting short-term tracer studies, *Water*
1060 *Resour. Res.*, 38(8), 1142, doi:10.1029/2001WR000637.

1061 Fredsøe, J. (1978), Meandering and braiding of rivers, *J. Fluid Mech.*, 84, 609-624,
1062 doi:10.1017/S0022112078000373.

1063 Furbish, D., P. Haff, J. Roseberry, and W. Schmeeckle (2012), A probabilistic

description of the bed load sediment flux: 1. Theory, *J. Geophys. Res.*, 117, F03031, doi: 10.1029/2012JF002352.

Ganti, V., M.M. Meerschaert, E. Foufoula-Georgiou, E. Viparelli, and G. Parker (2012), Normal and anomalous diffusion of gravel tracer particles in rivers, *J. Geophys. Res.*, 115, F00A12, doi:10.1029/2008JF001222.

Giri, S. and Y. Shimizu (2006), Numerical computation of sand dune migration with free surface flow, *Water Resour. Res.*, 42(10), doi: 10.1029/2005WR004588.

Hashenburger, J.K. (2013), Tracing river gravels: Insights into dispersion from a long-term field experiment, *Geomorphology*, 200, 121-131, doi:10.1016/j.geomorph.2013.03.033.

Hassan, M.A. and M. Church (1994), Vertical mixing of coarse particles in gravel bed rivers: A kinematic model, *Water Resour. Res.*, 30(4), 1173-1185, doi: 10.1029/93WR03351.

Hassan, M.A., H. Voepel, R. Schumer, G. Parker, and L. Fraccarollo (2013), Displacement characteristics of coarse fluvial bed sediment, *J. Geophys. Res.*, 118, 155-165, doi: 10.1029/2012JF002374.

Hirano, M. (1971), River bed degradation with armoring. *Proc., JSCE*, 195, 55–65. (in Japanese)

Hoey, T.B. (1996), Sediment dispersion and duration of storage in a model braided river, *J. Hydrol. NZ*, 35(2), 213-237.

Iwasaki, T., M. Nabi, Y. Shimizu, and I. Kimura (2015), Computational modeling of

1085 ^{137}Cs contaminant transfer associated with sediment transport in Abukuma River, *J.*
1086 *Environ. Radioactiv.*, 139, 416-426, doi:10.1016/j.jenvrad.2014.05.012.

1087 Iwasaki, T., Y. Shimizu, and I. Kimura (2016), Sensitivity of free bar morphology in
1088 rivers to secondary flow modeling: Linear stability analysis and numerical
1089 simulation, *Adv. Water Resour.*, 92, 57-72, doi:10.1016/j.advwatres.2016.03.011.

1090 Jang, C. and Y. Shimizu (2005), Numerical simulation of relatively wide, shallow
1091 channels with erodible banks, *J. Hydraul. Eng.*, 131(7), 565–575.
1092 doi:10.1061/(ASCE)0733-9429(2005)131:7(565).

1093 Kasprak, A., J.M. Wheaton, P.E. Ashmore, J.W. Hensleigh, and S. Peirce (2015), The
1094 relationship between particle travel distance and channel morphology: Results
1095 from physical models of braided rivers, *J. Geophys. Res.*, 120, 55-74,
1096 doi:10.1002/2014JF003310.

1097 Kovacs, A. and G. Parker (1994), A new vectorial bedload formulation and its
1098 application to the time evolution of straight river channels, *J. Fluid Mech.*, 267,
1099 153-183, doi:10.1017/S002211209400114X.

1100 Kuroki, M. and T. Kishi (1984), Regime criteria on bars and braids in alluvial straight
1101 channels, *Proc. of JSCE*, 342, 87-96. (in Japanese)

1102 Lajeunesse, E., L. Malverti, and F. Charru (2010), Bed load transport in turbulent flow
1103 at the grain scale: Experiments and modeling, *J. Geophys. Res.*, 115, F04001,
1104 doi:10.1029/2009JF001628.

1105 Lajeunesse, E., O. Devauchelle, M. Houssais, and G. Seizilles (2013), Tracer

1106 dispersion in bedload transport, *Adv. Geosci.*, 37, 1-6, doi:
1107 10.5194/adgeo-37-1-2013.

1108 Langendoen, E.J., A. Mendoza, J.D. Abad, P. Tassi, D. Wang, R. Ata, K. El Kadi
1109 Abderrezzak, and J. Hervouet (2016), Improved numerical modeling of
1110 morphodynamics of rivers with steep banks, *Adv. Water Resour.*,
1111 doi:10.1016/j.advwatres.2015.04.002.

1112 Lanzoni, S. and M. Tubino (1999), Grain sorting and bar instability, *J. Fluid Mech.*,
1113 393, 149-174, doi: 10.1017/S0022112099005583.

1114 Lanzoni, S. (2000), Experiments on bar formation in a straight flume. Part II: Graded
1115 sediment, *Water Resour. Res.*, 36(11), 3351-3363, doi: 10.1029/2000WR900161.

1116 Lauer, J.W. and G. Parker (2008), Modeling framework for sediment deposition,
1117 storage, and evacuation in the floodplain of a meandering river: Theory, *Water*
1118 *Resour. Res.*, 44, W04425, doi:10.1029/2006WR005528.

1119 Lesser, G.R., J.A. Roelvink, J.A.T.M. van Kester, G. Stelling (2004), Development
1120 and validation of a three-dimensional morphological model, *Coast. Eng.*, 51,
1121 883-915, doi:10.1016/j.coastaleng.2004.07.014.

1122 Lui, X.D., S. Osher, and T. Chan (1994), Weighted essentially non-oscillatory schemes,
1123 *J. Comput. Phys.*, 115, 200-212, doi:10.1006/jcph.1994.1187.

1124 Martin, R.L., D.J. Jerolmack, and R. Schumer (2012), The physical basis for
1125 anomalous diffusion in bed load transport, *J. Geophys. Res.*, 117, F01018, doi:
1126 10.1029/2011JF002075.

1127 Meyer-Peter, E. and R. Muller (1948), Formulas for bedload transport, IAHSR, Report
1128 on the second Meeting, 3, 39-64.

1129 Mosselman, E. and T.B. Le (2016), Five common mistakes in fluvial morphodynamic
1130 modeling, *Adv. Water Resour.*, doi:10.1016/j.advwatres.2015.07.025.

1131 Nabi, M., H.J. de Vriend, E. Mosselman, C.J. Sloff, and Y. Shimizu (2013a), Detailed
1132 simulation of morphodynamics: 3. Ripples and dunes, *Water Resour. Res.*, 49,
1133 doi:10.1002/wrcr.20457.

1134 Nabi, M., H.J. de Vriend, E. Mosselman, C.J. Sloff, and Y. Shimizu (2013b), Detailed
1135 simulation of morphodynamics: 2. Sediment pickup, transport, and deposition,
1136 *Water Resour. Res.*, 49, doi:10.1002/wrcr.20303.

1137 Nakagawa, H. and T. Tsujimoto (1980), Sand bed instability due to bed load motion,
1138 *Journal of the Hydraulics Division*, 106(12), 2029-2051.

1139 Nagata, N., T. Hosoda, and Y. Muramoto (2000), Numerical analysis of river channel
1140 processes with bank erosion, *J. Hydraul. Eng.*, 126(4), 243-252, doi:
1141 10.1061/(ASCE)0733-9429(2000)126:4(243).

1142 Nelson, J.M. (1990), The initial instability and finite-amplitude stability of alternate
1143 bars in straight channels, *Earth-Sci. Rev.*, 29, 97–115,
1144 doi:10.1016/0012-8252(0)90030-Y.

1145 Nelson, J.M., Y. Shimizu, T. Abe, K. Asahi, M. Gamou, T. Inoue, T. Iwasaki, T.
1146 Kakinuma, S. Kawamura, I. Kimura, T. Kyuka, R.R. McDonald, M. Nabi, M.
1147 Nakatsugawa, F.R. Simoes, H. Takebayashi, and Y. Watanabe (2016), The

International River Interface Cooperative: Public Domain Flow and Morphodynamics Software for Education and Applications, *Adv. Water Resour.*, doi:10.1016/j.advwatres.2015.09.017.

Nikora, V., H. Habersack, T. Huber, and I. EcEwan (2002), On bed particle diffusion in gravel bed flows under weak bed load transport, *Water Resour. Res.*, 38(6), doi: 10.1029/2001WR000513.

Olinde, L. and J.P.L. Johnson (2015), Using RFID and accelerometer-embedded tracers to measure probabilities of bed load transport, step lengths, and rest times in a mountain stream, *Water Resour. Res.*, 51, 7572-7589, doi: 10.1002/2014WR016120.

Parker, G. (1976), On the cause and characteristic scales of meandering and braiding in rivers, *J. Fluid Mech.*, 76, 457-480, doi:10.1017/S0022112076000748.

Parker, G., C. Paola, and S. Leclair (2000), Probabilistic Exner sediment continuity equation for mixtures with no active layer, *J. Hydraul. Eng.*, 126(11), 818-826, doi: 10.1061/(ASCE)0733-9429(2000)126:11(818).

Parker, G., G. Seminara, and L. Solari (2003), Bed load at low Shields stress on arbitrarily sloping beds: alternative entrainment formulation, *Water Resour. Res.*, 39, 1183-1192, doi: 10.1029/2001WR001253.

Pelosi, A., G. Parker, R. Schumer, and H.-B. Ma. (2014), Exner-Based Master Equation for transport and dispersion of river pebble tracers: Derivation, asymptotic forms, and quantification of nonlocal vertical dispersion, *J. Geophys.*

1169 *Res.*, 119, doi:10.1002/2014JF003130.

1170 Pelosi, A. and G. Parker (2014), Morphodynamics of river bed variation with variable
1171 bedload step length, *Earth Surf. Dynam.*, 2, 243-253.
1172 doi:10.5194/esurf-2-243-2014.

1173 Pelosi, A., R. Schumer, G. Parker, and R.I. Feruson (2016), The cause of advective
1174 slowdown of tracer pebbles in rivers: Implication of Exner based master equation
1175 for coevolving streamwise and vertical dispersion, *submitted to J. Geophys. Res.*,
1176 doi: 10.1002/2015JF003497

1177 Phillips, C.B., R.L. Martin, and D.J. Jerolmack (2013), Impulse framework for
1178 unsteady flows reveals super-diffusive bed load transport, *Geophys. Res. Lett.*, 40,
1179 1328-1333, doi: 10.1002/grl.50323.

1180 Pornprommin, A., N. Izumi, and T. Tsujimoto (2004), Weakly nonlinear analysis of
1181 multimodal fluvial bars, *Annual Journal of Hydraulic Engineering*, *JSCE*,
1182 1009-1014.

1183 Pornprommin, A. and N. Izumi (2011), Stability analysis of sand bars using amplitude
1184 expansion method, *Proceedings of 6th international symposium on River, Coastal*
1185 *and Estuarine Morphodynamics, RCEM2011*, Tsinghua University Press,
1186 1624-1638.

1187 Pyrce, R. and P. Ashmore (2003), The relation between particle path length
1188 distribution and channel morphology in gravel-bed streams: a synthesis,
1189 *Geomorphology*, 56, 167-187, doi:10.1016/S0169-555X(03)00077-1.

1190 Pyrce, R. and P. Ashmore (2005), Bedload path length and point bar development in
1191 gravel-bed river models, *Sedimentology*, 52, 839-857, doi:
1192 10.1111/j.1365-3091.2005.00714.x.

1193 Rodrigues, S., E. Mosselman, N. Claude, C.L. Wintenberger, and P. Juge (2015),
1194 Alternate bars in a sandy gravel bed river: generation, migration and interactions
1195 with superimposed dunes, *Earth Surf. Proc. Land.*, 40, 610-628,
1196 doi:10.1002/esp.3657.

1197 Roelvink, J.A. (2006), Coastal morphodynamic evolution techniques, *Coast. Eng.*, 53,
1198 277-287, doi;10.1016/j.coastaleng.2005.10.015.

1199 Roseberry, J.C., M.W. Schmeeckle, and D.J. Furbish (2012), A probabilistic
1200 description of the bed load sediment flux: 2. Particle activity and motions, *J.*
1201 *Geophys. Res.*, 117, F03032, doi:10.1029/2012JF002353.

1202 Sayre, W. and D. Hubbell (1965), Transport and dispersion of labeled bed material,
1203 North Loup River, Nebraska, *U.S. Geol. Surv. Prof. Pap.*, 433-C, 48pp.

1204 Schielen, R., A. Doelman, and H.E. de Swart (1993), On the nonlinear dynamics of
1205 free bars in straight channels, *J. Fluid Mech.*, 252, 325-356,
1206 doi:10.1017/S0022112093003787.

1207 Schmeeckle, M. (2014), Numerical simulation of turbulence and sediment transport of
1208 medium sand, *J. Geophys. Res.*, 119(6), 1240-1262, doi:10.1002/2013JF002911

1209 Schmeeckle, M. (2015), The role of velocity, pressure, and bed stress fluctuations in
1210 bed load transport over bed forms: numerical simulation downstream of a

1211 backward-facing step, *Earth Surf. Dynam.*, 3, 105-112, doi:
1212 10.5194/esurf-3-105-2015.

1213 Schumer, R., M.M. Meerschaert, and B. Baeumer (2009), Fractional
1214 advection-dispersion equations for modeling transport at the Earth surface, *J.*
1215 *Geophys. Res.*, 114, F00A07, doi:10.1029/2008JF001246.

1216 Schuurman, F., M.G. Kleinhans, and W.A. Marra (2013), Physics-based modeling of
1217 large braided sand-bed rivers: bar pattern formation, dynamics, and sensitivity, *J.*
1218 *Geophys. Res.*, 118, 2509-2527, doi:10.1002/2013JF002896.

1219 Schuurman, F., Y. Shimizu, T. Iwasaki, and M.G. Kleinhans (2016), Dynamic
1220 meandering in response to upstream perturbations and floodplain formation,
1221 *Geomorphology*, 253, 94-109, doi:10.1016/j.geomorph.2015.05.039.

1222 Shimizu, Y. and T. Itakura (1989), Calculation of bed variation in alluvial channel, *J.*
1223 *Hydraul. Eng.*, 115, 367-384. doi:10.1061/(ASCE)0733-9429(1989)115:3(367).

1224 Simons, D.B., E.V. Richardson, and C.F. Nordin Jr. (1965), *Bedload equation for*
1225 *ripples and dunes*, *U.S. Geol. Surv. Prof. Pap.*, *462-H*, 1-9.

1226 Stecca, G., A. Siviglia, and A. Blom (2014), Mathematical analysis of the
1227 Saint-Venant-Hirano model for mixed-sediment morphodynamics, *Water Resour.*
1228 *Res.*, 50, doi:10.1002/2014WR015251.

1229 Stecca, G., A. Siviglia, and A. Blom (2016), An accurate numerical solution to the
1230 Saint-Venant-Hirano model for mixed-sediment morphodynamics in rivers, *Adv.*
1231 *Water Resour.*, doi:10.1016/j.advwatres.2015.05.022.

1232 Takebayashi, H. and S. Egashira (2008), Non-equilibrium characteristics of bar
1233 geometry on bed with non-uniform sediment, *J. Hydrosci. Hydraul. Eng.*, 26(2),
1234 1-14.

1235 Tubino, M., R. Repetto, and G. Zolezzi (1999), Free bars in rivers, *J. Hydraul. Res.*,
1236 37(6), 759–775, doi:10.1080/00221689909498510.

1237 van der Mark, C.F., A. Blom, and S.J.M.H. Hulscher (2008), Quantification of
1238 variability in bedform geometry, *J. Geophys. Res.*, 113, F03020,
1239 doi:10.1029/2007JF000940.

1240 Viparelli, E., O.E. Sequeiros, A. Cantelli, P.R. Wilcock, and G. Parker (2010), River
1241 morphodynamics with creation/consumption of grain size stratigraphy 2:
1242 numerical model, *J. Hydraul. Res.*, 48(6), 727-741, doi:
1243 10.1080/00221686.2010.526759.

1244 Voepel, H., R. Schumer, and M.A. Hassan (2013), Sediment residence time
1245 distributions: Theory and application from bed elevation measurements, *J.*
1246 *Geophys. Res.*, 118, 2557-2567, doi: 10.1002/jgrf.20151.

1247 Watanabe, Y. (2007), A weakly nonlinear analysis of bar mode reduction process, *J.*
1248 *Hydrosci. Hydraul. Eng.*, 25(1), 107-122, doi: 10.2208/prohe.50.967.

1249 Weeks, E.R., J.S. Urbach, and H.L. Swinney (1996), Anomalous diffusion in
1250 asymmetric random walks with a quasi-geostrophic flow example, *Physica D*, 97,
1251 291-310, doi:10.1016/0167-2789(96)00082-6.

1252 Wong, M., G. Parker, P. DeVries, T. M. Brown, and S. J. Burges (2007), Experiments

on dispersion of tracer stones under lower-regime plane-bed equilibrium bed load transport, *Water Resour. Res.*, 43, W03440, doi:10.1029/2006WR005172.

Yabe, T., T. Ichikawa , P.Y. Wang, T. Aoki, Y. Kadota, and F. Ikeda (1991), A universal solver for hyperbolic equations by Cubic-Polynomial Interpolation II. two and three-dimensional solvers, *Comput. Phys. Commun.*, 66(2-3), 233-242, doi:10.1016/0010-4655(91)90072-S.

Yamaguchi, S., Y. Shimizu, I. Kimura, and S. Giri. (2009), Significance of bed slope effect and non-equilibrium sediment transport on bed form evolution process: A numerical analysis using detailed hydrodynamics, Proceedings of the 6th IAHR symposium on River, Coastal and Estuarine Morphodynamics (RCEM2009), *Universidad Nacional Del Litoral, Santa Fe*, *Argentina*, *21-25*, September, 2009, 659-666.

Yang, C.T., and W.W. Sayre (1971), Stochastic model for sand dispersion, *Proc. ASCE*, *Journal of the Hydraulics Division*, 97(2), 265-288.

Zhang, Y., M.M. Meerschaert, and A.I. Packman (2012), Linking fluvial bed sediment transport across scales, *Geophys. Res. Lett.*, 39, L20404, doi:10.1029/2012GL053476.

Zolezzi, G., R. Luchi, and M. Tubino (2012), Modeling morphodynamic processes in meandering rivers with spatial width variations, *Rev. Geophys.*, 50, 1-24, doi: 10.1029/2012RG000392.

1274

1275

1276

1277 **Tables**

Table 1. Nondimensional parameters for the sensitivity analysis of tracer advection-dispersion associated with free bars.

	Froude number, F_r	Shields number, θ	Width/depth, β
Case 1	0.85	0.095	41.7
Case 2	0.6	0.095	41.7
Case 3	0.45	0.095	41.7
Case 4	0.6	0.075	41.7
Case 5	0.6	0.141	41.7
Case 6	0.6	0.095	33.3
Case 7	0.6	0.095	50

1278

1279

Table 2. Tracer plume transport characteristics: asymptotic advection velocity with respect to initial velocity and the scaling exponent, γ, in the relationship, $\sigma \sim t^{\gamma}$.

	Asymptotic velocity/initial velocity (%)	Scaling exponent, γ
Case 1	6.1	0.69
Case 2	2.6	0.59
Case 3	1.2	0.52
Case 4	3.1	0.63
Case 5	1.5	0.50
Case 6	2.8	0.55
Case 7	2.3	0.59

1285 **Figures**

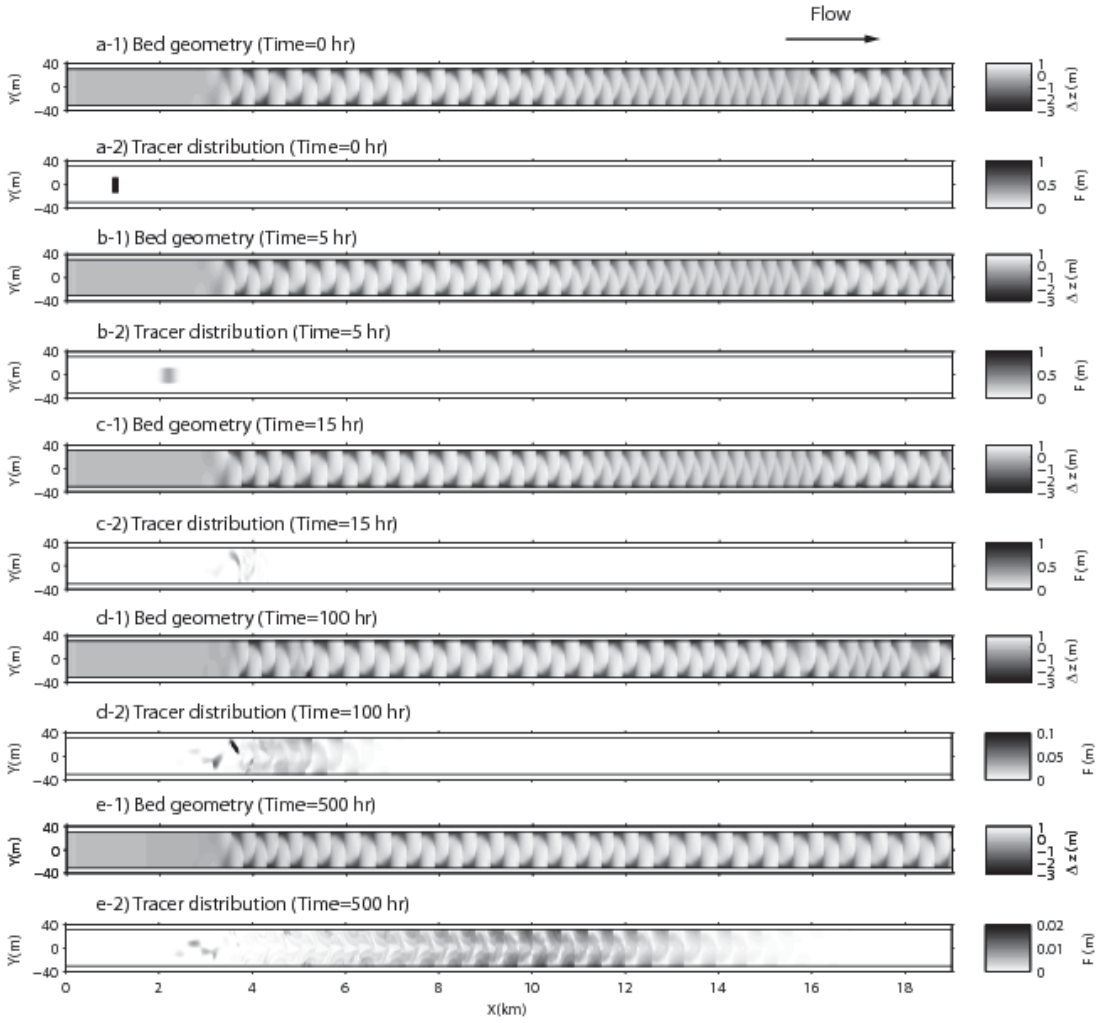

Figure 1. Temporal changes of alternate bar morphology and tracer distribution simulated by the entrainment-based model. Hydraulic conditions are: $F_r = 0.85$, $\theta = 0.095$, $S = 0.00461$, and $\beta = 41.7$. Flow is from left to right. A detailed view of the spatiotemporal evolution of bar morphology and tracer concentration can be seen in Video S1, a link to which is given in the Supporting Information.

1286

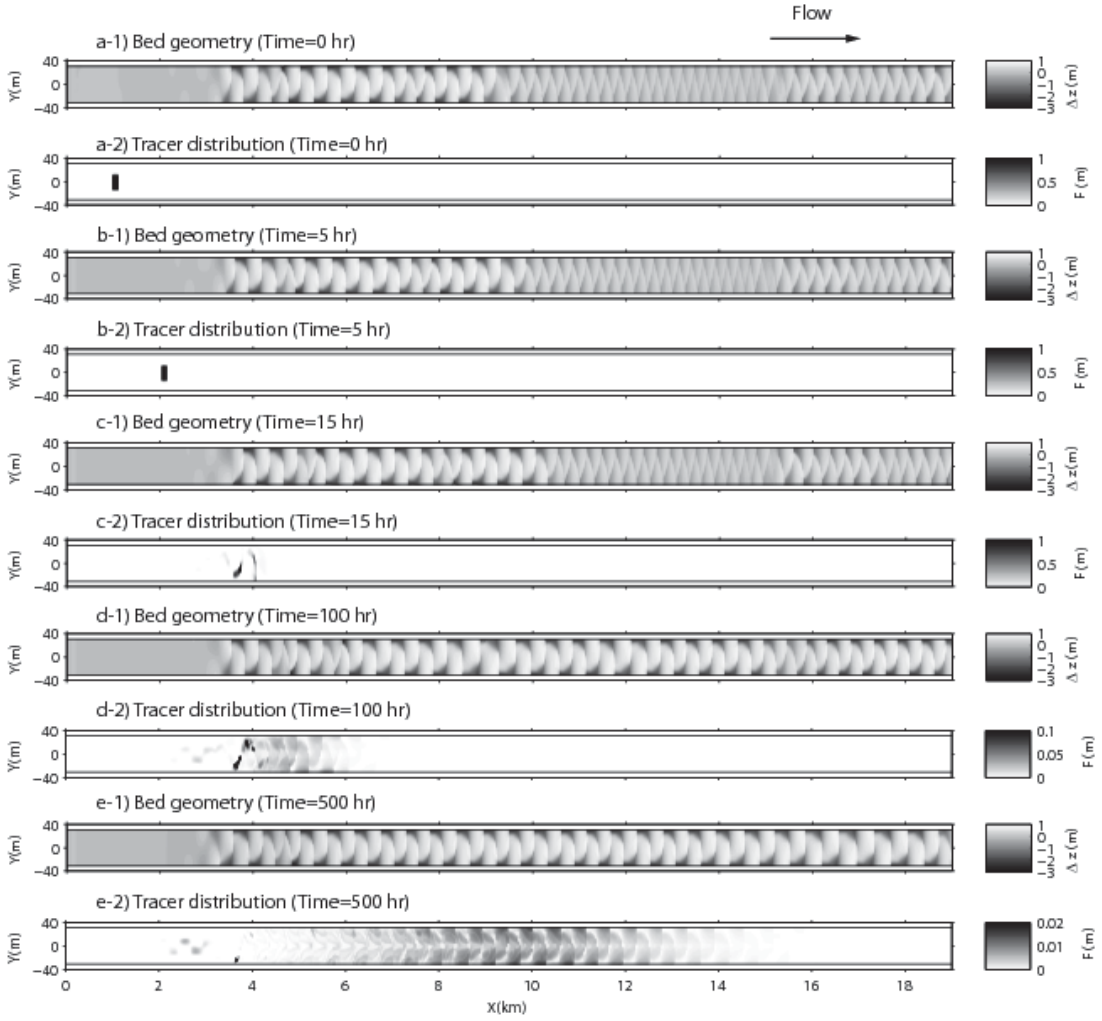

Figure 2. Temporal changes of alternate bar morphology and tracer distribution simulated by the flux-based model. Hydraulic conditions are: $F_r = 0.85$, $\theta = 0.095$, $S = 0.00461$, and $\beta = 41.7$. Flow is from left to right. Details of the spatiotemporal evolition of bar morphology and tracer concentration can be seen in Video S1 in the Supporting Information.

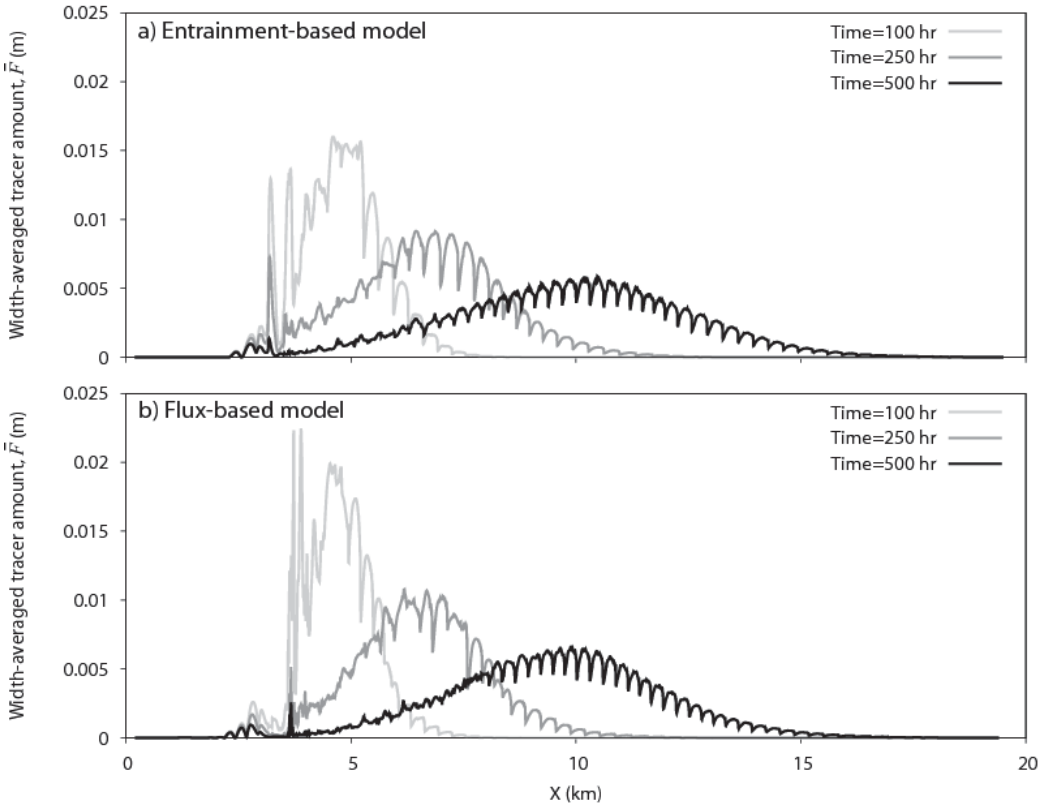

Figure 3. Temporal change of the width-averaged tracer amount $\bar{F}$ in the longitudinal direction, as simulated by a) the entrainment-based model and b) the flux-based model. Flow is from left to right.

1290

1291

1292

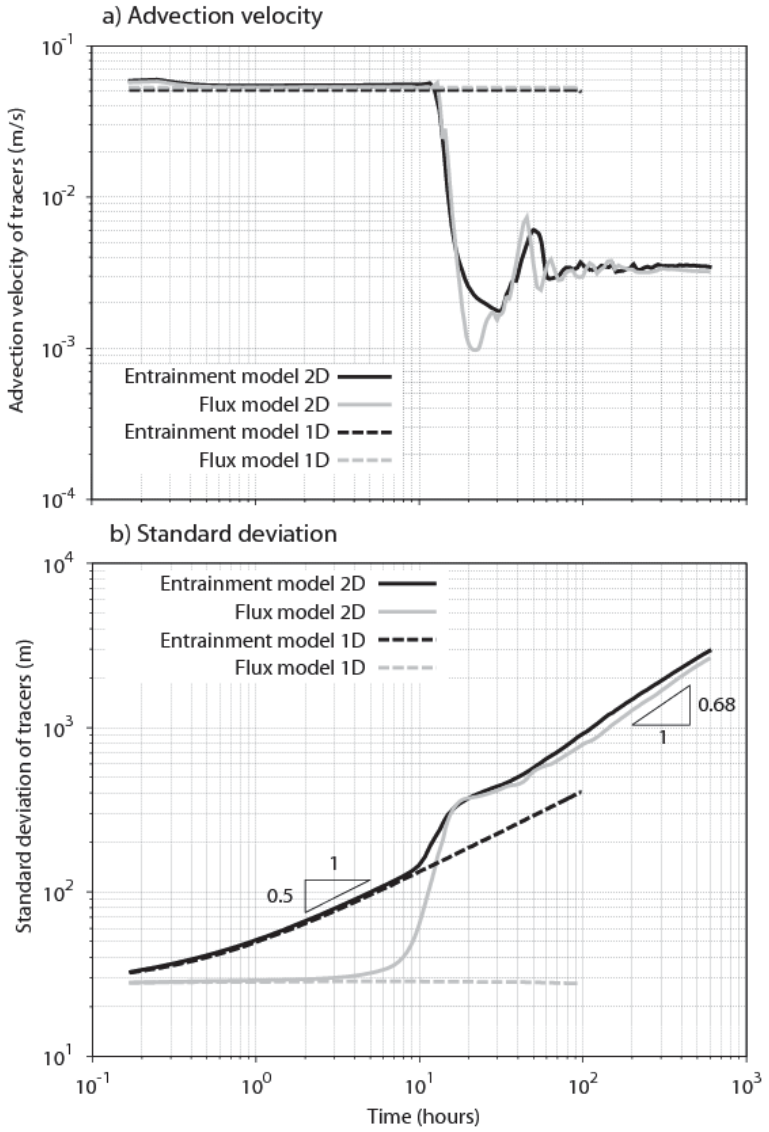

Figure 4. a) Advection velocity and b) standard deviation of the plume of tracers in the longitudinal direction. The dashed and solid lines represent the 1D and 2D calculations, respectively, and the black and gray lines denote the entrainment- and flux-based models, respectively.

1293

1294

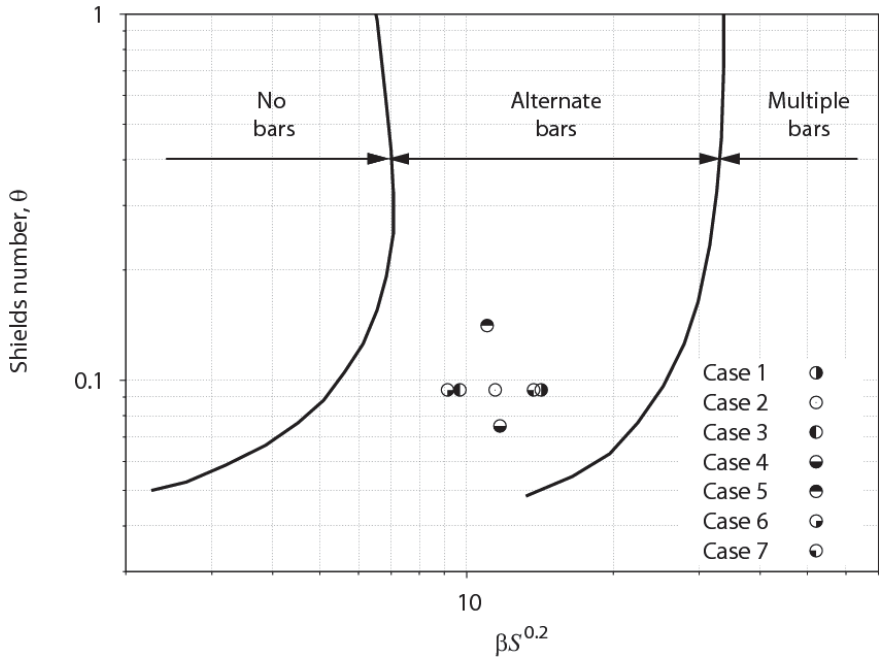

Figure 5. Regime criteria of free bar mode based on a linear stability analysis [*Kuroki and Kishi*, 1984]. All runs performed for the sensitivity analysis are categorized in the single-row alternate bar regime.

1295

1296

1297

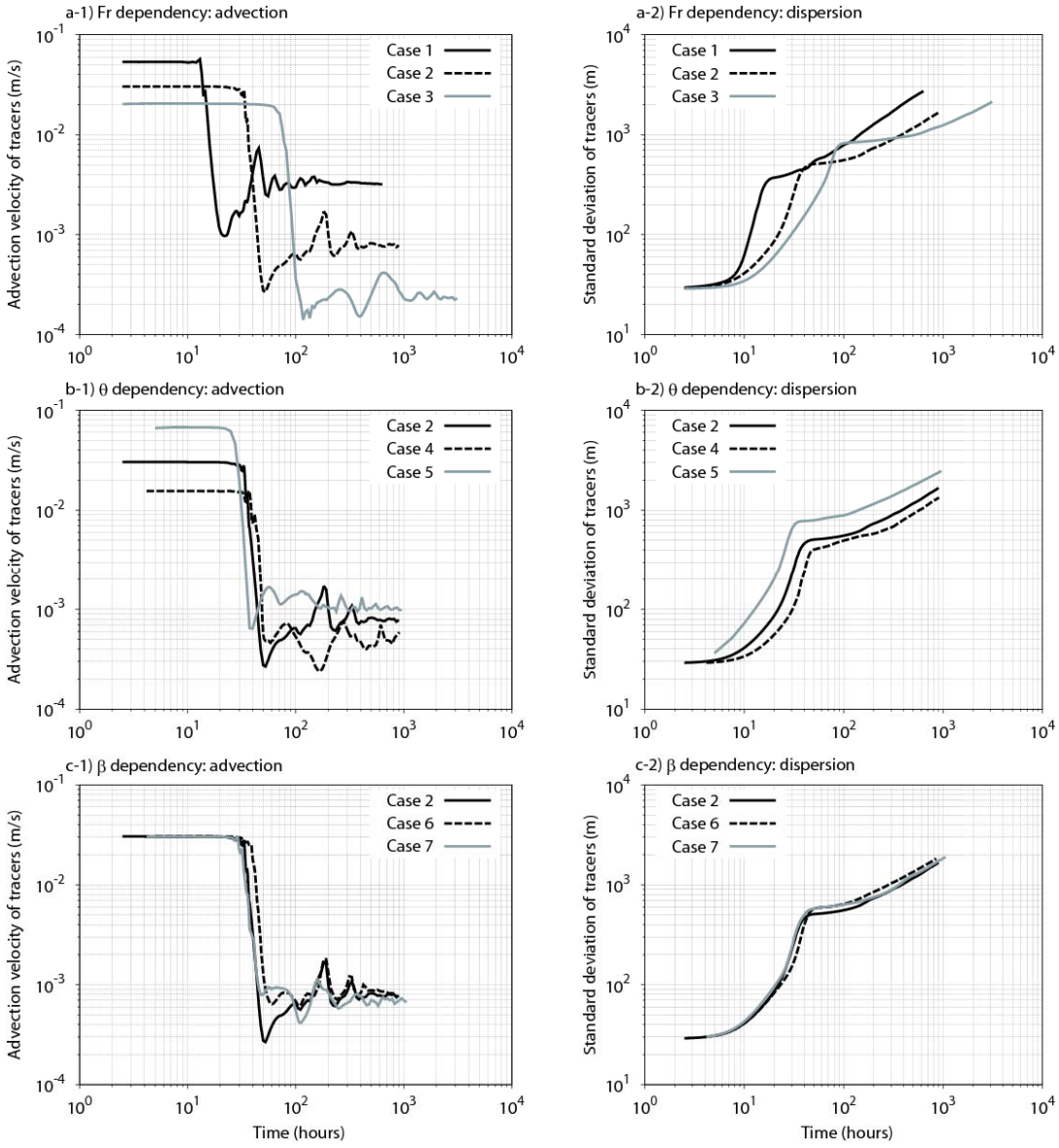

Figure 6. Sensitivity analysis of advection and dispersion characteristics. The figures in the left and right columns show the advection velocity and standard deviation of the tracer plume, respectively. The notations a), b), and c) in the upper left-hand side of each panel indicate that variation in Froude number *Fr*, Shields number θ, and width/depth ratio β, respectively, are studied.

1298

1299

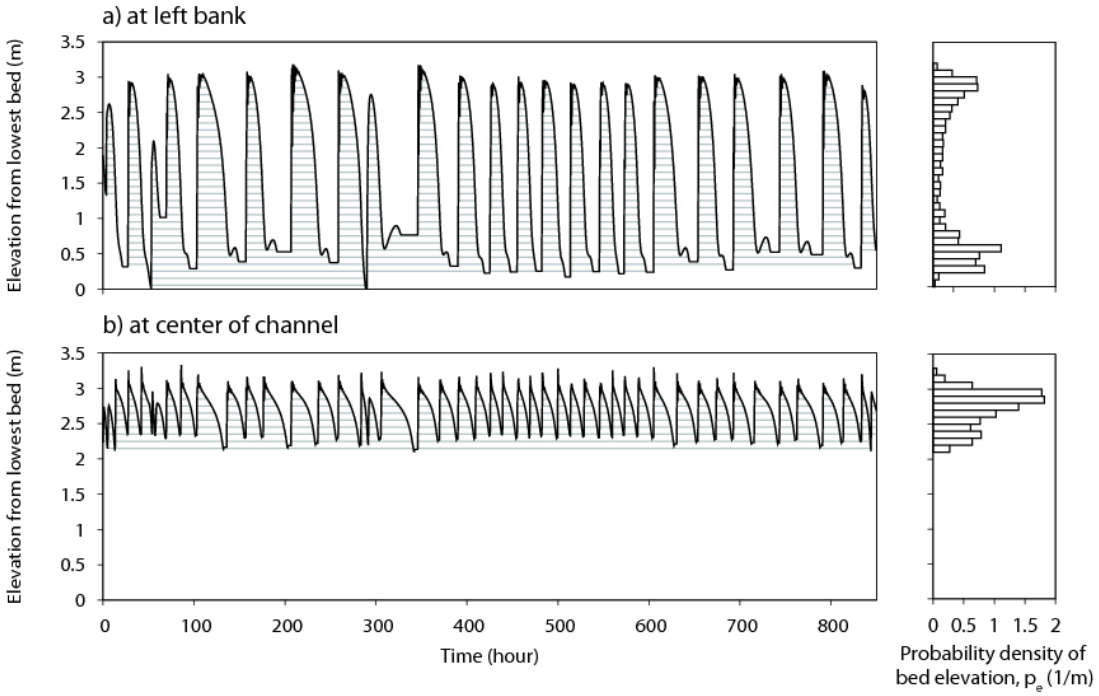

Figure 7. Time series of bed surface elevation (black line) and the corresponding waiting time (gray line) (left), and the probability of bed surface elevation (right) at the a) left bank and b) center of the channel in Case 1.

1300

1301

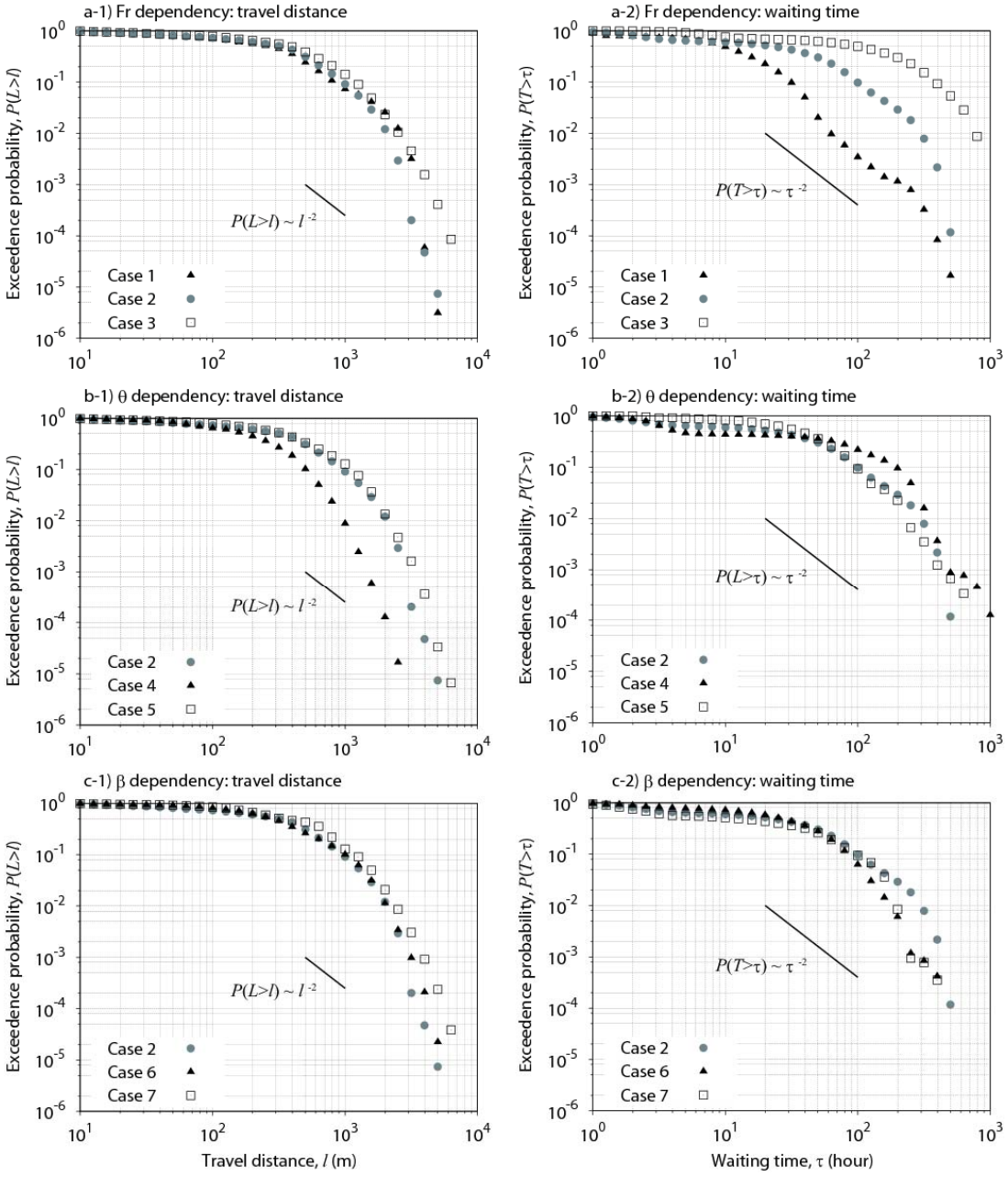

Figure 8. Exceedance probability distribution of the travel distance (a-1, 2, 3) and waiting time (b-1, 2, 3) in each the seven numerical runs.

1302

1303

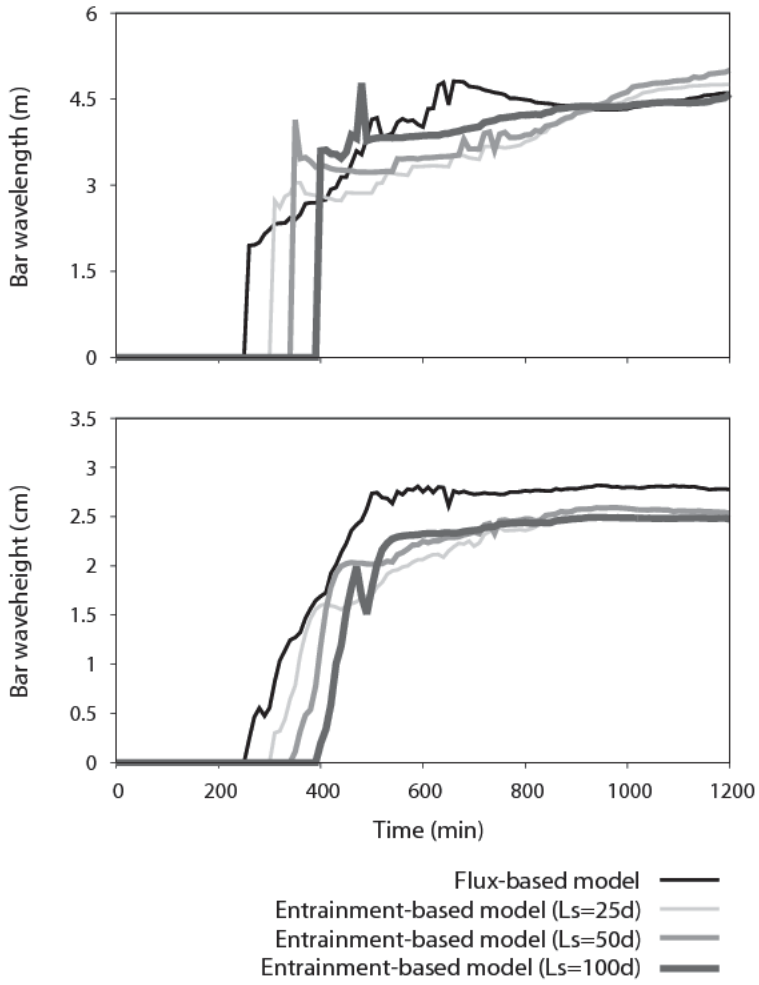

Figure A1. Sensitivity of the simulated free bar dimensions, i.e., wavelength (top), and b) wave height (bottom), to the type of morphodynamic model (flux or entrainment) and mean step length.

1304

Using bioavailability to assess pyrethroid insecticide toxicity in urban sediments

Basic Information

Title:	Using bioavailability to assess pyrethroid insecticide toxicity in urban sediments
Project Number:	2015IL298G
USGS Grant Number:	G15AS00019
Start Date:	9/1/2015
End Date:	8/31/2018
Funding Source:	104G
Congressional District:	IL012
Research Category:	Water Quality
Focus Category:	Models, Sediments, Toxic Substances
Descriptors:	None
Principal Investigators:	Michael j Lydy, Amanda D Harwood, Kara Elizabeth Huff Hartz, Samuel A Nutile

Publications

There are no publications.

Progress Report 5/15/17 for NIWR 104G:
"Using bioavailability to assess pyrethroid insecticide toxicity in urban sediments"
Michael Lydy and Kara Huff Hartz

Problem and Research Objectives

The following report summarizes the activities conducted in the Lydy Research lab from 3/1/2016 to 2/28/2017 as part of the NIWR/USGS grant titled "Using bioavailability to assess pyrethroid insecticide toxicity in urban sediments." The grant aims to study pyrethroid insecticide contamination in urban streams in the northeastern United States. In particular, the objectives of this portion of the project were to receive sediment subsamples collected as part of the Northeast Stream Quality Assessment (NESQA), determine the pyrethroid concentrations in those sediments using single-point Tenax and exhaustive chemical extractions, conduct 10-day bioassays with *Hyalella azteca* using the sediments, and run focused toxicity identification evaluations (fTIEs) to confirm pyrethroid toxicity. In addition, in a preliminary project, we used single-point Tenax extractions to determine the effect of standard holding time procedures on the bioaccessible pyrethroid concentrations in sediment.

Methodology

To measure bioaccessible pyrethroids, single-point Tenax extractions were performed on sediments in quadruplicate. Tenax extraction, sample cleanup, and gas chromatography/mass spectroscopy analysis were conducted using methods previously developed in our laboratory (Nutile et al., 2016). Briefly, 0.5 of Tenax sorbent, 3 g (dry weight) of sediment, 4.5 mg of mercury (II) chloride to inhibit microbial growth, and 45 mL of reconstituted moderately hard water (RMHW) (Ivey and Ingersoll, 2016) were rotated at 21 rpm to sorb bioaccessible pyrethroids from the sediment onto the Tenax. After 24 h, the Tenax was removed, recovery surrogate compounds (40 ng of dibromooctafluorobiphenyl (DBOFB) and decachlorobiphenyl (DCBP)) were added to the Tenax, and the pyrethroids were extracted from the Tenax using acetone/hexane and hexane solvent washes. The extract was cleaned up using a sodium sulfate column, placed in a vial, and brought to a 0.5 mL volume in acidified (0.1% acetic acid) hexane.

In addition, the exhaustively extracted pyrethroids were measured in all sediments to determine the total pyrethroid contamination in the sediment using methods previously developed in our laboratory (You et al., 2008; Nutile et al. 2016). Briefly 3 g of freeze-dried sediment and 5 g of silica gel were placed in an accelerated solvent extraction cell along with filler sand and a glass fiber filter. The cell was spiked with recovery surrogate compounds (50 ng of DBOFB and DCBP). Pyrethroids were extracted from sediment by pressurized liquid extraction using a Dionex 200 Accelerated Solvent Extraction (ASE) using 1:1 dichloromethane:acetone at 100 ^{o}C and 1500 pounds per square inch which was held for two heat-static cycles of 10 minutes each. After extraction, extracts were solvent changed to hexane, cleaned up using Supelclean ENVI-Carb-II/PSA 300/600 mg solid-phase extraction cartridges and 1 g of sodium sulfate (previously dried at 400 ^{o}C for 4 hours). Extracts were solvent changed to hexane, transferred to a GC vial, and evaporated to a final volume of 1 mL, and acidified to 0.1 % using acetic acid.

The pyrethroid concentration in the Tenax and exhaustive extract were measured for nine pyrethroids (tefluthrin, fenpropathrin, bifenthrin, cyhalothrin, permethrin, cyfluthrin, cypermethrin, esfenvalerate, and deltamethrin) using an Agilent 7890A gas chromatography equipped with an Agilent 5975A inert XL mass spectrometer (Nutile et al. 2016). Pyrethroids and surrogate concentrations were determined using internal standard calibration and normalized for dry weight organic carbon. Quality assurance/quality control samples were prepared analyzed along with the Tenax and exhaustive extracts, and these consisted of blank and spiked samples prepared with reference sediment as well as spiked field sediment.

Hyalella azteca 10-d toxicity bioassays followed those outlined by the USEPA (2000). Briefly, 100 mL of sediment (four replicates) were distributed into 300-mL glass jars, covered with overlying RMHW and

allowed to settle for 24 hours at 23°C. After sediment settled, ten 7- to 8-d old *H. azteca* were added to each test jar containing the sediment, as well as sand and LaRue Pine Hills control sediment. The test jars were housed in an automated water renewal system maintained at 23°C with four automatic water renewals (100 mL/test jar/renewal) performed daily for the duration of the test. Organisms were fed a diet consisting of a Tetramin suspension and diatoms (*Thalassiosira weissflogii,* Ivey et al. 2016). After 10 days, the test organisms were removed from the jars, and two endpoints (% survival and biomass) were recorded. Toxic sediments were identified according to significantly lower survival and biomass compared to the control and reference sediments. Quality assurance measures included initial and final biomass of the organisms in the control and reference sediment and >80% survival in these same sediments.

Sediments with significant toxicity and quantifiable pyrethroid concentrations in the Tenax extracts were selected for fTIE in order to confirm pyrethroids as the cause of sediment toxicity. Simultaneous bioassays at 17 ºC and 23 ºC were conducted using protocols following from Weston and Lydy (2010). The 7-14 d old *H. azteca* were first acclimated in a plastic tub at their respective test temperature for at least 12 h prior to use. The fTIE procedures followed the same procedure as the bioassays, and the 10-d biomass and % survival were the measured endpoints. Pyrethroid toxicity was confirmed when the 17 ºC biomass or % survival was significantly lower than the 23 ºC biomass or % survival relative to their respective controls. Note that due to limited sample volume, the other tier II fTIE tests (piperonyl butoxide exposure) were not conducted.

Principal Findings

A total of 49 sediments were received from USGS, and these were collected in August and October 2016 from streams in the northeastern United States. Pyrethroids were detected in sediments extracted by Tenax in 67% of the samples and by exhaustive extraction in 78% of the samples (Table 1). Forty out of 49 of the streams were classified as urban according to the portion of developed land use in the watershed (Homer et al. 2015). Sediments from sites with urban influence tended to show more frequent pyrethroid detections. Of the nine pyrethroids quantified, bifenthrin was the most commonly detected (Table 2) in Tenax and exhaustive chemical extractions, and this was consistent with pyrethroid occurrence in other streams in metropolitan areas (Kuivala et al. 2012). Cyhalothrin, cyfluthrin, and cypermethrin were also commonly found in stream sediments. The detection frequency of all pyrethroids was consistently lower for Tenax extraction than for exhaustive extraction, and this was because Tenax selectively samples the pyrethroid in the bioaccessible portion of the sediment.

Biossays (10-d *H. azteca*) were conducted on 46 sediments of the 49 sediments received. The remaining three sediments were received after the bioassays were completed, and because the Tenax extraction and exhaustive chemical extraction showed little-to-no pyrethroid contamination, toxicity bioassays were not conducted on these sediments. We estimate the *H. azteca* survival was impaired in nine sediments (20%) and that *H. azteca* growth was impaired in 13 sediments (28%). The frequency of sediments showing toxicity in northeastern U.S. urban streams was comparable to urban streams in other metropolitan areas. For example, 26% of the sediments collected from seven U.S. metropolitan areas caused impaired survival to *H. azteca* in 28-d tests (Kuivala et al. 2012).

Focused TIEs were conducted to confirm pyrethroids as the source of toxicity to *H. azteca*. Eleven sediments that showed toxicity in the 10-d bioassays and had quantifiable pyrethroids in the Tenax extractions were selected for fTIE tests. Seven of the eleven sediments (63%) showed lower % survival at 17 ºC exposure in comparison to 23 ºC exposure. Lower survival at lower exposure temperature is associated with pyrethroid-induced mortality (Weston and Lydy, 2010), and this finding suggests that pyrethroids were the cause of the noted toxicity in our current study.

Although we frequently detected pyrethroids by exhaustive extraction in NESQA samples, fewer sediments were acutely toxic or inhibited *H. azteca* growth. Tenax pyrethroid concentrations were consistently lower than exhaustive chemical concentrations, and the lower toxicity to *H. azteca* despite the higher detection rate in the ASE sediment was most likely due to low bioaccessible pyrethroids in NESQA sediments, as indicated by the Tenax extractions. In addition, the fTIE tests reveals that pyrethroids were a major contributing factor in seven out eleven sediments with toxicity. This suggests that pyrethroid contamination is an important contributing factor to sediments in northeastern urban streams. Currently, we are completing our quality assurance checks of the data and awaiting the completion of the bioassay results from USGS Columbia Environmental Research Center (CERC). After receiving these data, we will compare USGS-CERC bioassay results (28-H. azteca and 28-d *H. azteca*, 10-d *Chironomus dilutus*, and 28-d *Lampsilis siliquoidea* toxicity tests) to our 10-d *H. azteca*. We plan to correlate Tenax pyrethroid concentrations as toxic units with bioassay toxicity, and assess the ability of a Tenax extraction/fTIE approach to predict pyrethroid toxicity in urban sediment.

In a separate holding time study that was previously introduced in our first report, Tenax extraction was used to determine the stability of sediment stored using standard protocols (at 4 ºC). The data suggested that the bioaccessible fraction of pyrethroids in sediment decreases as a function of holding time (Figure 1). We can rule out pyrethroid degradation or sorption to the storage container, because the exhaustive extractive pyrethroid concentrations were stable relative to Tenax pyrethroid concentrations. This finding will not impact the correlation of our current work with the USGS dataset because we used standard sediment holding time practices and we coordinated our bioassay and Tenax extraction start dates with USGS-CERC. However, if we postulate that bioaccessible pyrethroids directly correlates with sediment toxicity, standard holding time procedures (store sediments 30 days at 4 ºC before beginning bioassays) may cause an under-prediction of sediment toxicity due to pyrethroid contamination. We have requested supplemental funding to repeat the holding time study, and we plan to use sediment from additional sites and incorporate the direct toxicity tests. This work will begin approximately May 1st, 2017, and will be discussed in the year 2 report.

Finally, the year 2 work objective is to assess the presence of pyrethroid resistance in field *H. azteca* in the northeastern United States. We plan to correlate our pyrethroid sediment and toxicity data with the *H. azteca* biosurvey data that is currently being processed by the USGS. Sites that contain pyrethroids in the sediment, demonstrate toxicity in bioassays, and indicate the presence of *H. azteca* in the biosurveys will be selected for further sediment analysis and *H. azteca* collection in the summer 2017. Currently, we are identifying sites that are likely good targets with our current data set and using historical data from the National Water Quality Monitoring Council Water Quality Portal.

Significance

Our results to date offer contributing evidence that pyrethroid contamination is an important source of toxicity to sediment-dwelling organisms in urban streams. Pyrethroid concentrations measured by Tenax extraction may be a more accurate predictor of pyrethroid toxicity than pyrethroid concentrations measured using exhaustive chemical extraction, because Tenax more appropriately samples the portion of the sediment that is bioaccessible and therefore susceptible to invertebrate exposure. The results of the holding time study indicate that longer sediment holding times cause an underestimation of the Tenax pyrethroid concentrations, but the work supported by our supplemental funding is needed to show that this correlates to an under-prediction of toxicity in lab bioassays. Finally, future work is needed to determine if sediment holding time procedures cause an underestimation of toxicity relative to the field, but this beyond the scope of the current projects.

Students supported and education level (undergrad, MS, PhD, Post Doc)

This project supported two undergraduate and three graduate students. Andrew Derby and Haleigh Sever (undergraduate students) cultured *H. azteca* for bioassays and provided assistance when the experiments

were conducted by preparing for experiments (sample receipt, logging, and sub-sampling, glassware and equipment preparation) and data collection. Courtney Y. Fung (MS student) prepared the same-day age *H. azteca* used in the toxicity bioassays, she conducted the bioassays and fTIEs, and provided assistance during sub-sampling. Jennifer Heim (MS student) helped conduct the bioassays and fTIEs and provided culturing support. Federico Sinche (PhD student) served as lead for the Tenax extractions and extract cleanup, and he helped conduct the bioassay experiments. Sam Nutile (PhD student) served as bioassay lead, and he helped conduct the Tenax extractions.

Publications

Data collection and analysis is in progress for this project, and we anticipate submitting the following articles for publication:

1) "Effect of Sample Holding Time on Pyrethroid and Polychlorinated Biphenyl Sediment Assessments: Application of Single-Point Tenax Extractions." Target publication: *Environmental Pollution*

2) "Occurrence of Bioaccessible Pyrethroid Insecticides in Urban Stream Sediments in the Northeastern United States" Target publication: *Environmental Science & Technology*

3) "Comparison of Single-Point Tenax Extraction to Toxicity Bioassays for Sediment Assessments" Target publication: *Environmental Toxicology and Chemistry*

References Cited

Homer CG, Dewitz JA, Yang L, Jin S, Danielson P, Xian G, Coulston J, Herold ND, Wickham JD, Megown K 2015. Completion of the 2011 National Land Cover Database for the conterminous United States-Representing a decade of land cover change information. *Photogrammetric Engineering and Remote Sensing*, 81(5): 345-354

Ivey CD, Ingersoll CG 2016. Influence of bromide on the performance of the amphipod *Hyalella azteca* in reconstituted waters. *Environ. Chem. Toxicol*. 35(10): 2425-2429.

Ivey CD, Ingersoll CG, Brumbaugh WG, Hammer EJ, Mount DR, Hockett JR, Norberg-King TJ, Soucek D, Taylor L 2016. Using an interlaboratory study to revise methods for conducting 10-d to 42-d water or sediment toxicity tests with *Hyalella azteca. Environ Toxicol Chem.*35(10): 2439-2447.

Kuivila KM, Hladik ML, Ingersoll CG, Kemble NE, Moran PW, Calhoun DL, Nowell LH, Gilliom RJ 2012. Occurrence and potential sources of pyrethroid insecticides in stream sediments from seven U.S. metropolitan areas. *Environ. Sci. Technol*. 46(8) 4297-4303.

Nutile SA, Harwood AD, Sinche FL, Huff Hartz KE, Landrum PF, Lydy MJ. The robustness of single-point Tenax extractions of pyrethroids: Effects of the Tenax to organic carbon mass ratio on exposure estimates. *Chemosphere* 171: 308-317.

Weston DP, Lydy MJ 2010. Focused toxicity identification evaluations to rapidly identify the cause of toxicity in environmental samples. *Chemosphere* 78: 368-374.

[USEPA] US Environmental Protection Agency 2000. Methods for measuring the toxicity and bioaccumulation of sediment-associated contaminants with freshwater invertebrates. EPA600/R-99/064. Washington, DC.

You J, Weston DP, Lydy ML 2008. Quantification of pyrethroid insecticides at sub-ppb levels in sediment using matrix-dispersive accelerated solvent extraction with tandem SPE cleanup. In *Synthetic Pyrethroids* ACS Symposium Series, Vol. 991 Chapter 5, pp 87–113.

Table 1: Land use and pyrethroid detection in NESQA sediment

		% of Sediments	
Land Use Category	Number of Sediments	Bioaccessible (Tenax)	Exhaustive Extraction
Forested (reference)	4	0%	25%
Agriculture	5	20%	20%
Urban (Tier 1)	40	80%	90%
All Categories	49	67%	78%

Table 2: Pyrethroid detection in NESQA sediment

	% of Sediments	
Pyrethroid	Bioaccessible (Tenax)	Exhaustive Extraction
Tefluthrin	12%	20%
Bifenthrin	65%	78%
Fenpropathrin	0%	4%
Cyhalothrin	47%	69%
Permethrin	10%	37%
Cyfluthrin	24%	53%
Cypermethrin	20%	49%
Esfenvalerate	4%	16%
Deltamethrin	2%	16%

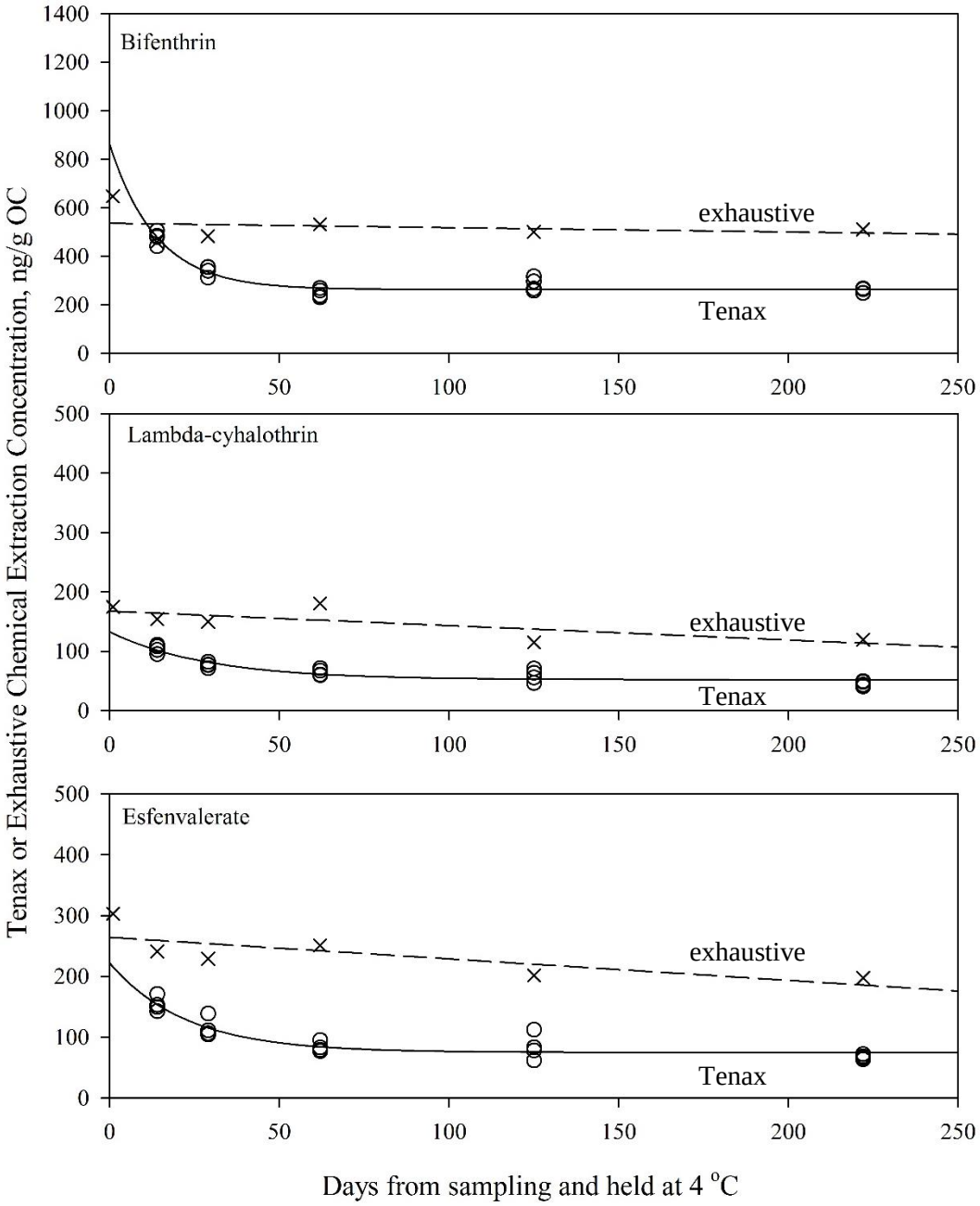

Figure 1: Tenax extraction (o) and exhaustive chemical extraction (×) bifenthrin, lambda-cyhalothrin, esfenvalerate concentrations as a function of days held at 4 °C after sampling at Ingram Creek, CA. Tenax concentrations were fit (solid line) to an exponential equation $C_t = \Delta C e^{-kt} + C_f$ where C_t was the Tenax concentration at time t, ΔC was the change in Tenax concentration, k was the first-order rate constant, and C_f was the final Tenax concentration. Exhaustive chemical extraction concentrations were fit (dashed line) to a linear equation C_t= slope × t + C_i where C_i = initial exhaustive chemical extraction concentration.

Identifying wetland inundation extent and patterns in Illinois

Basic Information

Title:	Identifying wetland inundation extent and patterns in Illinois
Project Number:	2016IL311B
Start Date:	3/1/2016
End Date:	2/28/2018
Funding Source:	104B
Congressional District:	IL-12
Research Category:	Biological Sciences
Focus Category:	Wetlands, Floods, Ecology
Descriptors:	None
Principal Investigators:	Michael W Eichholz

Publications

There are no publications.

Identifying wetland inundation extent and patterns in Illinois

Category: Biological Sciences

Wetland inundation, habitat availability, wetland resources, water allocation

Michael W. Eichholz, Ph.D.
Avian/Wetland Ecologist, Associate Professor
Southern Illinois University Carbondale
Cooperative Wildlife Research Laboratory
eichholz@siu.edu
(618) 453-6951

Congressional District: IL-12

Problem

Continued increase in human population combined with increasing climatic variability associated with climate change will likely exacerbate future demands on our limited water supply throughout North America. Managing water for wildlife is one of several competing interests for limited water resources. Maximizing efficiency of water use for wildlife will require precise knowledge of wildlife habitat requirements and how those requirements vary throughout the annual cycle. For example, the hydrologic variation of wetlands makes them the most productive habitat in our ecosystem (Mitsch and Gosselink 2000, Batzer and Sharitz 2006). This same hydrologic variation, however, often limits the availability of resources provided by wetlands to wetland-dependent organisms in that wetlands may be dry when organisms are most dependent on them (Batzer and Sharitz 2006). This variation of inundation in wetlands makes accurately developing restoration goals based on the resource needs of wildlife populations difficult.

The National Wetlands Inventory provides an estimate of the total acreage of wetlands, but we are currently unable to estimate the acreage of wetlands that are inundated by water in a given time period. In the upper Midwest region, February-March, May-July and August-September are the most biologically important time periods for waterfowl, breeding wading birds and shorebirds, respectively. Estimates of inundation during those periods will allow for more precise allocation of water to provide habitat for those groups.

The location of inundation is also important if it is to provide resources to those groups. Directly monitoring inundation at all of the state's wetlands via ground survey is unfeasible on a seasonal or annual basis. Traditional remote sensing techniques such as aerial and optical imagery are unable to detect inundation in heavily vegetated areas. Classification error in the NWI can be exaggerated by vegetation cover type, with classifications of forested wetlands often having the highest error (Kudray and Gale 2000). Considering that Illinois has lost over 85% of its historical wetland area, with palustrine wetlands most heavily impacted (Dahl and Allord 1996), it is crucial to develop a method to estimate the availability of remaining wetlands to inundation-dependent species.

By developing models to estimate seasonal wetland inundation at the state level, this study could be used to develop more accurate wetland protection and restoration goals, allowing more efficient use of limited water resources for wildlife. Further, the estimates of wetland inundation obtained may be used as baselines to detect changes in the availability of water resources in wetlands in the future.

Project objectives and scope

This project aims to develop models to estimate wetland inundation for the entire state of Illinois. Two different approaches are being used to reach these ends.

Objective 1 will use ground surveys to estimate the seasonal changes in inundation and NWI error at random sites and then scale those values to the statewide NWI layers. This will provide an estimate of total wetland inundation in the state, specific to wetland type. Objective 1 constitutes a portion of a larger project which is funded by Federal Grant-in-Aid W-184-R-1-4 in

cooperation with IDNR. That project also includes quality assessments of the areas determined to be inundated. Habitat quality will be determined using several metrics including vegetation sampling and stress indicators, and will be analyzed by a Master's student at the University of Illinois under the advisement of Heath M. Hagy, Director of Illinois Natural History Survey's Forbes Biological Station.

Objective 2 will utilize satellite-based synthetic aperture radar (SAR) imagery to detect inundation on a larger scale and use the results from that analysis to model inundation patterns in the state. Unlike optical methods such as Landsat, L-band SAR can penetrate the forest canopy, and C-band SAR can penetrate emergent vegetation. The intensity of the radar return and polarity shifts in the radiation are used to estimate the presence of inundation (Lang et al. 2008). Imagery resolutions range from 3 meters to 100 meters. Funds to purchase imagery for preliminary analyses have been provided by the Upper Mississippi River and Great Lakes Joint Venture. Technical assistance with imagery processing and analysis will be provided by Donald Atwood, Senior Research Scientist at Michigan Tech Research Institute and former Senior Researcher at the Alaska Satellite Facility's SAR archives.

Methods

Sample sites were selected by stratified random sampling, using the 15 natural divisions of IL as the different strata with a Neyman allocation used to weight the number of samples per division. Lake Michigan was excluded due to logistical constraints. Survey sites were then assigned from the NWI using the reverse randomized quadrant-recursive raster (RRQRR) algorithm to create a spatially-balanced sampling pattern. The order in which each survey was conducted was randomized using the Mersenne Twister algorithm, but some exceptions were made to the sampling order due to logistical constraints such as private land access, boat availability, and ice.

Surveys are being conducted in three discrete seasons to coincide with the spring waterfowl migration, the summer marsh and wading bird nesting season and the fall shorebird migration (respectively): mid-February to mid-April, mid-April-June and August-September. Surveys will be conducted at each site once per season. During surveys, a team of 2-3 technicians will utilize GPS units to record the perimeter of all inundated areas that they encounter. Two teams will operate concurrently to maximize coverage: one from INHS and one from SIU. Geo-coded satellite images and field notes will be used with GPS tracks to create thematic maps of inundated and non-inundated areas within the surveyed areas. In 2015, ~90 sites of ~25 hectares each were surveyed in each of the three sampling seasons. We expect similar coverage in future years.

For objective 1, the thematic maps will be compared to NWI polygons using ArcGIS to determine what proportion of each NWI wetland type is inundated in each season and highlight any areas that have inundation, but are omitted in the NWI dataset. Determining these proportions specific to wetland type will allow us to scale the proportional inundation to the remainder of the dataset, providing an estimate of statewide wetland inundation, along with an uncertainty value.

For objective 2, two L-band SAR images taken on August 28th, 2015 were purchased. The images were taken at 6-m resolution and used the maximum number of polarizations (four). Downscaling and removal of polarizations will be conducted to simulate lower resolution/polarimetry options. Thematic maps from wetlands surveyed within one week of the imagery capture will be used to compare the accuracy for each imagery option. This will be weighed along with cost-per-unit-area of the coverage to determine the optimal imagery for further studies. Additional imagery will be purchased in May of 2017 to aid in the development of a classification model. A random forest classification model will be used along with C-band imagery, Landsat imagery, ancillary data, and a portion of the GIS inundation data to parse areas of inundation and non-inundation across the extent of the imagery. A separate subset of the GIS inundation data will be used to assess the accuracy of the classifier for each resolution level.

We were approved for a data grant from the Japanese Aerospace Exploration Agency (JAXA), providing us with up to 50 free images per year, for a total of three years, but they cannot be scheduled *a priori*. We have also been granted access to C-band SAR data through the European Space Agency. Our purchase imagery will be used to develop and evaluate the classification model. These additional free images will be used to increase the extent for estimates of inundation, providing substantial coverage of the state. Seasonal inundation extent and variability will be evaluated using geostatistical methods, allowing an estimation of the average proportion of available wetland area and variation across each of the seasons. The dissertation associated with the project is scheduled to be completed in 2018.

Expected results and significance

The inundation portion of the overall Federal project will support one dissertation, 3-4 peer-reviewed publications and several presentations at regional and national conferences. Presentations on preliminary analyses have already been given at multiple local and national conferences. Additional publications may be produced in synergy with the wetland quality study. Algorithms, models, satellite imagery, and survey data derived from the overall project will be made available to contributing agencies for further analysis and implementation.

Accurate estimates of wetland inundation will help refine estimates of available wetland habitat for WDA. Refined estimates should help correct for the potential overestimation of available habitat that arises when fluctuations in inundation are not considered. By evaluating multiple methods of estimating wetland inundation in Illinois, this project will provide a verified framework for future monitoring. Further, the methods and models developed in this study will potentially allow for wetland inundation to be estimated rapidly and at large spatial scales across the state.

Current status

Approximately 90 sites (~25 ha each) were sampled in 2015, and another 110 were sampled in 2016. Our recently completed spring 2017 samples covered 110 sites, and a similar number will be expected for repeat surveys in spring and autumn of this year. We are continuing to digitize the survey data into a GIS for analysis once field survey is completed. The first 50 free images have been downloaded from JAXA, spanning multiple seasons and years from 2014-2016. We will acquire additional images for that period and will also obtain images for 2017

with our remaining allotment of 100 images. The multi-season, multi-year dataset will allow analyses of patterns of wetland inundation in Illinois during that period.

Participating students

- John O'Connell – Doctoral student at SIU – dissertation on wetland inundation
- Abigail Blake-Bradshaw – Master's student at U of Illinois – thesis on wetland quality
- Micah Miller – Master's Zoology student at SIU – field assistant
- Harley Copple – Senior Zoology student at SIU – field/lab technician
- Shawn Caldwell – Senior Geography student at SIU – field/lab technician
- Travis Preston – Senior Geography student at SIU – field/lab assistant
- Hannah Judge – Junior undergraduate student at SIU – field and GIS assistant
- Alex Bell – Sophomore undergraduate student at SIU – field and GIS assistant
- Several recent graduates employed as field technicians (4 in 2015, 3 in 2016, 2 in 2017)

Literature citations

Batzer, D. P. and R. R. Sharitz 2006. Ecology of Fresh Water and Estuarine Wetlands. University of California Press. Berkeley, CA USA

Dahl, T. E., and G. J. Allord. 1996. History of Wetlands in the Conterminous United States. Judy D. Fretwell, John S. Williams, and Phillip J. Redman.(eds.), National Water Summary on Wetland Resources, USGS Water-Supply Paper 2425: 19–26.

Kudray, G. M., and M. R. Gale. 2000. Evaluation of National Wetland Inventory maps in a heavily forested region in the Upper Great Lakes. Wetlands 20: 581-587.

Lang, M. W.; Townsend, P. A.; Kasischke, E. S. 2008. Influence of incidence angle on detecting flooded forests using C-HH synthetic aperture radar data. Remote Sensing of Environment. 112:3898-3907

Mitsch, W. J., and J. G. Gosslink 2000. Wetlands. John Wiley& Sons, Inc. New York, NY. USA

Appendix A. Extent of Sentinel-1 C-band SAR imagery that is consistently available in the seasons and years of evaluation.

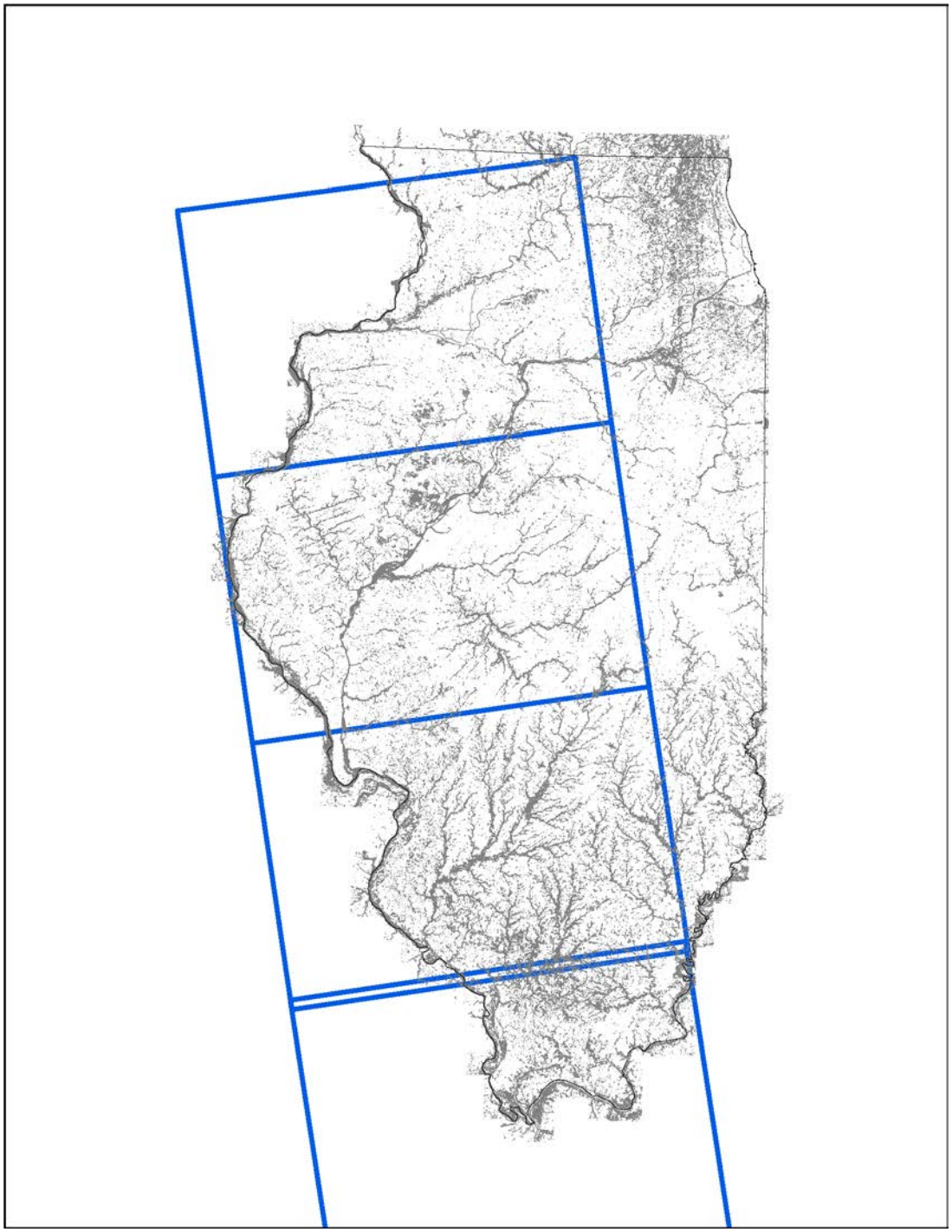

Appendix B. PALSAR-2 L-Band imagery currently downloaded for the focal period. Scenes were selected randomly from each of three strata of available images based on wetland density within the scene. Grey boxes signify scenes that were not selected because they did not overlap much of the state's wetlands or the Sentinel-1 imagery. Colored, hollow boxes represent those that were not randomly selected from the remaining sample. Filled boxes were selected. The maps include the NWI layer for Illinois.

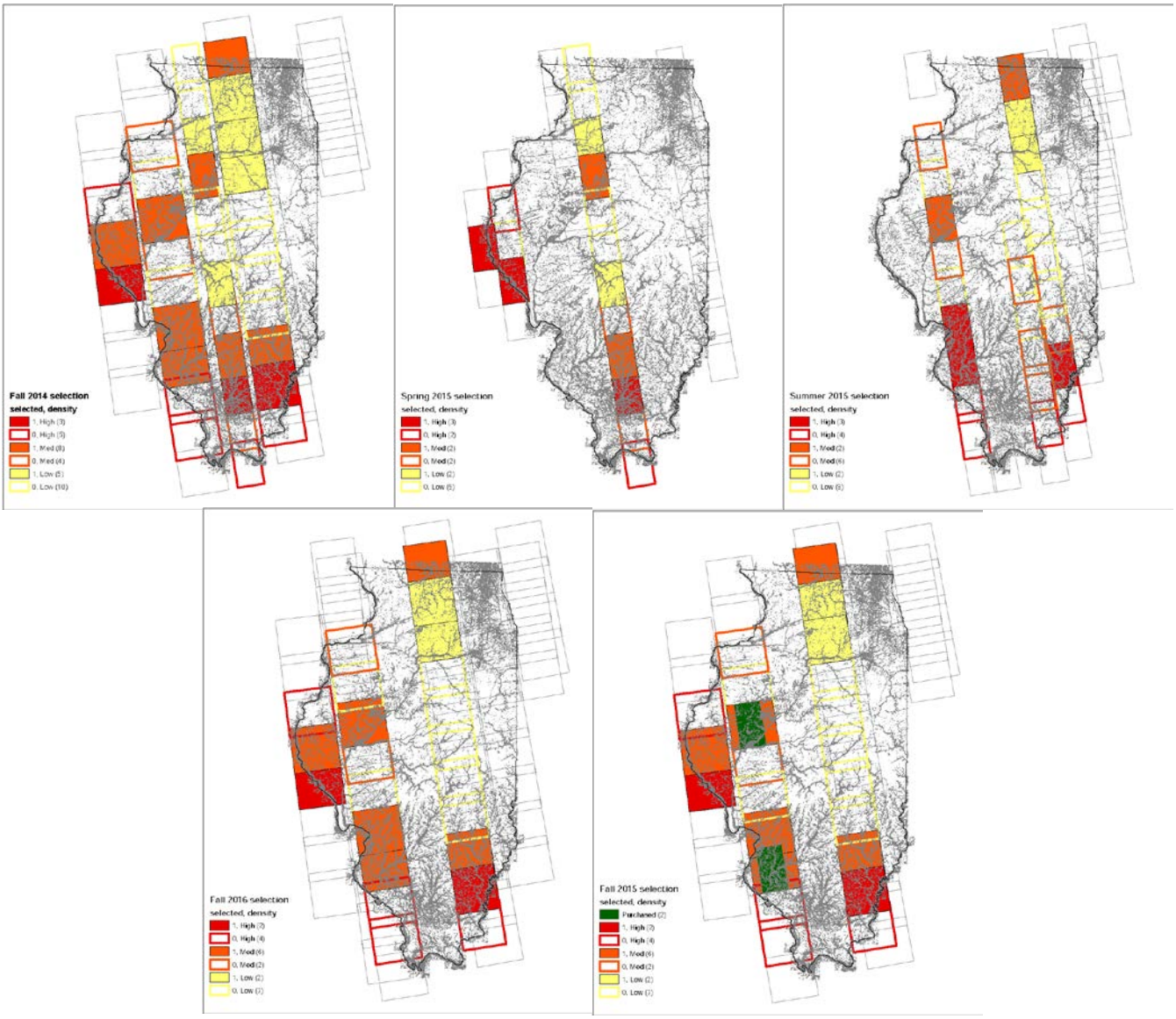

Under the Cover of Darkness: Nighttime water use by native, biofuel and agricultural crops of Illinois

Basic Information

Title:	Under the Cover of Darkness: Nighttime water use by native, biofuel and agricultural crops of Illinois
Project Number:	2016IL312B
Start Date:	3/1/2016
End Date:	2/28/2017
Funding Source:	104B
Congressional District:	IL-7
Research Category:	Climate and Hydrologic Processes
Focus Category:	Climatological Processes, Agriculture, Hydrology
Descriptors:	None
Principal Investigators:	Max Benjamin Berkelhammer, Benjamin Alsip

Publications

There are no publications.

Annual report for "Under Cover of Darkness: Nighttime water use by native, biofuel and agricultural crops of Illinois"

PI: M. Berkelhammer

Problem and Research Objectives:
In this proposal we have set out to understand the importance of nighttime transpiration for the water budget of typical Illinois landscapes. Nighttime water use by plants is typically neglected in water budget calculations and surprisingly little is known about the factors that control its magnitude and how it varies between plant types. The assumption has been that plants reduce their stomatal conductance to a universal minimum value at night and consequently transpiration is very small and does not vary. The limited observations available on nighttime water use by plants, suggest this assumption is false and that water use at night varies between species and responds to environmental changes such as temperature and humidity.

One of the motivations to study nighttime transpiration is that nocturnal temperatures are expected to increase faster than daytime temperatures over the next century. Thus, it becomes important to understand the sensitivity of plant water use to evolving nighttime climate. Furthermore, as landscapes are converted to agriculture or back to prairie or, alternatively, if managed landscapes are converted to different crops, it would be important to understand how these species differ in their nighttime water use. One reason to study this is because nighttime transpiration influences atmospheric humidity and therefore the rate that air cools at night. In addition, if plant stomata are remaining open during the night this influences atmospheric chemistry such as ozone concentrations.

The first goal of this project was to test a new method to continuously assess nighttime stomatal conductance at the ecosystem scale. This method involves measurements of the flux of a gas species called carbonyl sulfide (OCS), which is sensitive to plant stomata opening. The second goal of the project was to use this method to study the environmental factors such as temperature, wind speed, soil moisture and humidity that influence nighttime transpiration. The final goal was to assess how nighttime transpiration varies between different plant species or landscapes. To achieve these goals we made continuous measurements of OCS at the FermiLab AmeriFlux site in Batavia Illinois. We were able to document clear evidence for nighttime uptake of OCS, which is a strong indicator that stomata remained open at night. The best environmental predictor to explain day-to-day and seasonal variability in nighttime stomatal conductance is soil moisture. However, a lot of the variability we observed could not be explain by environmental factors and we suspect that circadian rhythms are important in controlling nighttime stomatal conductance. The importance of this process will be assessed in future studies.

Methodology:
Beginning in May 2016, a Los Gatos Inc. laser absorption spectrometer was installed in a small instrument shed at the FermiLab AmeriFlux site (Figures 2 and 3). The installation involved setting up an air conditioning system in the shed to sustain optimal temperature conditions in the shed otherwise, heat from the laser would cause the system to overheat (Figure 3). The analyzer was set up to make 1 Hz measurements of OCS, carbon monoxide (CO) and carbon dioxide (CO_2) at 4 heights above the surface on a small tower in the middle of a restored prairie site (0.5m, 1m, 3m and 4m) (Figures 5 and 6). Vertical gradients in the gas concentration can be used to make quantitative estimates of the flux rate of a gas. For example, if gas concentrations are lower near the surface, this means that the gas molecules are being consumed by a process at the surface (i.e. there is a *sink*). Alternatively, if gas concentrations are higher at the surface, this means the gas is being produced from the surface (i.e. a *source*). The difference in gas concentrations as function of height can be converted to a flux using "K-theory" which states that:

$$\text{Flux}=k*[(\text{Gas}_{\text{Height 1}}-\text{Gas}_{\text{Height 2}}/\text{Height 1-Height 2})]$$

where k is eddy diffusivity and varies as a function of wind and the surface friction. Negative flux values are associated with a surface sink. In the case of OCS, gas molecules are consumed when plants have open stomata so the flux is negative. Carbon monoxide also has a negative flux because it is consumed by soils. Carbon dioxide has both a sink and a source associated with photosynthesis and respiration, respectively.

Through the course of the summer, measurements were made continuously from the 4 heights on the tower. Overall, we made over 60 million gas concentration measurements that were converted to 30 minute flux estimates. There was only a single day during the entire campaign when the system failed due to a power outage on site. Weekly trips to the site were done to perform routine maintenance, transfer data and perform calibrations on the instrument. Supporting meteorological measurements for the site were provided from Department of Energy collaborators who have been making measurements at this site since 2010. We have reinstalled the system during April of 2017 (no longer supported by IWRC) to provide a second year of measurements.

Although our initial proposal intended to make measurements at a cropland, the energy demands for the AC made it impossible to run the system from a solar array. We did not anticipate the energy demands necessary to cool the laser would be as high as they were. While we would have liked to have complimentary measurements over an agricultural site, the dedicated continuous measurements we performed over the grassland provide the first and most comprehensive analysis of nighttime transpiration for a typical prairie.

Principal Findings:

(1) OCS concentrations over the course of the year show a strong seasonal cycle with concentrations highest during the early part of the growing season and lowest at the end of the growing season (Figure 7). This cycle, which has been observed elsewhere, reflects increased gross primary productivity and drawdown of OCS as the growing season proceeds. A comparison of the new data from FermiLab with that from the National Oceanic and Atmospheric Administration site in Park Falls, Wisconsin shows the pattern observed here is regional (Figure 8). The two sites, despite being 100s of km apart, show nearly identical values and comparable week-to-week variability.

(2) There is a strong diurnal cycle of OCS concentrations at the FermiLab site that represents a combination of plant uptake and changes in the height of the surface boundary layer. The gas concentrations are lowest at night and periodically drop below 30 parts per trillion (Figures 8). These are the lowest concentrations observed to date anywhere in the free atmosphere. The very low concentrations at night confirm our expectations that there is significant plant uptake of the gas at night corresponding to plant stomata remaining open.

(3) The midday uptake of carbonyl sulfide reaches a peak in May, when gross primary production is at its maximum. The flux declines through the growing season following declining soil moisture and vapor pressure deficit. The result confirms that carbonyl sulfide fluxes are a robust proxy for plant photosynthesis.

(4) Nighttime data confirm that carbonyl sulfide is being taken up by the ecosystem at night (Figures 9 and 10). There is a much smaller seasonal cycle in the nighttime fluxes than the daytime fluxes suggesting that nighttime stomatal conductance is not just a “memory” from the previous daytime values. The strongest controls on the nighttime fluxes appear to be soil moisture with a weaker effect from changes in nighttime relative humidity. These results confirm some expectations that stomatal conductance at night is controlled by similar processes as during the day. However, the fact that the nighttime fluxes stay relatively stable throughout the growing season also implies there are significant non-environmental controls on nighttime stomatal conductance. Further analysis will be conducted to explore other possible mechanisms to explain the observed variability.

(5) An opportunistic analysis was conducted through an undergraduate research project to explore the processes influencing the carbon monoxide concentrations at the site. This gas is measured by the laser as parts of its routine to measure carbonyl sulfide. The results show a clear difference in the diurnal cycle in carbon monoxide between weekends and weekdays. There is a clear peak in carbon monoxide between 7-8 am on weekdays, which corresponds with morning rush hour. This observation shows the strong effect that traffic has on ambient carbon monoxide concentrations (Figure 11).

Significance:

This work will contribute to a growing body of data on how carbonyl sulfide can be used as a proxy for plant photosynthesis and stomatal conductance (both night and day). We show very strong evidence that the carbonyl sulfide fluxes at this site track the seasonal and daily variability in photosynthesis and this is strongly controlled by soil moisture and relative humidity. We are undertaking one of the first comprehensive analyses of the nocturnal fluxes and this will be used in land surface models to place more realistic constraints on the processes controlling nighttime stomatal conductance.

We provide a first high resolution analysis of carbon monoxide in the Chicago suburbs and show the strong effect that weekday traffic has on carbon monoxide concentrations.

Students supported and education level (undergrad, MS, PhD, Post Doc):

(1) Ben Alsip: M.S. (summer support)

(2) Lucero Serrano: Undergraduate (semester hourly wage)

(3) Jen Bueno-Barraza: Undergraduate (semester hourly wage)

(4) Danielle Petkunas: Undergraduate (independent research project, no direct financial support)

(5) Omar Ortiz: Undergraduate (independent research project, no direct financial support)

Publications:

B. Alsip, M. Berkelhammer, R. Matamala, D. Cook and C. Whelan. *Carbonyl Sulfide Fluxes from a Tall Grass Prairie Ecosystem Through a Growing Season*. AGU Fall Meeting: Abstract #B53B-0527

M. Berkelhammer. *Carbonyl sulfide gradients over Midwestern US ecosystems.* The biosphere-atmosphere exchange and global budget of carbonyl sulfide. Sep. 5-9. Hyytiala, Finland.

B. Alsip*. Under the cover of darkness: Nighttime water uses by native, biofuel, and agricultural crops of Illinois*. Illinois Water Conference.

B. Alsip. *Carbonyl sulfide fluxes and concentrations over a restored prairie.* Masters Thesis, in prep (expected August 2017).

B. Alsip, M. Berkelhammer, R. Matamala, D. Cook. (in prep) *Regional drawdown of carbonyl sulfide during the Midwestern productivity maxima.*

Figure and Images:

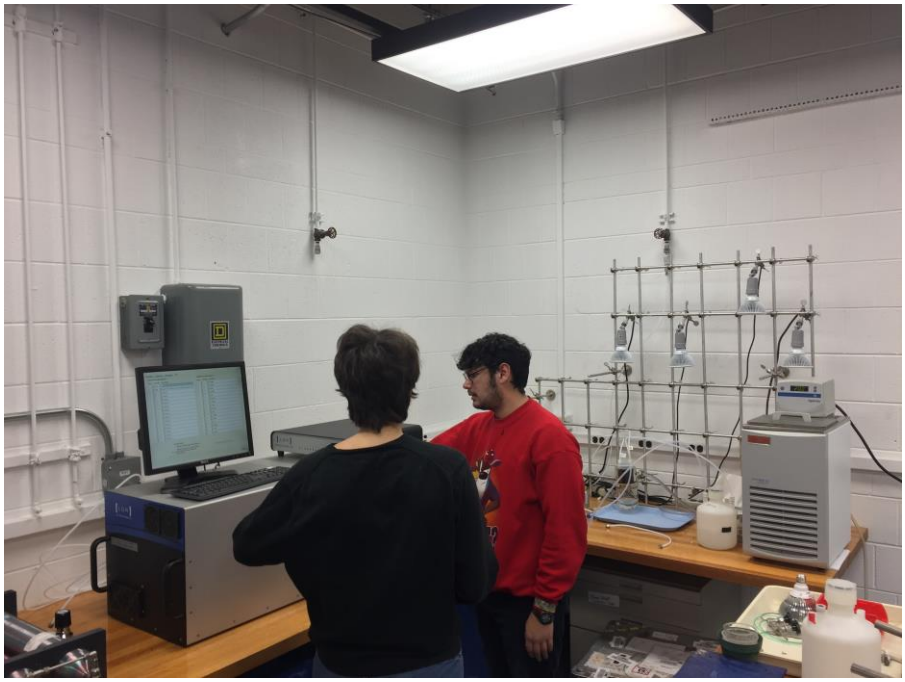

Figure 1: Omar Ortiz and Lucero Serrano calibrating the carbonyl sulfide laser.

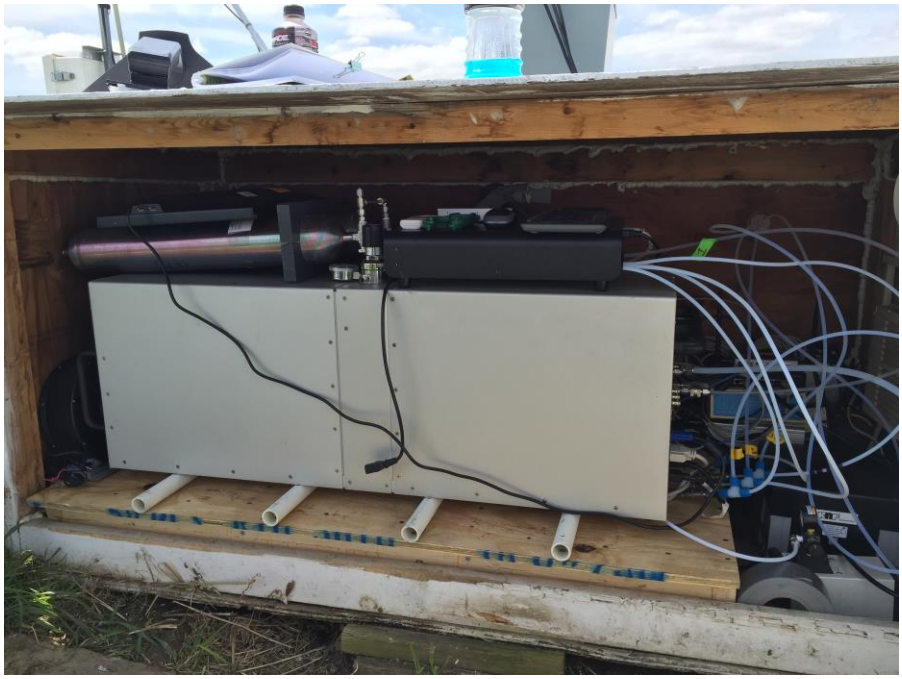

Figure 2: Carbonyl sulfide laser installed in the instrument shed at the FermiLab AmeriFlux site.

Figure 3: Instrument shed with air conditioning system installed to control shed temperatures.

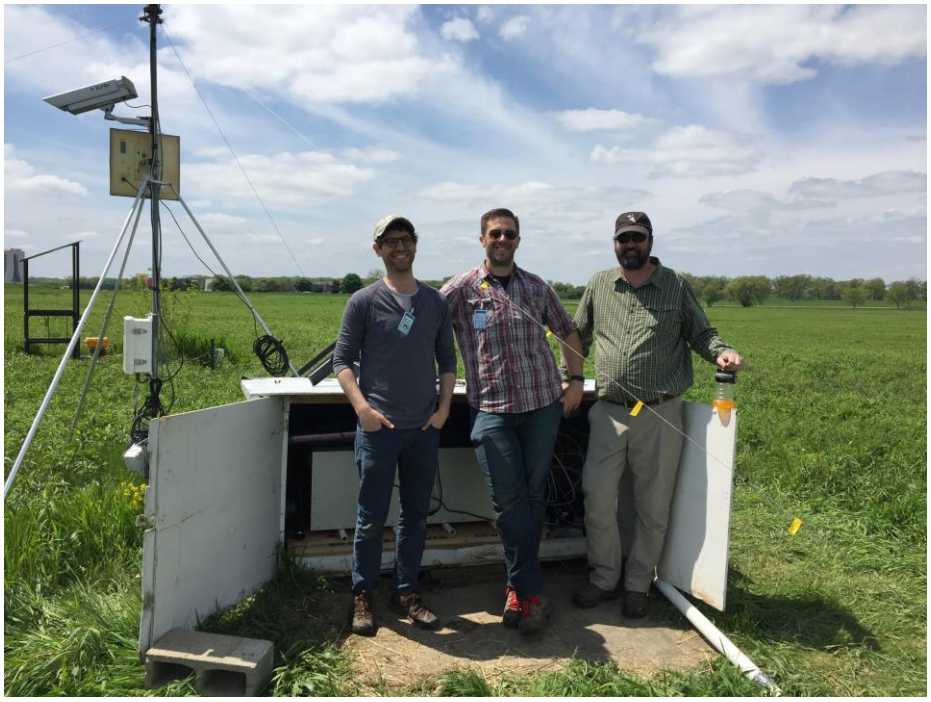

Figure 4: PI Berkelhammer, B. Alsip (Masters) and T. Larson (undergraduate) relaxing following the installation of the laser in May 2016.

Figure 5: Students installing gas inlet lines at the tower at FermiLab.

Figure 6: Sunset at the sampling site in May 2017.

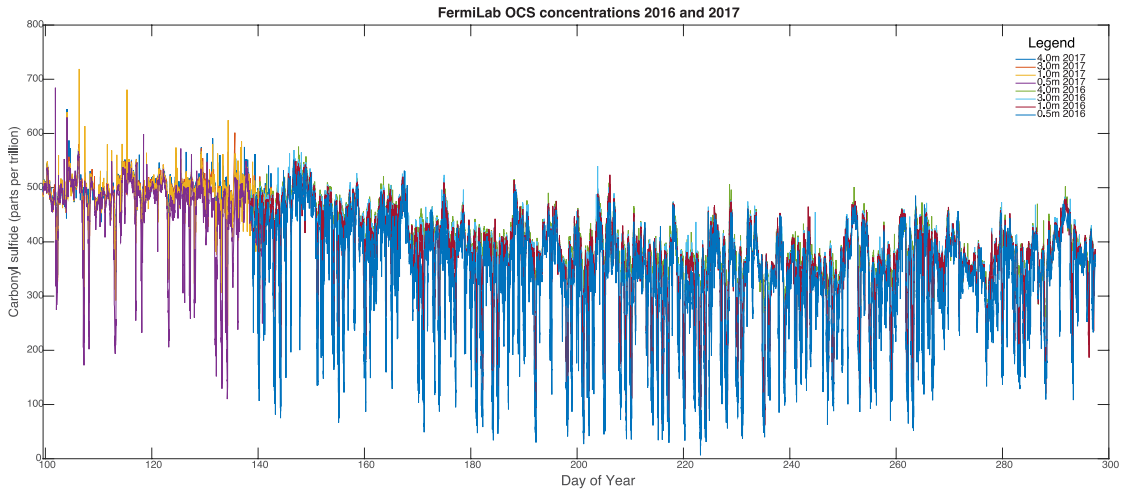

Figure 7: Carbonyl sulfide concentrations at the FermiLab site during 2016 and 2017 growing seasons. The multiple lines represent measurements being made at different heights above the surface.

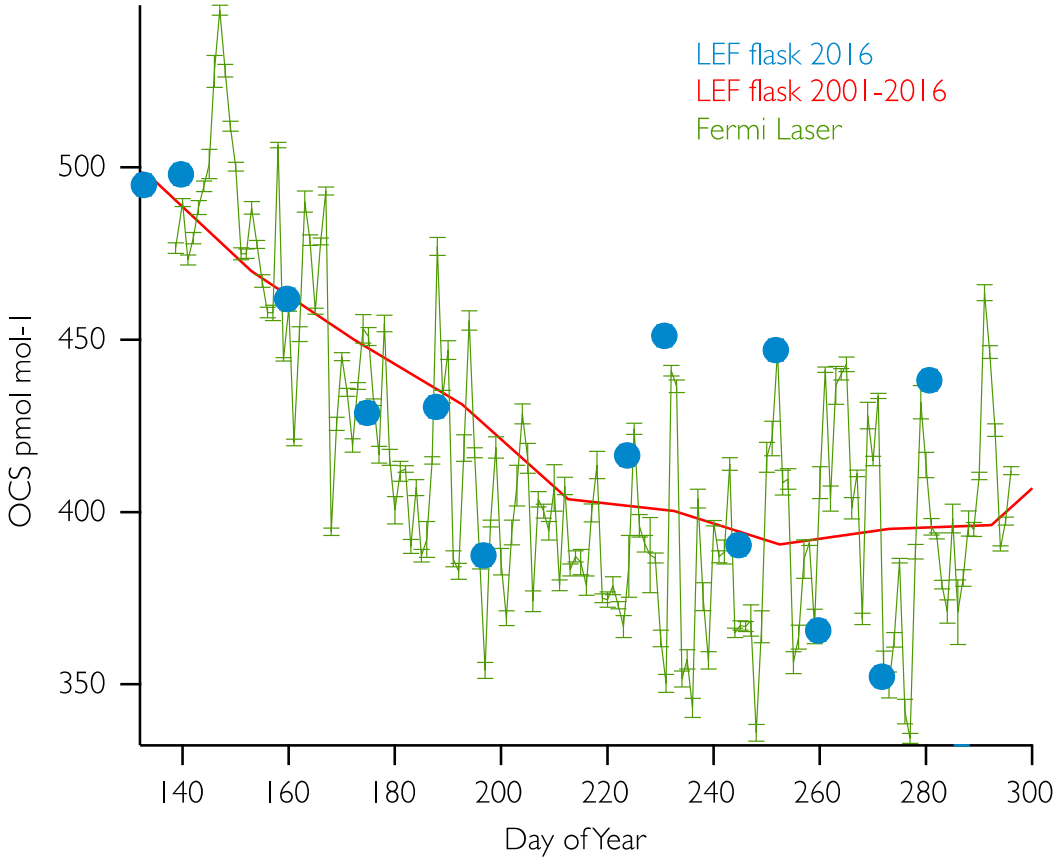

Figure 8: Daily variations in the carbonyl sulfide concentrations at FermiLab from this project (green). Weekly measurements of carbonyl sulfide from the NOAA site at Park Falls Wisconsin (blue dots).

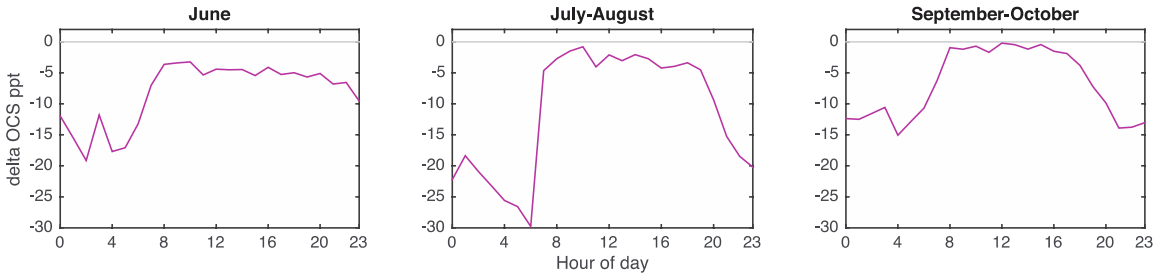

Figure 9: Diurnal cycle of the gradient between OCS at 4 m and at 1 m (i.e. delta OCS). Negative values indicate that the surface is acting as a sink. The different panels show the diurnal cycle in the gradient during different windows of the growing season.

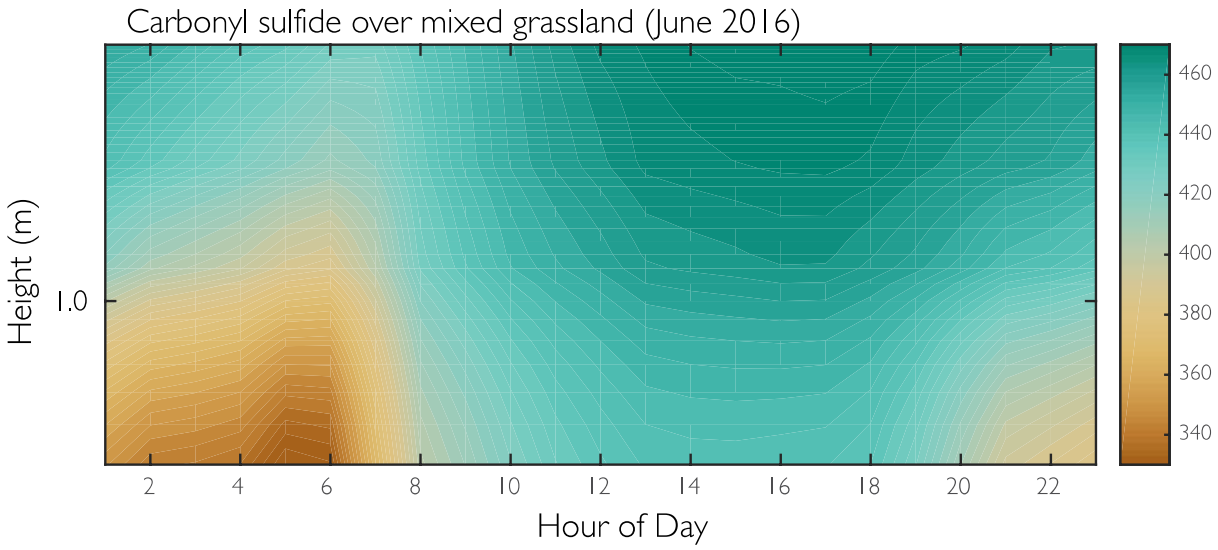

Figure 10: Interpolated surface showing carbonyl sulfide concentrations at different heights (y axis) and at different times of the day (x axis). The brown tones during the night near the surface, indicate strong uptake of carbonyl sulfide during the night. The unit of color bar is parts per trillion.

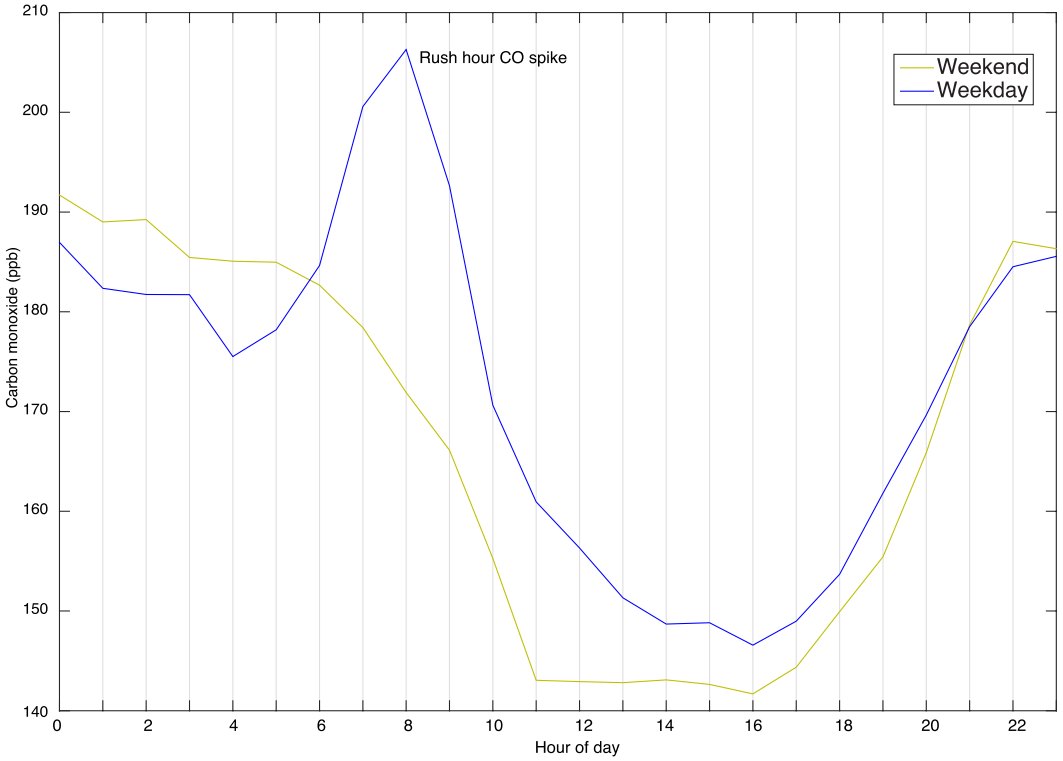

Figure 11: Diurnal cycle of carbon monoxide for the summer of 2016 at the Fermilab AmeriFlux site.

Spatial and temporal modeling of road salts in a watershed with mixed, urban and agricultural, land use

Basic Information

Title:	Spatial and temporal modeling of road salts in a watershed with mixed, urban and agricultural, land use
Project Number:	2016IL313B
Start Date:	3/1/2016
End Date:	2/28/2018
Funding Source:	104B
Congressional District:	IL-103
Research Category:	Water Quality
Focus Category:	Water Quality, Non Point Pollution, Models
Descriptors:	None
Principal Investigators:	Eric Wade Peterson

Publications

1. Ludwikowski, J., 2016, The transport and fate of chloride within the groundwater of a mixed urban and agricultural watershed, MS Dissertation, Geology,Illinois State University, Normal, IL, 56 p.
2. Chabela, L., 2017, Using 3-D modeling to describe the relationship between peak stage, storm duration, and bank storage and the implications along a meandering stream in central Illinois: Normal, IL, Illinois State University, 57 p.

Progress Report: Spatial and temporal modeling of road salts in a watershed with urban and agricultural land use

Principal Investigator: Eric W. Peterson

Academic Rank: Professor

University: Illinois State University

Email: ewpeter@ilstu.edu

Phone: 309-438-7865

Research Category: Water quality

Keywords: Deicers; Road Salts; Transport & Fate; Modeling

For Period: March 1, 2016 to February 28, 2017

Submitted: May 12, 2017

Table of Contents

Table of Tables

Table of Figures

I. Introduction

Chloride (Cl^-) is highly soluble and does not biodegrade, volatilize, precipitate, or absorb onto mineral surfaces [1, 2]. Thus, Cl^- is extremely mobile, easily transported within surface water or infiltrated into the subsurface. Natural sources of Cl^- include atmospheric deposition, rock weathering, and basin brines [3-5]. During winter months in northern latitudes, deicers, typically composed of a Cl^- salt, are applied to impervious surfaces, roads, walkways, and parking lots, to keep these areas clear of snow and ice [2, 6, 7]. In watersheds where deicers have been employed, natural Cl^- inputs contribute less than 1% of the Cl^- [1, 8], and inputs from agricultural and septic sewer systems only contribute an additional 1% to 3% to the total Cl^- load [8]. The remaining load is attributed to deicers, which serve as a nonpoint source of Cl^- [1, 4, 8]. Annual Cl^- use for road deicing in the US increased from 163,000 tons in 1940 to over 23 million tons in 2005 [9]; six states apply three quarters of the total mass of salt: New York, Ohio, Michigan, Illinois, Pennsylvania, and Wisconsin [10]. In the Chicago area, multiple entities apply over 270,000 tons of road salt, primarily as NaCl, to roads during an average winter [11, 12].

Between 35 to 55% of the applied salt will be transported away via overland flow, with Cl^- concentrations in excess of 1000 mg/L [13], to surface water bodies [14]. Following runoff, streams exhibit acute changes, 20- to 30-fold increases, in Cl^- concentrations [15-20]. The long-term use of deicers has had a chronic impact on streams [21, 22], with reported concentrations increasing 1.5 mg/L per year (Cl^-). Rural watersheds with low density of roadways have seen increases in Cl^- concentrations as a result of deicing applications in urban areas [23, 24]. Cl^- concentrations in the rural streams did not return to baseline levels in summer, even when no salt was being applied. Salt concentrations build up over many years and remain high in the soil and groundwater. Elevated concentrations within the groundwater contribute to elevated baseflow concentrations in streams during the spring and summer [3, 18, 25] and to chronic impacts on groundwater and surface water systems [1, 26, 27].

Between 45% to 65% of applied deicers accumulate in the shallow subsurface waters [2, 15, 28]. Infiltration of runoff from salted roads elevates Cl^- concentrations in roadside soils up to distances of 50 m [29-31], with Cl^- concentrations as high as 13,700 mg/L [20]. Cl^- accumulation in soils and in groundwater subsequently raises the baseflow Cl^- concentrations in surface water bodies during the summer and leads to increases in the baseline salinity of surface waters [32, 33]. In select cases, Cl^- concentrations have increased by 243% over a 47-year period [17], and in other cases, Cl^- concentrations are up to 100 times greater than non-impacted streams [23]. Although acute concentration spikes associated with winter runoff can exceed 1000 mg/L [34], sustained, chronic, concentrations have been rising in streams. For example, the baseflow Cl^- concentration in Highland Creek (Toronto) has increased from 150 mg/L in 1972 to about 250 mg/L in 1995 [21]. Once in ground water, Cl^- can persist for many years [35], and even if deicing applications stopped, it would be decades before the Cl^- concentrations returned to pre-1960 levels in shallow ground water [4, 20].

Although Cl^- has typically been viewed as a benign ion in the environment, exposure to acute (> 1000 mg/L) and chronic (>210 mg/L) Cl^- concentrations can have deleterious effects on aquatic flora [2, 29, 36-49] and fauna [31, 50-52]. Subsequently, the USEPA [53] established a criteria maximum concentration (acute toxicity) of 860 mg/l and a criterion continuous concentration (chronic toxicity) of 230 mg/l for chloride for freshwater aquatic life. As a result of delayed (lagged) Cl^- concentrations in streams, sensitive life stages can be exposed to concentrations long after the winter period of application has occurred [54].

II. Research Objectives

Aquifer salt loading can be quite variable due to diversity of road types, application rates, land use, soil characteristics, and subsurface geology. Cl^- concentrations in the recharging waters can also change with time due to variation in precipitation and application rates. Scarcity of accurate data (i.e. salt application rates) and complexities associated with characterizing the urban hydrologic system lead to difficulties in linking spatial variability with potential impact of this nonpoint source contaminant.

Through this project, we sought to develop models to understand the transport and fate of Cl^- in a watershed. Overall, this study examined spatial and temporal variations in Cl^- concentrations, addressing the following questions:

1. Does road salt applications elevate Cl^- concentrations in a stream throughout the year?
2. Under what conditions will a watershed reach equilibrium between Cl^- inputs and outputs?
3. What is the time interval required for a system to return to background levels of Cl^- once inputs are decreased or ceased?

III. Site Description

The study focuses on Little Kickapoo Creek (LKC), a low gradient, low order, perennial stream that occupies a glacial outwash valley and its watershed (LKCW)(Figure 1). LKC headwaters are in southeast Bloomington, Illinois; Bloomington's total population is 78,902 and is growing at an annual rate of 3.0% [55]. Upon leaving the urbanized area of Bloomington, LKC flows through a low density suburban setting and then into an agricultural area. The LKC watershed covers a total area of approximately 56 km^2, from which 1.7 km^2 is road surface. The land use is 27% urban, 69% agricultural, and 4% forested/ wetland/ surface water areas; classifying the watershed as mixed urban and agricultural. The average annual precipitation for the area (1971-2000) is 95 cm of rain and 56 cm of snowfall [56]. Previous studies have examined and reported the geology, hydrology, and hydrogeology of the area [57-63]. Background stream Cl^- concentrations and groundwater concentrations tend to be less than 10 mg/L

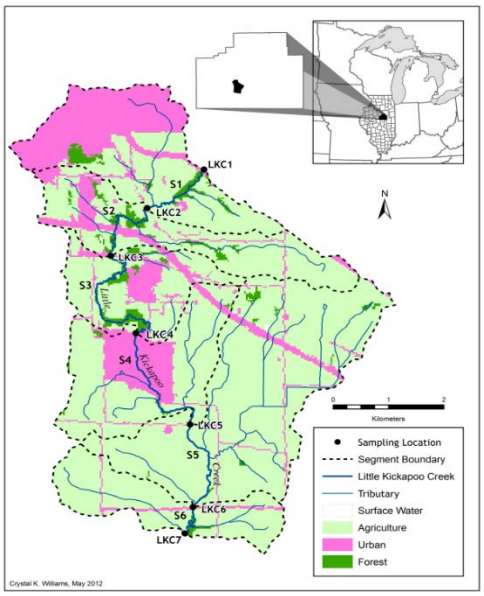

Figure 1: Little Kickapoo Creek watershed showing the proposed sampling sites and the land use for the area.

IV. Methodology

a. Stream Cl- concentrations

Surface water samples were collected every two weeks from seven locations (LKC1-7) along LKC (Figure 1) and analyzed for major anions (Cl^-, SO_4^{2-}, and NO_3-N) with a Dionex DX-120 Ion Chromatograph housed within the ISU Department of Geography-Geology. Quality assurance (QA) and quality control (QC) were be maintained during analysis of each sampling event by running blank, duplicate, and replicate samples. In-situ measurements of dissolved oxygen, specific conductance, and temperature were recorded using a YSI-85. Stream discharge measurements at each location were calculated using the velocity-area method [64], where velocity was measured using an electromagnetic flowmeter. Chloride loads were calculated using the discharge and the Cl^- concentration data. Sampling was conducted from August 2015 to February 2017.

b. Numerical Modeling-Watershed

Groundwater flow was simulated using MODFLOW [65], while MT3D [66] was used to simulate the transport of Cl^- within the system. The moel domain of the LKCW was delineated utilizing hydrography data from the National Hydrography Dataset [67]. The domain of the model was limited to the surface water drainage basin for LKC, assuming that the surface water divide serves as a groundwater divide for the shallow groundwater system. At the watershed perimeter, no-flow conditions were assigned to represent the groundwater divided. Along the bottom of the domain, the contact between the glacial materials and Pennsylvanian shale served as a no-flow boundary, restricting flow to two-dimensions. Consistent with previous studies in the area (e.g. [30, 57, 59, 62, 68]) uniform recharge of 3.0×10^{-9} m/s, equivalent to 10% of the average annual precipitation, was applied across the surface of the model domain (Table 1). LKC and the tributaries were treated as a constant head boundary with constant solute conditions. Groundwater flow was assumed to be steady-state, but the solute transport (Cl^-) was transient

due to the seasonal depositional rates. Given the geology of the system and the interest in horizontal transport towards the stream, a one-layer model accounting for two-dimensional (2-D) flow through the glacial sediments was developed. The area was discretized into model cells with a dimension of 100 m by 100 m, generating a finite-difference grid with 164 rows, 72 columns, and a total of 7,136 active cells.

Cells were assigned hydraulic conductivities to represent the respective units, either till or outwash. Individually, the till and outwash are represented as homogeneous and isotropic. As a whole, the system is heterogeneous with K values differing between the units. Storage parameters were derived from field work or from reported values in previous studies (Table 1). Aquifer test data from wells located in the modeled area were used to measure storage values for the tills and outwash (Table 1).

Table 1: Values used for model parameters.

Parameter	Value	Source
K – outwash	1.0×10^{-4} m/s	Ackerman, Peterson [68]
K – till	1.0×10^{-8} m/s	Hensel and Miller, 1991
Porosity – outwash	0.25	Ackerman, Peterson [68]
Porosity – till	0.35	Ackerman, Peterson [68]
S_y – outwash	0.021	Field test
S_y – till	0.01	Field test
S_s – outwash	0.0007	Field test
S_s – till	0.00056	Field test
Recharge rate	3.0×10^{-9} m/s	[30, 62, 68]
Cl^- Dispersivity longitude	1.78 m	[69]
Cl^- Dispersivity latitude	1.64 m	[69]
Cl^- concentration – Winter	$\geq$ 1,000 mg/L	Lax and Peterson [30]
Cl^- concentration – Winter	10 mg/L	Kelly [70]

Solute transport was simulated under transient conditions with two stress periods; one period represents winter, a time of Cl^- application. The second period represents no Cl^- application, spring, summer, and fall. Combined, the two periods equal a year, with the winter stress period lasting 84 days and the summer through fall spanning 281 days. For each stress period, the time step is one (1) day. The 84 day winter stress period is based upon the results of an infiltration model [30]. The National Land Cover Database assisted in the classification of cells in the model by revealing urbanized, road, agricultural and forested land use locations. Urbanized and road cells were treated as sources of Cl^-, with an increased Cl^- value that reflects elevated winter concentrations (Table 1); while agricultural and forested areas had constant Cl^- concentrations, 10 mg/L, through the whole simulation. Cells identified as roadways and urban areas from the National Transportation Dataset [71] were designated as sources of Cl^- due to road salt. To winter simulate conditions similar to those observed in Illinois [30, 72](Table 2), the different scenarios utilized different Cl^- levels, all above 1000 mg/L, for the urbanized cells. The 1,000 mg/L is lower than the measured concentrations within infiltration near a road [30] but given the size of the model cells, was determined to be more representative of the input concentration. Non-urban cells were assigned an initial concentration of 10 mg/L simulating background conditions [70], and the recharge maintained a constant 10 mg/L concentration over the duration of the simulation. To accurately model Cl^- movement a dispersivity coefficient of 1.78 m for longitude and 1.64 m for latitude was employed [69]. Porosity values of the till and outwash units were 0.25 and 0.35 respectively. Since Cl^- is conservative, no retardation factors or reactions were simulated.

Seven scenarios were developed to assess the transport and fate of Cl^- in the watershed. Scenarios 1 and 2 simulated 10 cycles (or 10 years) of winter and summer. Beginning in cycle 11, year 11, the simulation of road salt application ceases, and the background Cl^- levels are applied consistently to all cells during all stress periods. Scenario 1 used Cl^- application rates of 1,000 mg/L whereas Scenario 2 employed 10,000 mg/L. At the end of each decade, the maximum Cl^- concentration and net mass values were recorded. Utilizing a basic mass balance equation the amount of Cl^- entering and leaving the system was calculated. Scenarios 1 and 2, referred to as the "**Flush Scenarios**", offer insight into how the watershed flushes out Cl^- after 50 years of no application and to determine storage relative to the different application rates.

Table 2: Build-up scenarios: Assigned application rate.

Scenario	Winter Application Rate (mg/L)
3	1,000
4	2,500
5	5,000
6	7,500
7	10,000

Scenarios 3 - 7 simulated a constant, but different, deposition rate across a 60-year span (Table 2). As the application of Cl^- occurs over the entire 60 years, Scenarios 3 – 7 are referred to as the "**Build-Up Scenarios**". The scenarios provided insight to the relationship between Cl^- application rate and 1) the accumulation of Cl^- mass in the system and 2) the residence time of Cl^- in the system. For each year, the residence time was calculated using the Equation (1), presented by Dingman [73]:

$$Tr = \frac{Total\ Mass\ solute}{Mass\ Out\ solute} \quad \text{Equation 1}$$

c. GIS - Regression Modeling

A GIS model was developed in ArcGIS 10.3 to model concentrations along the stream. The model examined the kilometers of roads in each sub-watershed and land use from the United States Geological Survey. Both the developed high intensity and developed medium intensity were added together to provide the area of urbanization in each sub basin. The developed high intensity and developed medium intensity were chosen because 50-100% of the area represent impervious surfaces, which is where road salts are likely to be applied.

The spatial data and field data were incorporated into a GIS database. The data included Cl^- concentration at a given location, Cl^- concentration at the most upstream site (LKC1), water day, temperature, sub-watershed drainage area, kilometers of road in sub-watershed, and land cover area per sub basin. A multiple linear regression model was developed to simulate concentrations along LKC and to determine the parameters that were controls on the Cl^- concentrations. The multiple linear regression was completed using SPSS. SPSS calculated a coefficient for each variable and p value to show that variable's significance to the dataset. The coefficients will be multiplied by each respective variable and summed together to predict the chloride concentration at downstream locations. The regression was conducted multiple times, adding and subtracting variables, until each variable was statistically significant ($p<0.05$).

V. Principle Findings

a. Stream Cl- concentrations

Chloride concentrations ranged from 37.4 mg/L to 460.4 mg/L in the waters of LKC, with the waters possessing similar concentrations across the seven locations (Table 3; Figure 2). The Cl^- concentrations are typically below the 230 mg/L Cl^- identified as the chronic toxicity threshold established by the USEPA [53]. Chloride load ranged from 1436 Kg/s to 321578 Kg/s (Table 3). Spatially, no differences in concentrations were observed among the locations.

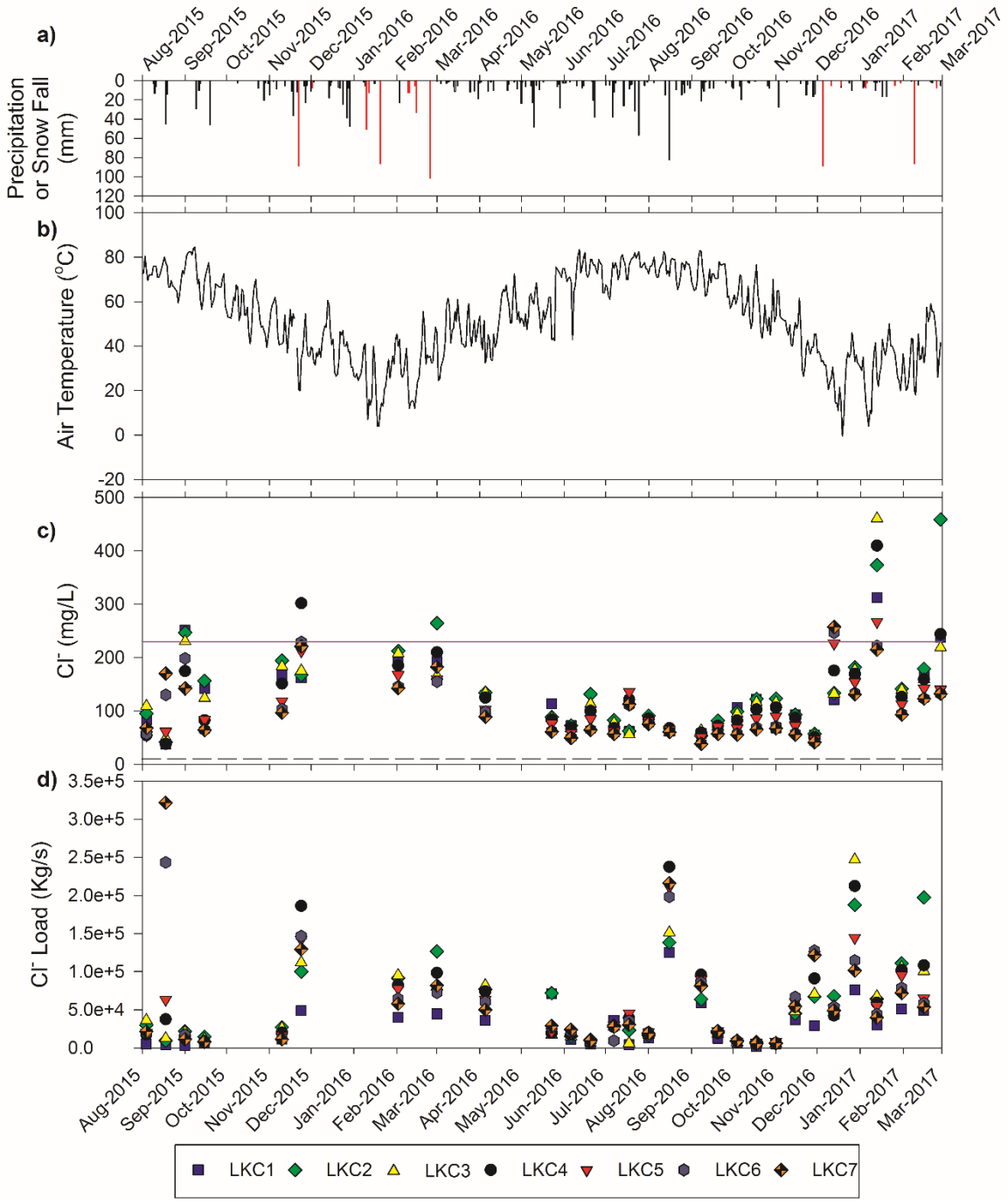

Figure 2: a) Precipitation (black) and snowfall (red) during the period of sampling. b) Air temperature during the period of sampling. c) Chloride concentrations for the waters at the seven locations. Purple line represents the 230 mg/L threshold and the black dashed lines is in the background concentrations of 10 mg/L. d) chloride load for the locations.

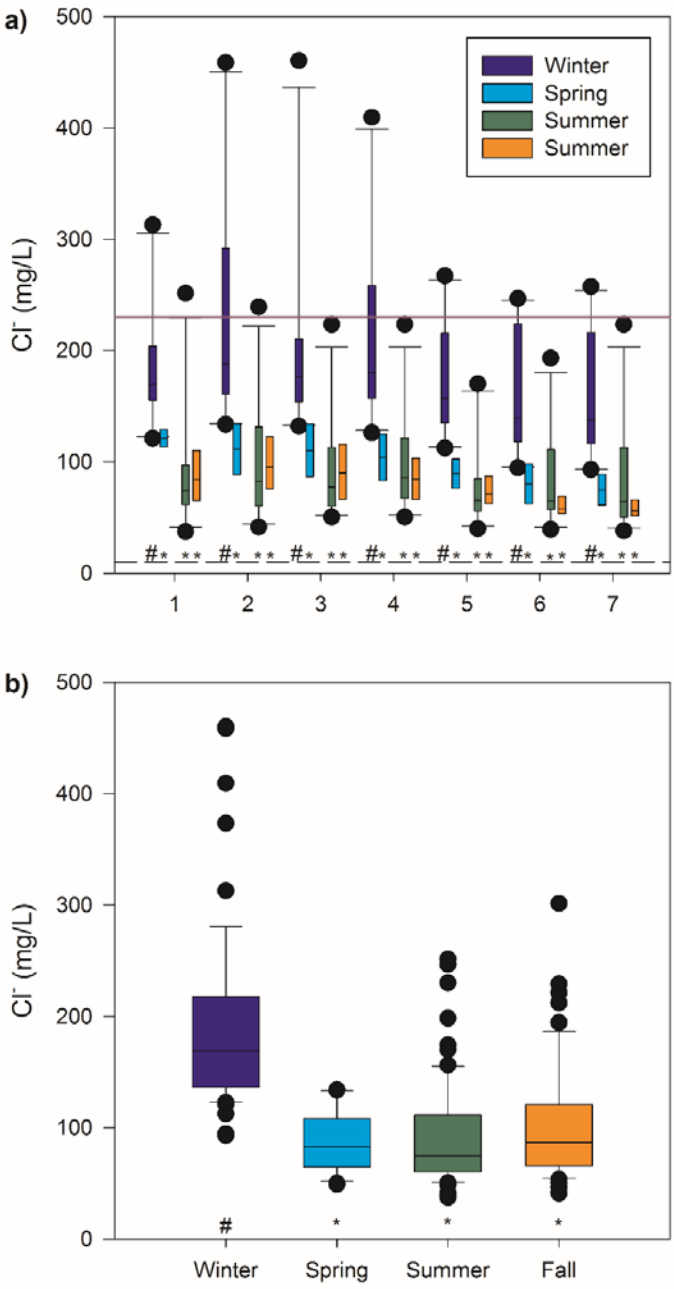

Figure 3: Box and whisker plots of a) Mean Cl^- concentrations for each season at the individual locations. Purple line represents the 230 mg/L threshold and the black dashed lines is in the background concentrations of 10 mg/L. b) Mean seasonal concentrations for the locations pooled together. Symbols, # and *, below box and whiskers signify values that are statistically similar.

Chloride concentrations varied temporally, with higher concentrations occurring consistently in the winter. No difference in concentrations among the other seasons was observed [$F(3,6)=81.9$, $p<0.001$] (Figure 2 and Figure 3). The highest Cl^- concentrations follow snow events (Figure 2c). While the highest Cl^- concentrations were observed in the winter, the largest Cl^- loads were measured in August (Figure 2d). The high loads in August correspond to precipitation events when discharge was high. Both Cl^- concentration ($r = -0.585$, $n = 203$, $p = 0.001$) and Cl^- load ($r = -0.317$, $n = 203$, $p = 0.001$) are negatively correlated to water temperature (Figure 4), which serves as a proxy for time of year.

b. Numerical Modeling-Watershed

i. Flush Scenario Results

The flush scenarios simulate road salt application of 1,000 or 10,000 mg/L for 10 winter seasons. After year 10, the application of Cl^- is discontinued, and the model simulates 50 additional years with no additional Cl^- inputs. In both scenarios, Cl^- accumulates within and near roadways and urbanized areas (Figure 5). Some areas, not near the roads or urbanization, show deposition of Cl^-, with concentrations remaining at the background values. After the Cl^- application is ceased, the Cl^- dissipates from roadways and urbanized areas into the surrounding aquifer and moves toward LKC. At the end of the 60-year period, Cl^- concentrations remain highest along roadways, especially those within areas comprised of till material. Till dominated areas have increased Cl^- concentrations and continue to store Cl^- despite 50 years of no

application. The 10,000 mg/L rate has more Cl^- in storage than the 1,000 mg/L rate due to Cl^- loading in the low conductivity tills.

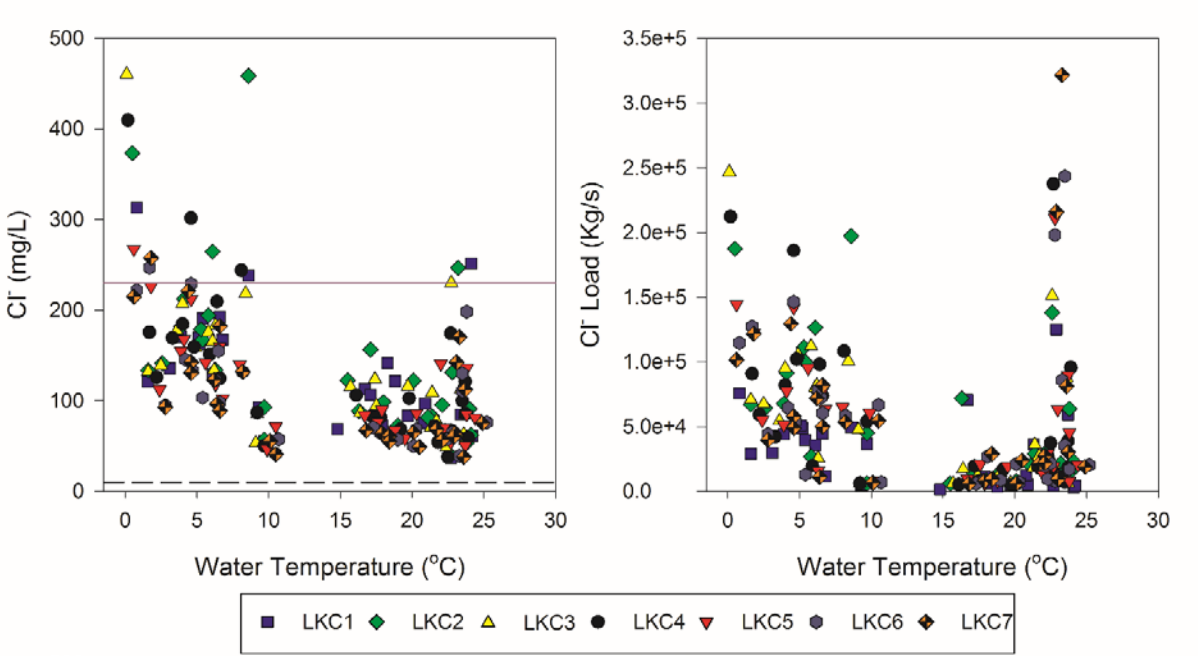

Figure 4: Relationships between water temperature and a) Cl^- concentrations and b) Cl^- load. Purple line represents the 230 mg/L threshold and the black dashed lines is in the background concentrations of 10 mg/L.

Table 3: Cl^- concentration and Cl^- load data for the sampling locations.

Sample	Cl^- (mg/L)			Cl^- Load (Kg/s)		
Location	Mean ± StdDev	Minimum	Maximum	Mean ± StdDev	Minimum	Maximum
LKC1	125.8 ± 66.1	37.4	312.9	29970 ± 28829	1437	125122
LKC2	144.8 ± 95.3	41.6	458.6	57041 ± 53750	5964	197303
LKC3	131.3 ± 82.0	48.9	460.3	53116 ± 55199	5912	246859
LKC4	129.5 ± 82.5	37.9	409.6	59030 ± 62906	4784	237348
LKC5	110.0 ± 56.4	46.8	267.2	54260 ± 50679	6272	211077
LKC6	103.7 ± 59.1	39.4	246.8	56711 ± 59774	5980	243400
LKC7	102.9 ± 59.1	38.1	257.5	57592 ± 69405	5614	321579

For each application rate, the peak Cl^- concentration in the system increases, reaching a maximum concentration at year 10 (Figure 6). After year 10, the concentrations decrease following power laws (Figure 6). For the 1,000 mg/P application rate, the peak Cl^- concentrations, 85 mg/L, represents 8.5% of the application rate. When the application rate is 10,000 mg/L, the peak Cl^- concentration at year 10 is 767 mg/L, 7.7% of the application rate (Figure 6). Although the decrease in Cl^- concentration follows a power law, neither system has returned to the background concentration of 10 mg/L by the end of the simulation. Following 50 years of no Cl^- application, the maximum Cl^- concentration was 166 and 25 mg/L for 10,000 and 1,000 mg/L application rates, respectively. Using the appropriate power laws, the 1,000 mg/L and the 10,000 mg/L application rates would return to background concentrations after 237 years and 1658 years, respectively. After the 10 years of Cl^- application, the application of 10,000 mg/L resulted in the storage of 127,000 Kg of Cl^-. The lower application rate produced 11,800 Kg of Cl^- in storage. In accord with the reduction in Cl^- concentration in the waters of the system during the 50 years of no application, the mass of Cl^- in the system decreased. Following exponential decay trends, the mass drops by a little more than half by the simulation end to

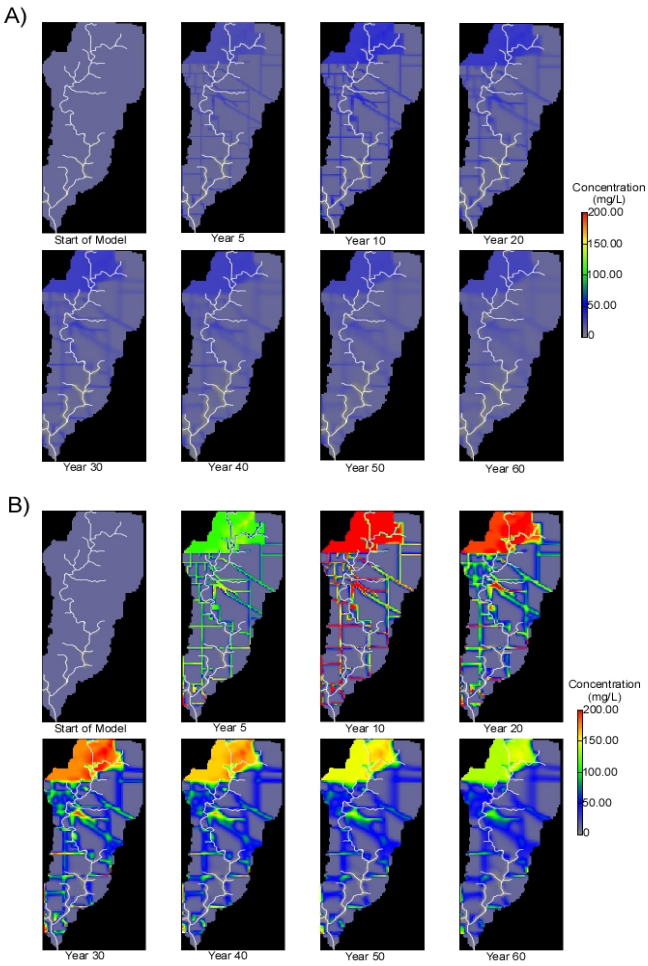

Figure 5: Chloride concentration color flood map of model scenario 1 at 1,000 mg/L (A) and 10,000 mg/L (B) application rates. Both panels show models in which road salt was applied for 10 winter seasons; shut off at end of year 10 and then ran at background levels for 50 years after.

6,200 Kg for the 1,000 mg/L application rate and to 73,500 Kg for the 10,000 mg/L application rate (Figure 7).

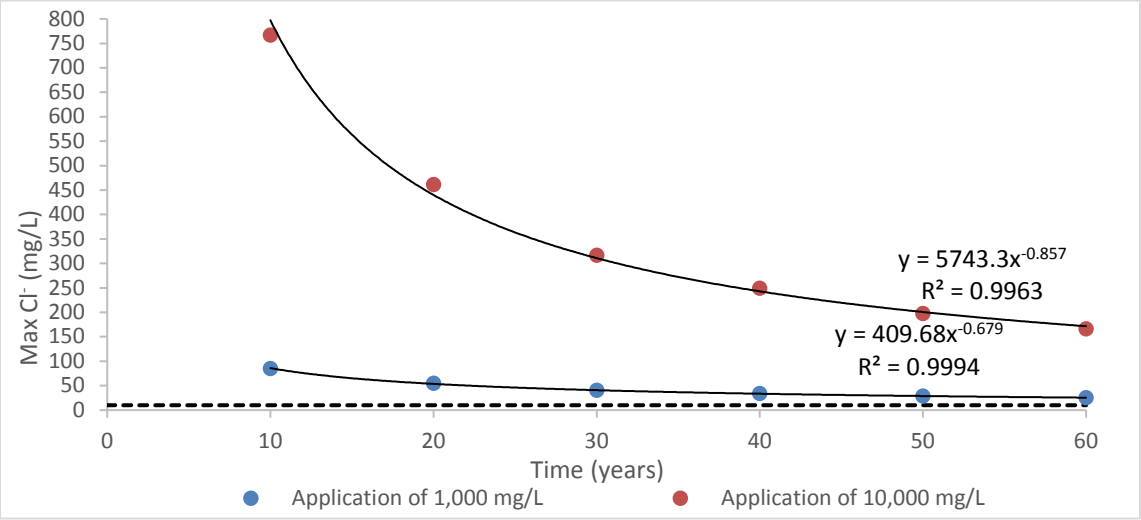

Figure 6: Model scenario 1 results, wherein road salt was applied for 10 winter seasons and shut off at end of year 10. Reported is the maximum Cl^- concentration (mg/L) at the end of each decade and the background levels (black).

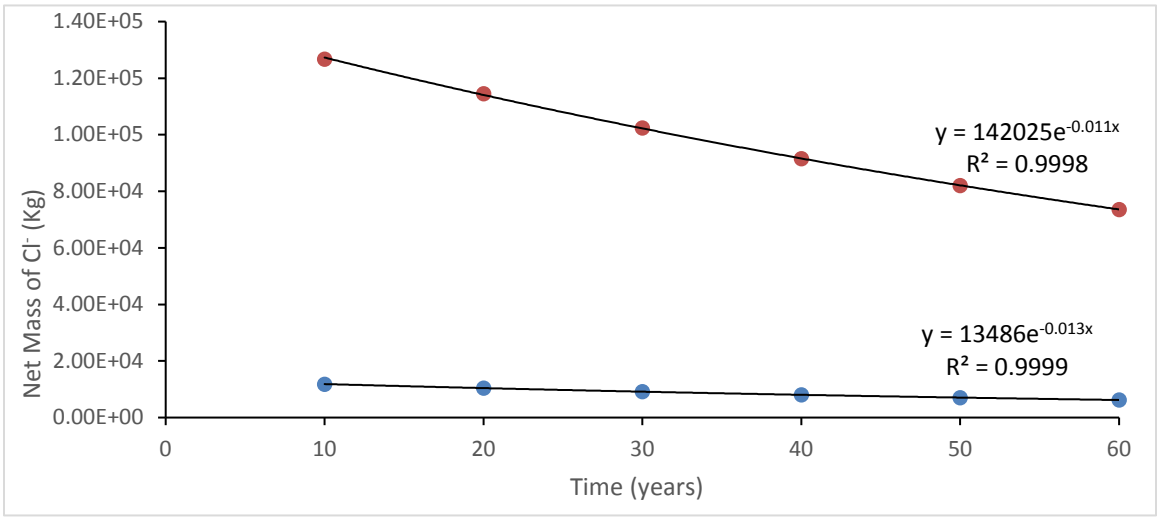

Figure 7: Model scenario 1 results, wherein road salt was applied for 10 winter seasons and shut off at end of year 10. Reported is the net mass of Cl^- (Kg/L) at the end of each decade.

Flush models were assigned specific application rates that were applied for 10 winter seasons then shut off. The estimated flush time is relative to application rate with the application rate of 1,000 mg/L having 47% of its mass flush away while the 10,000 mg/L saw 42% flushed away (Figure 6). The 10,000 mg/L rate took 40 years to return to the EPA chronic toxicity level of 230 mg/L (Figure 6). Bester et al. [74] simulated the transport of a Cl^- plume in an industrial/urban aquifer setting; model simulations indicated Cl^- would flush out of the aquifer after four decades of no application. For both application rates, the simulations show that after 15 years the maximum Cl^- concentrations are half of the peak concentrations, similar to [74] (Figure 6).

ii. Build-up Scenario Results

Build-up scenarios simulate a constant road salt application for 60 winter seasons, with each scenario having a specific application rate (Table 2). Similar to the flush scenarios, mass balance data and the maximum Cl^- concentrations at five-year intervals were recorded. For each individual application rate, the maximum Cl^- level increases every year (Figure 8). Application rates of 7,500 mg/L and 10,000 mg/L show no signs of reaching steady state, but the lower rates appear to be nearing a plateau by the end of the 60-year simulation (Figure 8). The point at which the watershed reaches steady state is relative to the application rate; severe application rates such as 10,000 mg/L show the watershed as continually storing Cl^-. As the application rate increases so do the Cl^- concentrations within the system, a linear relationship between the two is implied (Figure 9). Even after a 60-year period, the maximum Cl^- levels are only about 19% of input for all rates.

The net mass of Cl^- was also computed for build-up models at the end of each five-year period. From the start to year 60, each simulation shows Cl^- mass accumulating annually, with the 1,000 mg/L and 2,500 mg/L rates stabilizing towards the end of the 60 years (Figure 10). At the end of year 60, the net mass is 596,000 Kg for the 10,000 mg/L application rate and 58,000 Kg for the 1,000 mg/L (Figure 10). As expected, increasing road salt application also increases the net mass of Cl^- in the system.

Color flood maps of model scenario 2 were constructed to demonstrate the distribution of Cl^- across the watershed. Both map's roadways and urbanized areas have the highest concentration of Cl^- and the lowest concentrations are found in LKC (Figure 12). Unlike the first set of color flood maps (Figure 5), the spreading and storing of higher concentration water s from the source areas in to the adjacent sediments is illustrated (Figure 12). As LKC represents a point of groundwater discharge, Cl^- transport is directed towards LKC. For both application rates, the agricultural lands have the lowest concentrations due to their distance from urban areas and roadways (Figure 12). With both application rates, the Cl^-

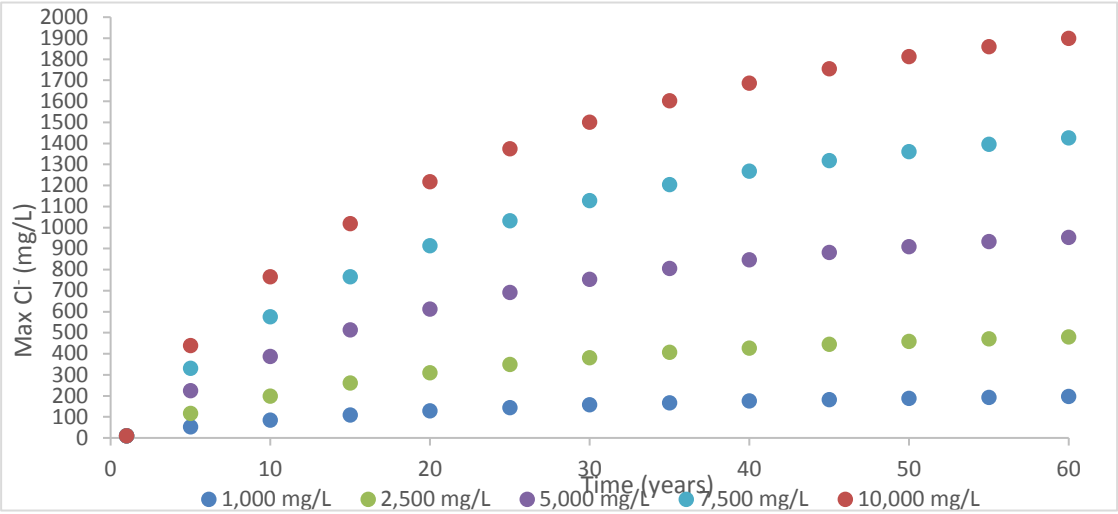

Figure 8: Build-up model results, wherein road salt was applied for 60 winter seasons. Reported are the maximum Cl^- concentrations (mg/L) at the end of each five-year period.

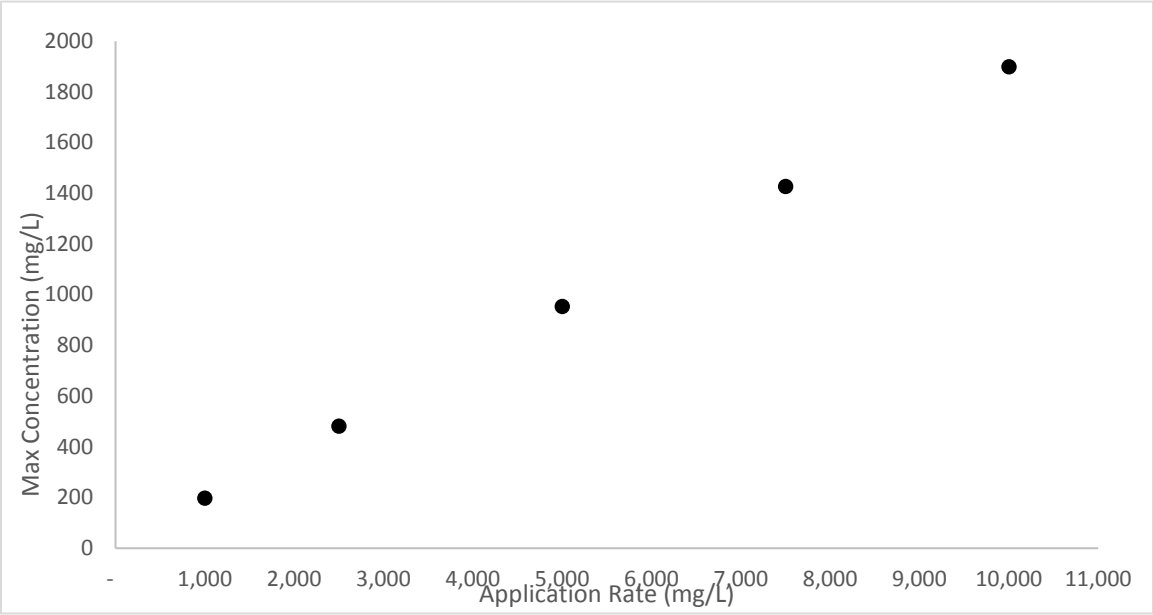

Figure 9: Relationship between the application rate and the maximum Cl^- concentration at the end of the 60-year simulation.

concentration increases over time in the agricultural areas (Figure 12). The 10,000 mg/L map uses a different color scale due to reaching concentrations over 200 mg/L only after 10 years of application.

The residence time was calculated every year for each application rate using Equation 1. Application rate and residence time display a positive relationship with a range of 1,123 to 1,288 days for the rates of 1,000 and 10,000 mg/L (Figure 11). The relationship between application rate and Cl^- residence time is positive; as the application rate increases so increases the residence time. The Cl^- residence time of ~3 years is similar to reported groundwater residence times of 3 years reported in previous studies [75].

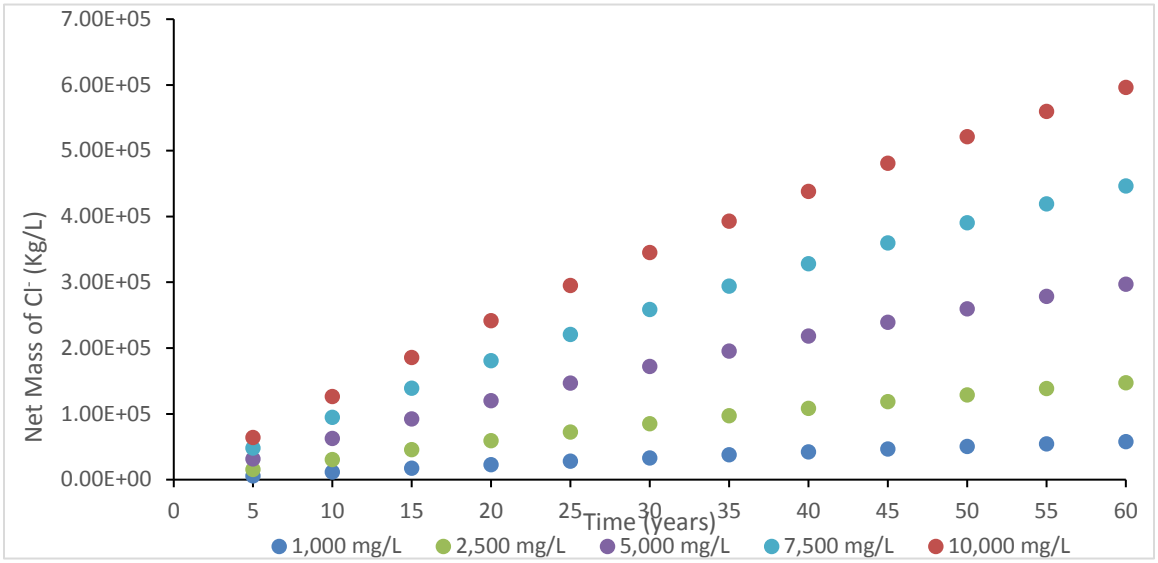

Figure 10: Build-up model results, wherein road salt was applied for 60 winter seasons. Reported are the maximum net mass of Cl^- at the end of each five-year period.

Build-up models were assigned application rates that were held constant for 60 years (Table 2). Application rate has a linear relationship with mass accumulation and groundwater concentration of Cl^-. The maximum Cl^- concentration within all simulations rose annually at a rate greater than 1 mg/L (Figure 8), similar to rates reported by [70]. By year 60, maximum Cl^- concentrations ranged from 197 mg/L to 1,900 mg/L, which are similar to measured Cl^- concentrations in previous studies [70, 72, 76](Figure 8). Alarmingly, all models except rates of 1,000 mg/L and 2,500 mg/L possessed maximum concentrations that exceeded the MCL after 10 years of Cl- application (Figure 8). The net mass accumulation is dependent upon application rate; final net mass ranges from 58 million metric tons to 596 million metric tons, exhibiting a linear relationship with application rates (Figure 10). Lower rates of 1,000 mg/L and 2,500 mg/L reached steady-state conditions at year 60 contrasting higher rates. For the scenarios examining the lower application rates, estimates of time to reach steady state matches those of previous studies [28, 77]. This study's simulations reveal that the watershed exhibits a linear relationship between with Cl^- storage and application rate, which affects steady-state estimates.

Color flood maps of the watershed display the distribution of Cl^- concentrations throughout the watershed (Figure 12). The Cl^- concentration is influenced by the land use of that area. The LKC watershed is 27% urbanized and 69% agricultural land use, both of which have associated Cl^- concentrations. Urbanized areas (i.e. roadways) exhibit the highest Cl^- concentrations, which is analogous with [76]. Agricultural land use have low Cl^- concentrations that range from 10 mg/L to 50 mg/L which is supported by previous studies [70, 76](Figure 5 and Figure 12). Lax, Peterson [24] found that during winter months Cl^- concentrations in an urban stream range between 65 to 1,350 mg/L and for an agricultural stream between 20 and 60 mg/L. In addition, there is a seasonal variance in which spikes of Cl^- are observed in surface waters during winter storm events [25, 34, 70, 78]. Summer Cl^- concentrations can also spike due to contaminated groundwater leaching into LKC [58]. However, this

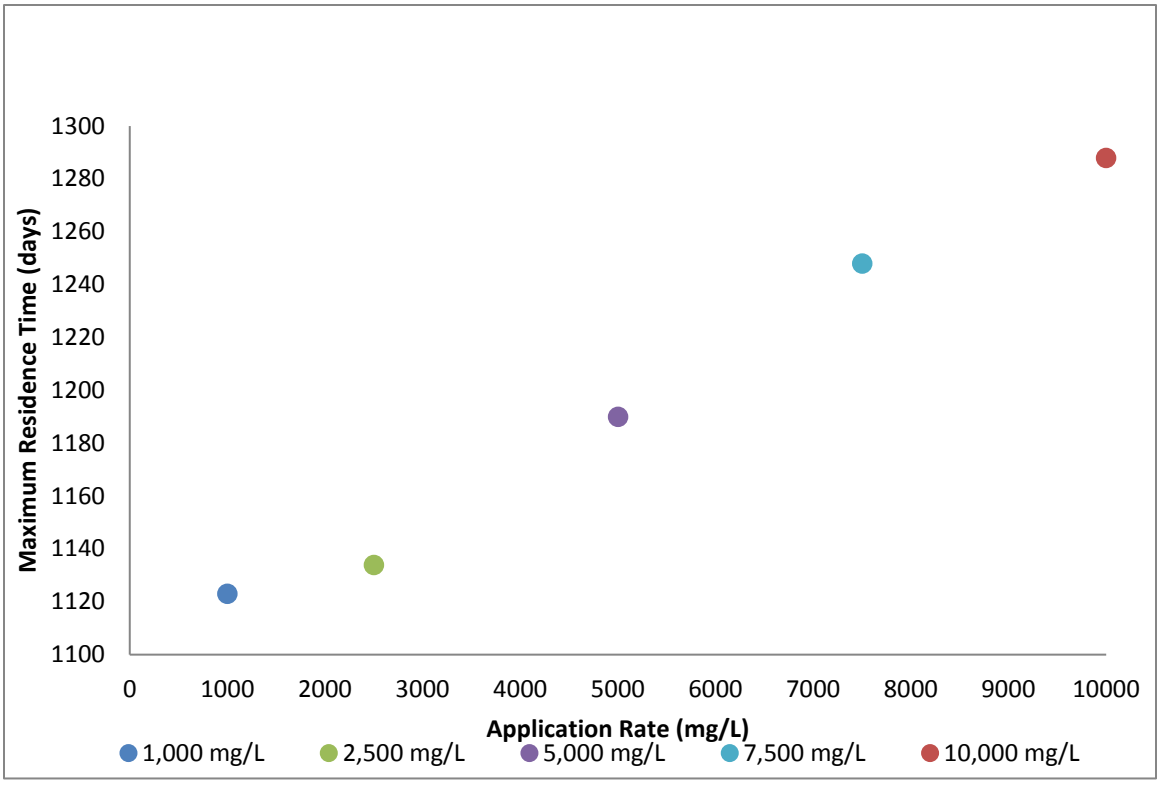

Figure 11: Build up scenario results wherein road salt was applied for 60 winter seasons. Shown is the maximum solute residence time (days) and application rate (mg/L)

solute transport model did not incorporate the transient nature of the stream into the model; rather it examined only the application rates.

Modeling of the watershed revealed 1) the relationship between road salt application rates and mass solute storage and 2) the relationship between road salt application rate and solute residence time. A positive relationship was observed between application rate and mass accumulation. In addition, a positive relationship was observed between application rate and residence time. The time it takes for the watershed to return to safe drinking levels is dependent upon the application rate; as the application rate increases the flush time increases. Steady-state time was also dependent on application rates, wherein a positive relationship was observed.

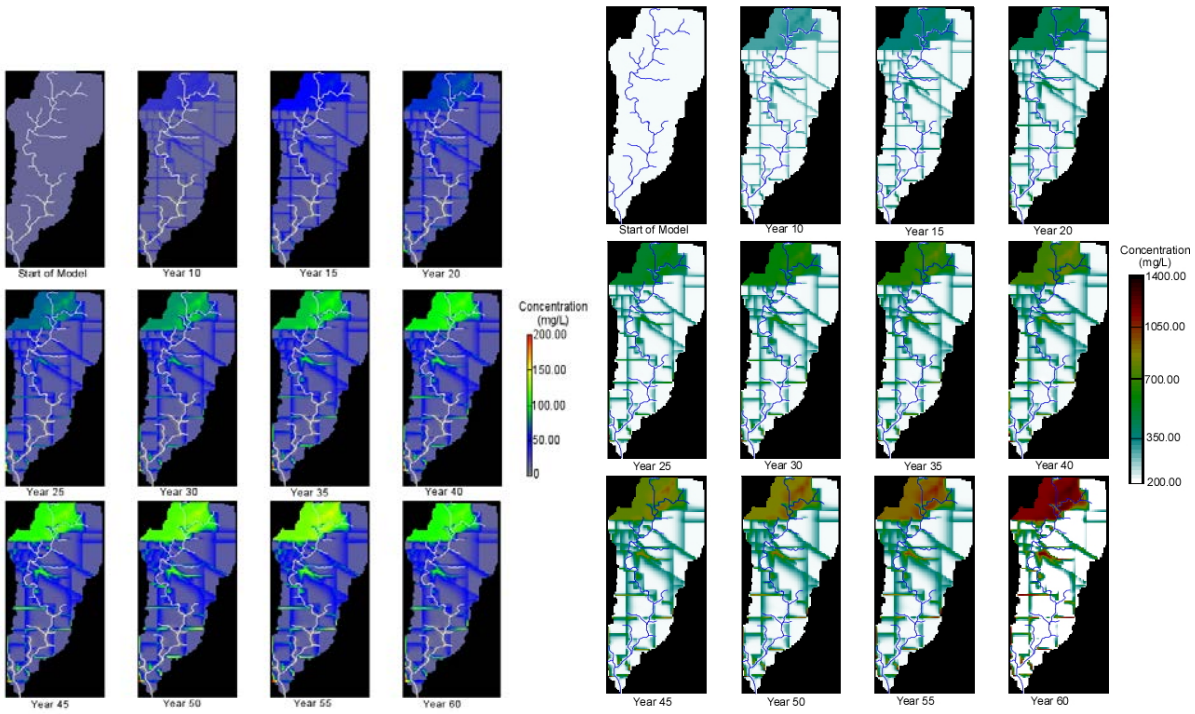

Figure 12: a) Chloride concentration color flood map of model scenario 2 at the 1,000 mg/L application rate. Shown is the model in which road salt was applied for 60 winter seasons and LKC (white). B) Chloride concentration color flood map of model scenario 2 at the 10,000 mg/L application rate. Shown is the model in which road salt was applied for 60 winter seasons and LKC (blue). White areas indicate concentrations at or below 200 mg/L.

The modeling of Cl^- transport in this study reveals the proficiency in which a watershed can store and cleanse road salt. At high application rates, the watershed takes 30 years of no application to return to safe drinking levels, which would not be achievable due to human dependency on deicers. Lower application rates reached steady-state conditions after 60 years of deposition. Presently, watersheds within the Midwest could have reached steady-state conditions with road salt considering application started in the 1960s. Kelly, Panno [75] demonstrated that shallow aquifers within the Chicago metropolitan area have increased in Cl^- concentrations since the 1970s. The Cl^-contaminated groundwater then feeds local streams wherein we observed elevated surface water Cl^- concentrations through non-salting seasons [75]. The results of this study display that elevated Cl^- concentrations in the groundwater can sustain high surface water concentrations through the non-salting season. Therefore, with a continuance of application in the proceeding winters it is possible that surface water Cl^- concentrations will continue to increase through the decades as shown in Kelly, Panno [75] and [4]. Elevated surface waters and groundwater could lead to detrimental effects on the watershed ecosystem.

c. GIS – Regression Modeling

Urban land cover area and kilometers of roads for each sub basin were determined from the urban land cover datasets and road layers, respectively (Table 4). The drainage area, kilometer of roads, and urban land cover area all increase for each location downstream. The initial regression analysis identified the concentration of Cl^- at LKC1, the water day, the water temperature at LKC1, and the drainage area of the sub basin as the significant variables for predicting Cl^- concentrations at the downstream locations, with kilometers of road and land use as insignificant (Table 5). Given the lack of significance, the kilometers of road and land use parameters were removed and a final regression analysis was conducted (Table 6). All parameters remained significant, and the final coefficient values remained the same with the exception of drainage area, which increased slightly.

Table 4: Descriptive data for sub basins.

Location (Sub Basin)	Drainage Area (km^2)	Kilometers of Roads (km)	Urban Land Cover (km^2)
LKC1	25.07	174.7	5.71
LKC2	31.50	208.3	7.22
LKC3	36.80	233.7	7.31
LKC4	40.25	261.4	7.36
LKC5	47.58	294.8	7.42
LKC6	55.99	322.3	7.48
LKC7	57.45	330.3	7.48

Table 5: Results of initial regression analysis. Bold values parameters that were not significant.

Parameter	Standard Coefficient	Significance (p-value)
Concentrations at LKC1	0.636	0.000
Water Day	-0.146	0.029
Water temperature LKC1	-0.279	0.001
Roads (km)	-0.0006	0.666
Drainage area (km^2)	0.484	0.033
Urban land cover (km^2)	7.65×10^{-6}	0.402

Table 6: Results of final regression analysis, land use and roads were not used.

Parameter	Standard Coefficient	Significance (p-value)
Concentrations at LKC1	0.632	0.000
Water Day	-0.146	0.028
Water temperature LKC1	-0.281	0.000
Drainage area (km^2)	-0.124	0.032

The linear regression model, generated from the parameter coefficients, simulated chloride concentrations at all locations downstream from LKC1. The model over-predicted the concentrations at LKC4, LKC5, LKC6, and LKC7 and under-predicted the concentrations at LKC2 and LKC3 (Figure 13). Values used to test the models accuracy were not included in the construction of the linear model. The highest errors were associated with the locations farthest downstream from LKC1, LKC6 and LKC7 (Figure 13). Overall, the model produced a mean absolute error (MAE) of 15.39 mg/L.

The regression analysis indicates the only independent variable per sub basin is the drainage area of the sub basin. The regression model did not compensate for any other parameter. Lax [79] identified a relationship between chloride concentrations and land-use and found that land-use was a controlling factor of surface stream quality. Streams with their headwaters originating in urban areas have much higher chloride concentrations than those originating in agricultural areas [79]. The current regression model is not differentiating the upstream areas, which receive most of its water from the impacted urban runoff, from the downstream areas, which receive the majority of its water from groundwater infiltrating from agricultural areas. Dilution is a major controlling factor for chloride concentrations as high stream flow correlates with lower chloride concentrations [78, 80]. The land-use pattern of the watershed may play a role in the predictive use of the regression analysis. Moving downstream, the percentage of urban land use decreases as the drainage area increases. The larger drainage results in greater discharge, with water added from groundwater input [58, 59, 63]. The linear regression model is not compensating for the differences in water added to the stream at the upstream and downstream locations. The baseflow water adding to the upstream locations should have similar concentrations to the upstream locations so little dilution should occur. However, downstream baseflow waters, draining agricultural areas, have lower concentration relative to the waters in the downstream sites. Therefore, the dilution effectively lowers the concentration while maintaining the load, which is seen in the field data (Figure 2).

VI. Significance

Outcomes from these activities present spatial and temporal data for Cl^- within a watershed impacted by deicing agents. Results identify seasonal trends in the concentration of Cl^- in the LKC watershed, with elevated concentrations in the winter. However, periodic spikes during the summer follow precipitation events. The spikes appear to be associated with Cl^- stored within the aquifer system that is released in response to infiltration associated with the precipitation events. The continued use of roads salts will continue to elevate the concentration of Cl^- with in the waters. If the application of Cl^- ceased, the watershed would not fully recover within 50 years. Residual Cl^- would remain in the system. The numerical modeling approach provides an initial evaluation; additional modeling incorporating transient flow will be needed to support all future research activities and develop appropriate BMPs for Cl^- applications.

The Illinois State Geological Survey and the Illinois State Water Survey have examined the issue of road salts in the Chicago metropolitan area and the subsequent effects on the Illinois River watershed [5, 13, 36, 70, 80-82]. A pilot GIS model developed to evaluate the transport and fate of Cl^- within Illinois indicated that data are spatially and temporally too variable to accurately assess the problem [83]. Our data indicate suggest a balance between spatial resolution and temporal resolution exists. While our sampling points were closer together, the 2-week time period was to coarse to model accurately the pulse of Cl- moving through the system. A finer temporal resolution is needed to develop more adequate GIS and flow models.

Increases in road salts use, leading to increases in stream/groundwater chloride concentrations, are fueling the need for useful tools to study chloride fate and transport. Linear regression modeling has been used many times to predict the movement of a contaminant and is used here to predict chloride concentrations downstream. Land cover, representing impervious surfaces, drainage area, and discharge are all controlling factors in chloride concentration downstream, however there must be other factors controlling chloride concentration other than the ones viewed in this study. This study also revealed that there is an impacted area around an urban setting. Chloride concentrations are less diluted upstream due to the chlorides stored and discharging into the upstream sites. More dilution occurs downstream due to the waters discharging into downstream locations are agriculturally derived.

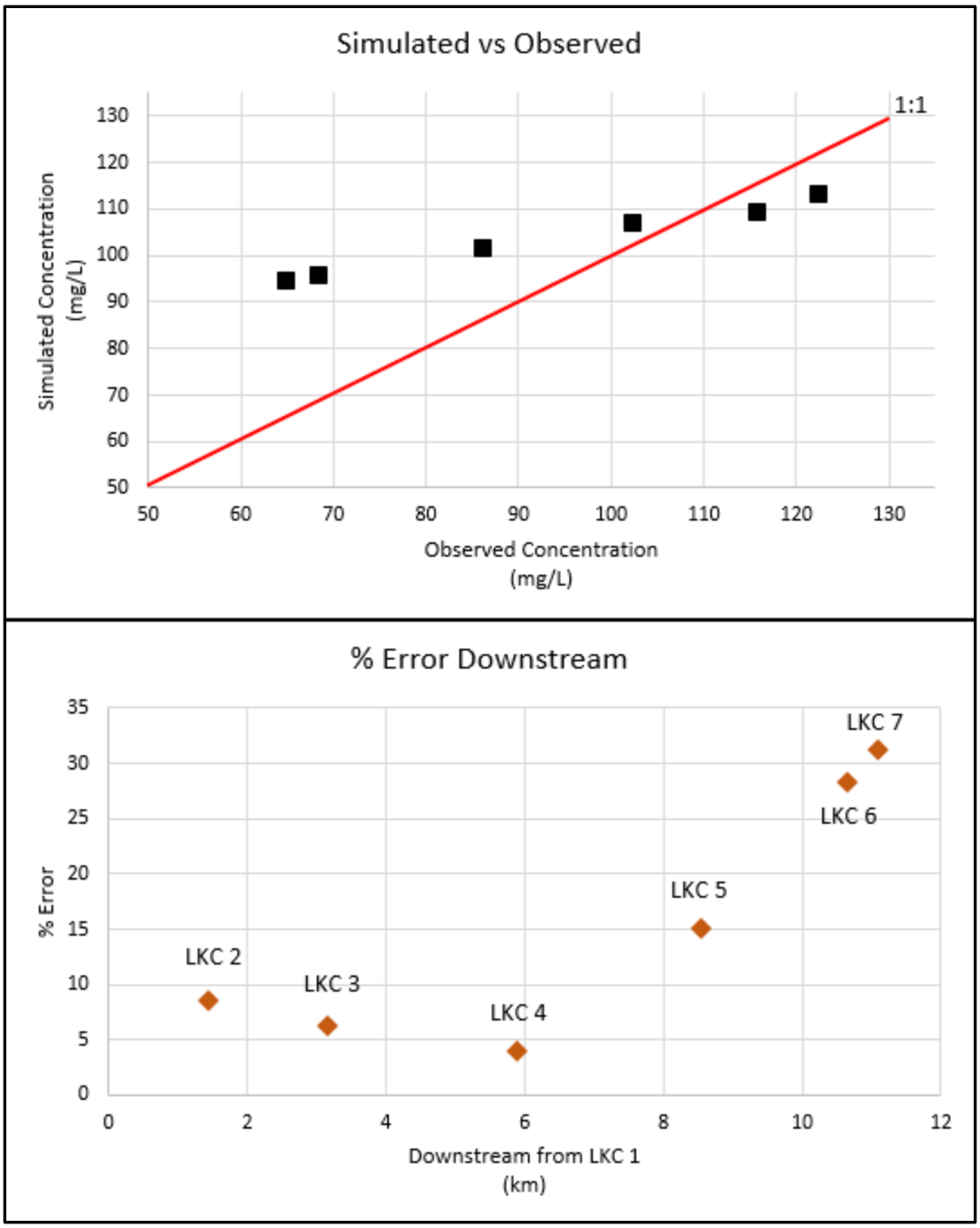

Figure 13: a) Observed versus simulated Cl- concentrations; b) Error in Cl- concentration at the downstream locations (LKC2-LKC7).

VII. Students supported

A total of five students were involved in the project: Graduate students Jessica Ludwikowski and Lucas Chabela; Undergraduate students Kyagaba David Lwanga, Alan Jensen; and Clint Updike. Direct support was provided to Mr. Chabela, Mr. Jensen, and Mr. Updike. Ms. Ludwikowski and Mr. Lwanga were involved through independent research. Below, I provide a more detailed description of the students' role and status.

Jessica Ludwikowski – MS 2016, Ms. Ludwikowski generated the groundwater flow (MODFLOW) and Cl^- transport model (MT3D) for the watershed, which served as her thesis research. Upon graduation, Ms. Ludwikowski began a position as an Environmental Control Engineer with the Cook County Department of Environmental Control.

Lucas Chabela – MS 2017, Mr. Chabela served as the lead student on the project. Mr. Chabela conducted the two-week stream sampling events. In addition to coordinating and collecting the water samples, Mr. Chabela developed a bank-storage model (MODFLOW) to examine Cl^- storage along the stream; this project served as his thesis research. Lucas was instrumental in the development of the GIS analysis to model concentrations within the watershed using the water sample data. Lucas is a May 2017 graduate and is in the process of finding employment.

Kyagaba David Lwanga – BS 2016, Mr. Lwanga was involved in water sampling and the initial GIS development. He participated in both the collection of water samples and the analysis of the samples. Upon graduation, Mr. Lwanga took a position as a GIS analyst at ExteNet Systems in Lisle, IL.

Alan Jensen – BS 2016, Upon Mr. Lwanga's graduation, Mr. Jensen began assisting Mr. Chabela in the collection of water samples. As a result of his schedule, Mr. Jensen's involvement was limited to sample preparation, sample collection, and data entry. After graduation, Mr. Jensen began working for Mostardi Platt, an environmental consulting firm in Chicago.

Clint Updike – BS expected 2018, Mr. Updike transitioned into the project as Mr. Jensen was about to graduate. Mr. Updike was involved with sample preparation, sample collection, and data entry. More recently, Mr. Updike began examining the data as part of an independent research project that he will complete during the next academic year. He has plans to present the work at the North-Central GSA meeting in Ames, Iowa in April 2018.

GEO 444 – Applied Groundwater Modeling: The data collected during the project will be incorporated into the curriculum of the Applied Groundwater Modeling course. Students will use the data in two projects: 1) a geostatiscal model to assess the temporal trends of the data and 2) a 1-D transient storage model development. While the thesis work by Ms. Ludwikowski and Mr. Chabela provide these answers, the data set is well-suited for student learning. The patterns that are present, the natural variability in the data, and the imperfections in the data provide students an opportunity to exam and to discuss how to incorporate imperfect the data into the models.

VIII. Publications

a. MS Thesis

Ludwikowski, J., 2016, The transport and fate of chloride within the groundwater of a mixed urban and agricultural watershed: Normal, IL, Illinois State University, 56 p.

Chabela, L., 2017, Using 3-D modeling to describe the relationship between peak stage, storm duration, and bank storage and the implications along a meandering stream in central Illinois: Normal, IL, Illinois State University, 57 p.

b. Peer-Reviewed Academic Journals

None at this time. I am developing two papers based upon the MS theses of Ms. Ludwikowski and Mr. Chabela. Additional papers are planned to examine the seasonal variation of Cl- in the watershed.

c. Presentations

Peterson, E.W., and Ludwikowski, J.*, (2016) Transport and fate of chloride within the groundwater of a mixed urban and agricultural watershed, Illinois Water Conference, October 26, 2016.

Chabela, L. P.*, Peterson, E. W., Miller, J.*, (2016) Seasonal variation of chloride inputs from road salt application in a mixed urban/agricultural watershed in central Illinois, Abstract with Programs - Geological Society of America, September 2016, Vol. 48, No. 7, doi: 10.1130/abs/2016AM-287247

Ludwikowski, J.*, and Peterson, E.W., (2016) Transport and fate of chloride within the groundwater of a mixed urban and agricultural watershed, Illinois Groundwater Association, April 20, 2016.

Additional presentations in 2017-2018 are planned at the 2017 annual GSA meeting, the 2018 North-Central GSA meeting, the Illinois Water Conference, and an Illinois Groundwater Association meeting.

IX. References

1. Meriano, M., N. Eyles, and K.W.F. Howard, *Hydrogeological impacts of road salt from Canada's busiest highway on a Lake Ontario watershed (Frenchman's Bay) and lagoon, City of Pickering.* Journal of Contaminant Hydrology, 2009. **107**(1–2): p. 66-81.
2. Environment Canada, *Priority substances list assessment report: Road Salts*, Health Canada, Editor. 2001, Minister of Public Works and Government Services. p. 171.
3. Gardner, K.M. and T.V. Royer, *Effect of Road Salt Application on Seasonal Chloride Concentrations and Toxicity in South-Central Indiana Streams.* J. Environ. Qual., 2010. **39**(3): p. 1036-1042.
4. Kelly, V.R., et al., *Long-term sodium chloride retention in a rural watershed: Legacy effects of road salt on streawater concentration.* Environmental Science & Technology, 2008. **42**(2): p. 410-415.
5. Panno, S.V., et al., *Characterization and identification of Na-Cl sources in ground water.* Ground Water, 2006. **44**(2): p. 176-187.
6. Locat, J. and P. Gélinas, *Infiltration of de-icing road salts in aquifers: the Trois-Rivières-Ouest case, Quebec, Canada.* Canadian Journal of Earth Sciences, 1989. **26**(11): p. 2186-2193.
7. Marsalek, J., *Road salts in urban stormwater: an emerging issue in stormwater management in cold climates.* Water Science & Technology, 2003. **48**(9): p. 61-70.
8. Novotny, E.V., et al., *Chloride ion transport and mass balance in a metropolitan area using road salt.* Water Resources Research, 2009. **45**(12): p. n/a-n/a.
9. Jackson, R.B. and E.G. Jobbágy, *From icy roads to salty streams.* Proceedings of the National Academy of Sciences of the United States of America, 2005. **102**(41): p. 14487-14488.
10. Kostick, D.S., J.A. Milanovich, and R.R. Coleman, *2005 Minerals Yearbook: Salt*, U.S.G. Survey, Editor. 2007, U.S. Geological Survey. p. 21.
11. Friederici, P., *Salt on earth.* Chicago Wilderness Magazine, Winter, Chicago, 2004.
12. Keseley, S., *Road salt is a slippery subject.* Lake County Health Department and Community Health Center Cattail Chronicles, 2006. **16**(1): p. 4-5.
13. Kelly, W.R., S.V. Panno, and K.C. Hackley. *Impacts of road salt on water resources in the Chicago region*. in *2009 UCOWR conference*. 2009. Southern Illinois University, Carbondale, IL.
14. Church, P.E. and P.J. Friesz, *Effectiveness of Highway Drainage Systems in Preventing Road-Salt Contamination of Groundwater: Preliminary Findings*. Transportation Research Record, ed. T.R. Record. Vol. 1420. 1993, Washington, DC Transportation Research Record. 64.
15. Ruth, O., *The effects of de-icing in Helsinki urban streams, Southern Finland.* Water Science and Technology, 2003. **48**(9): p. 33-43.
16. Bäckström, M., et al., *Speciation of Heavy Metals in Road Runoff and Roadside Total Deposition.* Water, Air, and Soil Pollution, 2003. **147**(1-4): p. 343-366.
17. Godwin, K.S., S.D. Hafner, and M.F. Buff, *Long-term trends in sodium and chloride in the Mohawk River, New York: the effect of fifty years of road-salt application.* Environmental Pollution, 2003. **124**(2): p. 273-281.
18. Koryak, M., et al., *Highway Deicing Salt Runoff Events and Major Ion Concentrations along a Small Urban Stream.* Journal of Freshwater Ecology, 2001. **16**(1): p. 125-134.
19. Scott, W.S., *The effect of road deicing salts on sodium concentration in an urban water-course.* Environmental Pollution (1970), 1976. **10**(2): p. 141-153.

20. Howard, K.W.F. and P.J. Beck, *Hydrogeochemical implications of groundwater contamination by road de-icing chemicals.* Journal of Contaminant Hydrology, 1993. **12**(3): p. 245-268.
21. Bowen, G.S. and M.J. Hinton. *The temporal and spatial impacts of road salt on streams draining the Greater Toronto Area*. in *Proceedings of the Groundwater in A Watershed Context Symposium*. 1998. Burlington, Ontario: Ontario Ministry of the Environment and Geological Survey of Canada.
22. Warren, L.A. and A.P. Zimmerman, *The influence of temperature and NaCl on cadmium, copper and zinc partitioning among suspended particulate and dissolved phases in an urban river.* Water Research, 1994. **28**(9): p. 1921-1931.
23. Kaushal, S.S., et al., *Increased salinization of fresh water in the northeastern United States.* Proceedings of the National Academy of Sciences of the United States of America, 2005. **102**(38): p. 13517-13520.
24. Lax, S.M., E.W. Peterson, and S. Van der Hoven, *Quantifying Stream chloride concentrations as a function of land-use.* Water, Air, and Soil Pollution, *in review*.
25. Perera, N., B. Gharabaghi, and K. Howard, *Groundwater chloride response in the Highland Creek watershed due to road salt application: A re-assessment after 20 years.* Journal of Hydrology, 2013. **479**: p. 159-168.
26. Marsalek, J., et al., *Review of operation of urban drainage systems in cold weather: water quality considerations.* Water Science and Technology, 2003. **48**(9): p. 11-20.
27. Viklander, M., et al., *Urban drainage and highway runoff in cold climates: conference overview.* Water Science and Technology, 2003. **48**(9): p. 1-10.
28. Howard, K.W.F. and J. Haynes, *Groundwater contamination due to road de-icing chemicals--Salt balance implications.* Geoscience Canada, 1993. **20**(1): p. 1-8.
29. Karraker, N.E., J.P. Gibbs, and J.R. Vonesh, *Impacts of Road Deicing Salt on the Demography of Vernal Pool-Breeding Amphibians.* Ecological Applications, 2008. **18**(3): p. 724-734.
30. Lax, S. and E.W. Peterson, *Characterization of chloride transport in the unsaturated zone near salted road.* Environmental Geology, 2009. **58**(5): p. 1041-1049.
31. Miklovic, S. and S. Galatowitsch, *Effect of NaCl andTypha angustifolia L. on marsh community establishment: A greenhouse study*. Wetlands, 2005. **25**(2): p. 420-429.
32. Rosenberry, D.O., et al., *Movement of Road Salt to a Small New Hampshire Lake* Water, Air, & Soil Pollution, 1999. **109**(1-4): p. 179-206 DOI 10.1023/A:1005041632056
33. Siver, P.A., et al., *Historical changes in Connecticut lakes over a 55-year period.* Journal of Environmental Quality, 1996. **25**(2): p. 334-345.
34. Williams, D.D., N.E. Williams, and Y. Cao, *Road salt contamination of groundwater in a major metropolitan area and development of a biological index to monitor its impact.* Water Research, 2000. **34**(1): p. 127-138.
35. Watson, L.R., et al., *Effects of highway-deicer application on ground-water quality in a part of the Calumet Aquifer, Northwestern Indiana*, U.G. Survey, Editor. 2002, US Department of the Interior, US Geological Survey.
36. Panno, S.V., et al., *Impact of urban development on the chemical composition of ground water in a fen-wetland complex.* Wetlands, 1999. **19**(1): p. 236-245.
37. Mayer, T., et al., *Impact of road salts on small urban ponds: Rouge River pond case study*, N.W.R. Institute, Editor. 1999, National Water Research Institute: Burlington, Ontario.
38. Wegner, W. and M. Yaggi, *Environmental Impacts of Raod Salt and Alternatives in the New York City Watershed.* Stormwater, 2001. **2**(5): p. http://www.forester.net/sw_0107_environmental.html.
39. Demers, C.L., *Effects of road deicing salt on aquatic invertebrates in four Adirondack streams*, in *Chemical deicers and the environment*, F.M. D'Itri, Editor. 1992, Lewis Publishing: Boca Raton, Florida.
40. Crowther, R.A. and H.B.N. Hynes, *The effect of road deicing salt on the drift of stream benthos.* Environmental Pollution (1970), 1977. **14**(2): p. 113-126.

41. Molles, M., *Effects of road salting on stream invertebrate communities.* Eisenhower Consortium Bulletin, 1980. **10**: p. 1-9.
42. Hart, B., et al., *A review of the salt sensitivity of the Australian freshwater biota.* Hydrobiologia, 1991. **210**(1-2): p. 105-144.
43. Fay, L. and X. Shi, *Environmental Impacts of Chemicals for Snow and Ice Control: State of the Knowledge.* Water, Air, & Soil Pollution, 2012. **223**(5): p. 2751-2770.
44. Seilheimer, T., et al., *Impact of urbanization on the water quality, fish habitat, and fish community of a Lake Ontario marsh, Frenchman's Bay.* Urban Ecosystems, 2007. **10**(3): p. 299-319.
45. Sanzo, D. and S.J. Hecnar, *Effects of road de-icing salt (NaCl) on larval wood frogs (Rana sylvatica).* Environmental Pollution, 2006. **140**(2): p. 247-256.
46. Birge, W., et al., *Recommendations on numerical values for regulating iron and chloride concentrations for the purpose of protecting warm water species of aquatic life in the Commonwealth of Kentucky.* Memorandum of Agreement, 1985. **5429**.
47. Evans, M. and C. Frick, *The effects of road salts on aquatic ecosystems*. 2001, National Water Research Institute, Environmental Canada: Ottawa, Canada.
48. Richburg, J., W. Patterson, and F. Lowenstein, *Effects of road salt and Phragmites australis invasion on the vegetation of a Western Massachusetts calcareous lake-basin fen.* Wetlands, 2001. **21**(2): p. 247-255.
49. Foos, A., *Spatial distribution of road salt contamination of natural springs and seeps, Cuyahoga Falls, Ohio, USA.* Environmental Geology, 2003. **44**(1): p. 14-19.
50. Fraser, D. and E.R. Thomas, *Moose-Vehicle Accidents in Ontario: Relation to Highway Salt.* Wildlife Society Bulletin (1973-2006), 1982. **10**(3): p. 261-265.
51. Bollinger, T.K., P. Mineau, and M.L. Wickstrom, *Toxicity of sodium chloride to house sparrows (Passer domesticus).* Journal of Wildlife Diseases, 2005. **41**(2): p. 363-370.
52. Wilcox, D.A., *The effects of deicing salts on vegetation in Pinhook Bog, Indiana.* Canadian Journal of Botany, 1986. **64**(4): p. 865-874.
53. United States Environmental Protection Agency. *National recommended water quality criteria - aquatic life criteria table*. [cited 2017; Available from: https://www.epa.gov/wqc/national-recommended-water-quality-criteria-aquatic-life-criteria-table.
54. Findlay, S.E.G. and V.R. Kelly, *Emerging indirect and long-term road salt effects on ecosystems.* Annals of the New York Academy of Sciences, 2011. **1223**(1): p. 58-68.
55. U.S. Census Bureau. *State and County QuickFacts*. 2015 [cited 2015; Available from: http://quickfacts.census.gov/qfd/states/17/1706613.html.
56. Illinois State Water Survey, *Illinois Water and Climate Summary*. 2004.
57. Beach, V. and E.W. Peterson, *Variation of hyporheic temperature profiles in a low gradient third-order agricultural stream – A statistical approach.* Open Journal of Modern Hydrology, 2013. **3**(2): p. 55-66.
58. Peterson, E.W. and C. Benning, *Factors influencing nitrate within a low-gradient agricultural stream.* Environmental Earth Sciences, 2013. **68**(5): p. 1233-1245.
59. Peterson, E.W. and T.B. Sickbert, *Stream water bypass through a meander neck, laterally extending the hyporheic zone.* Hydrogeology Journal, 2006. **14**(8): p. 1443-1451.
60. Peterson, E.W., T.B. Sickbert, and S.L. Moore, *High frequency stream bed mobility of a low-gradient agricultural stream with implications on the hyporheic zone.* Hydrological Processes, 2008. **22**(21): p. 4239-4248.
61. Sickbert, T.B. and E.W. Peterson, *The effect of surface water velocity on hyporheic interchange.* Journal of Water Resource and Protection, 2014. **6**(4): p. 327-336.
62. Van der Hoven, S.J., N.J. Fromm, and E.W. Peterson, *Quantifying nitrogen cycling beneath a meander of a low gradient, N-impacted, agricultural stream using tracers and numerical modelling.* Hydrological Processes, 2008. **22**(8): p. 1206-1215.

63. Bastola, H. and E.W. Peterson, *Heat tracing to examine seasonal groundwater flow beneath a low-gradient stream.* Hydrogeology Journal, 2016. **24**(1): p. 181-194.
64. Mosley, M.P. and A.I. McKerchar, *Streamflow*, in *Handbook of Hydrology*, D.R. Maidment, Editor. 1993, McGraw Hill: New York. p. 8.1-8.39.
65. Harbaugh, A.W., et al., *MODFLOW-2000, The U. S. Geological Survey Modular Ground-Water Model-User Guide to Modularization Concepts and the Ground-Water Flow Process*, in *Open-File Report 00-92*, U. S. Geological Survey, Editor. 2000, U. S. Geological Survey,: Reston, VA. p. 134.
66. Zheng, C. and P.P. Wang, *MT3DMS: A Modular Three-Dimensional Multispecies Transport Model for Simulation of Advection, Dispersion, and Chemical Reactions of Contaminants in Groundwater Systems; Documentation and User's Guide*. Vol. Contract Report SERDP-99-1. 1999, Vicksburg, MS: U.S. Army Engineer Research and Development Center.
67. U.S. Geological Survey, *National Geospatial Technical Operations Center*. 2014, U.S. Geological Survey,.
68. Ackerman, J.R., et al., *Quantifying nutrient removal from groundwater seepage out of constructed wetlands receiving treated wastewater effluent.* Environmental Earth Sciences, 2015. **74**(2): p. 1633-1645.
69. Giadom, F.D., E.G. Akpokodje, and A.C. Tse, *Determination of migration rates of contaminants in a hydrocarbon-polluted site using non-reactive tracer test in the Niger Delta, Nigeria.* Environmental Earth Sciences, 2015. **74**(1): p. 879-888.
70. Kelly, W.R., *Long-term trends in chloride concentrations in shallow aquifers near Chicago.* Ground Water, 2008. **46**(5): p. 772-781.
71. Craun, K.J., et al., *The National Geospatial Technical Operations Center*, in *Fact Sheet*. 2009.
72. Kelly, W.R. and G.S. Roadcap. *Shallow ground-water chemistry in the Lake Calumet area, Chicago, Illinois*. in *of the National Symposium on Water Quality*. 1994. American Water Resources Association, .
73. Dingman, S.L., *Physical Hydrology*. Second ed. 2002, Upper Saddle River: Prentice Hall. 646.
74. Bester, M.L., et al., *Numerical Investigation of Road Salt Impact on an Urban Wellfield.* Ground Water, 2006. **44**(2): p. 165-175.
75. Kelly, W.R., S.V. Panno, and K.C. Hackley, *Impacts of Road Salt Runoff on Water Quality of the Chicago, Illinois, Region.* Environmental & Engineering Geoscience, 2012. **18**(1): p. 65-81.
76. Panno, S.V., et al., *Database for the Characterization and Identification of the Sources of Sodium and Chloride in Natural Waters of Illinois*, I.S.G. Survey, Editor. 2005, Illinois State Geological Survey: Champaign, Illinois. p. 21.
77. Boutt, D.F., et al., *Identifying potential land use-derived solute sources to stream baseflow using ground water models and GIS.* Ground Water, 2001. **39**(1): p. 24-34.
78. Corsi, S.R., et al., *River chloride trends in snow-affected urban watersheds: increasing concentrations outpace urban growth rate and are common among all seasons.* Science of The Total Environment, 2015. **508**: p. 488-497.
79. Lax, S.M., *Estimating stream chloride concentrations as a function of land use change for two small watersheds in central Illinois*, in *Geography-Geology*. 2007, Illinois State University: Normal, IL. p. 44.
80. Kelly, W.R., et al., *Using chloride and other ions to trace sewage and road salt in the Illinois Waterway.* Applied Geochemistry, 2010. **25**(5): p. 661-673.
81. Panno, S.V., et al., *Estimating background and threshold nitrate concentrations using probability graphs.* Ground Water, 2006. **44**(5): p. 697-709.
82. Roadcap, G.S. and W.R. Kelly, *Shallow ground-water quality and hydrogeology of the Lake Calumet area, Chicago, Illinois*. 1994: Illinois State Water Survey.
83. Eggert, M., R. Rowley, and E.W. Peterson, *Chloride Levels in Illinois Rivers and Streams*, in *AAG Annual Meeting*. 2015: Chicago, IL.

Evaluating Water Quantity and Water Quality Issues in Illinois Streams using Large-Scale Particle Image Velocimetry (LSPIV)

Basic Information

Title:	Evaluating Water Quantity and Water Quality Issues in Illinois Streams using Large-Scale Particle Image Velocimetry (LSPIV)
Project Number:	2016IL314B
Start Date:	3/1/2016
End Date:	2/28/2017
Funding Source:	104B
Congressional District:	IL-15
Research Category:	Climate and Hydrologic Processes
Focus Category:	Hydrology, Surface Water, Water Quality
Descriptors:	None
Principal Investigators:	Bruce L. Rhoads

Publications

There are no publications.

"Evaluating Water Quantity and Water Quality Issues in IL Streams using Large-Scale Particle Image Velocimetry"

Co-PI's Quinn Lewis, Bruce Rhoads, Frank Engel

Problem and Research Objectives

River flow velocity and discharge, the product of velocity and cross-sectional area, are two of the most fundamental measurements routinely used to characterize rivers. Discharge is the basic unit that defines flow quantity and therefore is essential for studies ranging from assessments of flooding risk, to ecological habitat water requirements, to extraction of water for human use. Flow velocity measurements are necessary to understand the work that rivers accomplish, such as channel bed and bank erosion or flow constituent mixing and flow momentum transfer. The magnitude and pattern of flow velocity governs the transport of constituents carried by the flow, so the ability to accurately measure velocity in natural systems is crucial for improved understanding of many problems related to water quality. However, the ability to measure both flow velocity and discharge in rivers can be limited with traditional methods and equipment when flows are very high and dangerous, too low to accommodate sensors in the water column, or highly spatially or temporally variable.

Large-scale particle image velocimetry (LSPIV), a state-of-the-art imagery-based velocity measurement technique, might partially address some of these limitations. LSPIV is inexpensive in comparison to methods commonly used by the United States Geological Survey (USGS) to obtain discharge at gaging sites. LSPIV can also yield high spatial and temporal resolution surface flow fields in rivers, which represent an important complement to in-stream measurements typically used to characterize flow velocity. The main objective of this study was to explore the utility of LSPIV to address problems related to water quantity and water quality in Illinois. This research focused on the ability of LSPIV to be a low-cost alternative for measuring discharge (i.e. *water quantity*) in comparison to traditional acoustic and propeller methods in a variety of flow environments and field sites. This research also focused on the utility of LSPIV for detailed surface flow measurements at river confluences

in support of an ongoing study of flow mixing at these hydrodynamically complex regions (i.e. *water quality*). An additional focus of this research was to compare LSPIV results from both a tripod-mounted camera and from a drone (herein referred to as an Unmanned Aerial System, UAS).

Methodology

LSPIV datasets were obtained with two related but distinct field setups. First, we mounted a small action camera to an extendable tripod. At the stream confluence study sites, where we used LSPIV to complement an ongoing study of flow mixing, we deployed the camera at both an angle oblique to the water surface as well as oriented vertically downward. We placed and surveyed ground control points in the field of view to rectify the resulting imagery. A similar tripod setup was used at bridges to determine discharge, but the camera was always oriented vertically downward. The second method used to obtain LSPIV was from the camera affixed to the UAS. We navigated the UAS over the region of interest and recorded video while the UAS was locked in position using on-board GPS.

During both the tripod and UAS recordings, workers manually spread small pine wood shavings onto the surface of the water. Occasionally, we imaged the water surface without adding wood tracers to assess the quality of naturally-occurring tracer particles like leaf litter and bubbles. The resultant videos were edited and individual frames were extracted. These frames were then uploaded to the open-source MATLAB program PIVLab, where surface velocity was determined from the movement of the wood tracers per unit time between frames. Secondary datasets, such as cross-sectional velocity or surface velocity fields, were subsequently derived from data obtained using PIVLab.

In concert with these LSPIV measurements, we obtained additional field data. In the study of flow mixing at stream confluences, we obtained LSPIV data in support of ongoing work that measured 3D flow velocity, water temperature, water conductivity, and water turbidity. The resultant LSPIV surface velocity field was used as a complement to the in-stream data. In the study of flow discharge, we

also obtained discharge measurements using either a hand-operated propeller meter, an acoustic Doppler current profiler (ADCP), or both. We also measured at USGS gage sites for an additional reference discharge value.

Principal Findings

We are still engaged in the process of interpreting our data, but can demonstrate numerous key findings. First, in relation to measurements of river discharge, the performance of the tripod-mounted LSPIV and the UAS LSPIV was nearly identical in each case where both methods were used. We found that when the tripod is extended high enough to view the entire channel width, the camera oscillates in the wind. The UAS is also not completely steady, but after about 30 seconds (depending on wind speed and height above the water surface), mean velocities are generally unaffected by camera movement. While in certain situations, such as in narrow, tree-lined rivers, in restricted flight zones, or when no certified UAS operator is present, it may be beneficial to use a tripod-mounted camera, in many situations the UAS is a more flexible option for obtaining mean surface velocity and therefore discharge. The UAS can more easily image wide rivers and the field of view can be adjusted on the fly in response to changing conditions.

In addition, LSPIV discharge from both the tripod and UAS compared favorably with the propeller and ADCP discharge and were often within a few percent of these reference values. Our results generally support the typical practice of relating depth-averaged velocity to surface velocity with a simple coefficient in the range of 0.85 – 0.9, but additional research into this is ongoing. Finally, we found that in some low and high flow conditions, the LSPIV discharge was close to the reference discharges measured by the research team but significantly (>25 %) different than the USGS gage. Overall, both the tripod and UAS methods resulted in rapid, accurate discharge calculations with respect to reference methods.

Second, we found that LSPIV is an important complement to traditional velocity measurements and can enrich our understanding of flow in complex hydrodynamic environments like confluences. Not only can LSPIV be used for qualitative flow visualization, useful for comparison among field sites and flow events and with numerical modeling, but quantitative information can be obtained over a large spatial scale. UAS greatly increases the capability to obtain LSPIV over a large area, and mean flow velocities are relatively easy to obtain. It is generally more difficult to obtain quasi-instantaneous flow "snapshots", especially as camera height above the water and magnitude of camera movement/oscillation increases. Under favorable circumstances, however, flow snapshots can be obtained from both tripod mounted and UAS LSPIV.

Significance

The results of this research are applicable to many disciplines in which accurate measurement of flow quantity and quality is desired. We expect continued collaboration with the USGS to more thoroughly investigate the challenges of stream gaging with LSPIV, but early results from this research are promising. In particular, this work indicates that rapidly mobilized campaigns using simple methods and inexpensive camera equipment can result in accurate discharge measurements in a variety of natural environments. These methods might address situations where traditional sensors are limited or difficult to operate, such as in floods, extremely low flows, or in rapidly changing flow conditions. We expect to produce a detailed set of recommendations reflecting our experience with LSPIV gaging, focusing on the challenges and opportunities of using UAS.

Interpretation of LSPIV results for confluence mixing is ongoing, but the significance of these results is clear. We have already used flow visualization from UAS imagery to compare our field data to numerical results and expect to use the resultant surface flow fields to enrich our understanding of in-stream measurements of velocity and mixing. LSPIV, specifically deployed from UAS, appears to be a

promising way to rapidly and inexpensively supplement traditional measurements with high-spatial resolution surface velocity fields. More research is required to consistently obtain quasi-instantaneous flow snapshots, and addressing this problem should continue to be fertile ground for future research.

In sum, we found that LSPIV should continue to be used as a complement to traditional discharge and velocity measurements, especially as the method matures and becomes interwoven with improved sensor and computing technologies. LSPIV velocity fields are an important complement to traditional field velocity measurements especially in complex flows, and cameras deployed both in fixed and UAS configurations can yield rapid, accurate mean flow and discharge measurements in a variety of field conditions.

Student Support

This grant has supported Quinn Lewis' dissertation, and at least one chapter is directly based on results in support of this grant. Equipment purchased through this grant has also indirectly supported additional dissertation work and other current projects Mr. Lewis is and will be participating in, such as high-resolution UAS surveys of field sites. Money awarded from this grant paid the salary of undergraduate student Nisarg Shah, in the Department of Natural Resources and Environmental Sciences at the University of Illinois. Mr. Shah gained valuable research experience over the Summer of 2016 and participated in all aspects of field work, as well as basic data processing.

This grant has also benefitted Evan Lindroth, a senior undergraduate in the Geology Department at the University of Illinois working with Bruce Rhoads. Mr. Lindroth is using results from this research grant to write his senior thesis and obtain valuable experience for future graduate level studies. Another undergraduate student, David Litwin in the Civil and Environmental Engineering Department at the University of Illinois, has indirectly benefitted from this project. Mr. Litwin obtained experience with LSPIV methods and UAS operation and applications while working as a research assistant for Bruce

Rhoads over the summer of 2016. During the summer of 2017, Mr. Litwin will be a summer research assistant at the University of Arizona.

Publications

Results from studies supported by this research grant will result in scholarly publication. Two publications are in preparation focused on: 1) the utility of UAS in comparison to fixed camera setups for obtaining LSPIV mean velocity and flow structure ("Large-Scale Particle Image Velocimetry for Mean and Instantaneous Flow Structure in Rivers: Comparisons Among Fixed and UAS Cameras"); and 2) how LSPIV from UAS and fixed camera setups can be used to more thoroughly study flow fields at stream confluences ("An Assessment of Stream Confluence Flow Dynamics using mixed LSPIV and In-stream Flow Measurement Techniques"). These papers are expected to be submitted for publication within a few months from this report's date (April 2017).

In addition, work led partly by Evan Lindroth is expected to be formed into a manuscript for publication in an applied river-science journal. This paper details the use of UAS for obtaining "on the fly" discharge measurements at bridges at a variety of field sites and flow levels. The challenges and opportunities of this method will be assessed, especially with respect to mounting a camera to a tripod. LSPIV velocities and subsequent discharges will be compared to simultaneous in-stream measurements at each site to assess the robustness and accuracy of these methods. An important contribution of this work is to create a set of procedures and recommendations for rapidly obtaining accurate discharges in the field without significant pre-measurement site preparation using UAS.

Finally, UAS data will be used to supplement Quinn Lewis' dissertation, and imagery and/or data obtained with the UAS will likely be included in subsequent manuscripts derived from this work. This additional work includes collaboration with a research group at the University of Iowa responsible for numerical modeling at the study confluences, from which further publications should result.

Information Transfer Program Introduction

None.

Technology Transfer to the People of Illinois

Basic Information

Title:	Technology Transfer to the People of Illinois
Project Number:	2016IL315B
Start Date:	3/1/2016
End Date:	2/28/2017
Funding Source:	104B
Congressional District:	IL-15
Research Category:	Not Applicable
Focus Category:	None, None, None
Descriptors:	None
Principal Investigators:	Lisa Merrifield

Publications

There are no publications.

Illinois Water Resources Center

Technology Transfer Report

- The Illinois Water Resources Center staff played a key role in writing, developing, filming, producing, and promoting a video series, “Planting for Pollinators” from inception to completion. The Planting for Pollinators series is a video series that contains seven short episodes that covers the basics of planting a pollinator friendly garden that is also environmentally friendly and promotes healthy water quality of the local rivers, lakes, and streams.
- The IWRC staff coordinated and facilitated 30 meetings for the Illinois Nutrient Loss Reduction Strategy and was key in managing the various working groups: Policy Working Group, Agricultural Water Quality Partnership Forum, Agricultural Water Quality Partnership Forum Tech Subgroup, Nutrient Monitoring Council, Urban Stormwater Working Group, and the Performance Benchmark Committee. The IWRC also provided ArcGIS maps and meeting minutes for all of the Illinois Nutrient Loss Reduction strategy meetings or where needed. The NLRS groups spend much of the year finalizing their respective performance measures to track implementation. IWRC is facilitating the meeting and gathering this information for a biennial report that will be released in 2017.
- IWRC staff also gave a presentation on the Nutrient Loss Reduction Strategy at the Illinois State Fair.
- IWRC staff were a joint recipients of the Team Award for Excellence from the University of Illinois College of Agricultural, Consumer, and Environmental Sciences for the Illinois Nutrient Loss Reduction and Science Assessment Team.
- IWRC planned, facilitated, coordinated, and provided logistical support for the bi-annual Illinois Water Conference in Urbana, IL.
- IWRC has been providing multimedia content for the Private Well Class, a flagship national 10-week educational email course for private well owners. Content provided includes the Private Well Podcast, well care videos, live webinars once a month with Q & A that feature a variety of topics, social media via Facebook and Twitter, and other resources.
- IWRC staff from the Private Well Class presented 4-hour Environmental Health Professional Workshop trainings for Continuing Education Credits in Oregon, Virginia, Massachusetts, Connecticut, Illinois, Tennessee, and online (3). IWRC staff was also representing the Private Well Class at the Tribal Lands and Environment Forum in Connecticut, where they also gave a presentation on their program.
- IWRC participates in multiple awareness weeks – including Groundwater Awareness Week, National Drinking Water Week, and more. We host a yearly Pledge to Test campaign where well owners pledge to test their well water and one is randomly selected to receive the cost of well water testing paid for, up to $200.
- The Illinois State Water Survey, in collaboration with the Illinois Water Resources Center and Rural Community Assistance Partnership and with funding from the U.S. Environmental Protection Agency, manages two national community outreach programs focused on providing the

information and tools needed to protect drinking and source water quality in rural areas. The web-based Private Well Class offers groundwater science education and technical assistance for well owners, realtors, and others interested in well care best practices. WaterOperator.org is a mobile-friendly web portal with free, comprehensive resources tailored for small community and tribal water and wastewater operators.

- Since 2012, more than 6,000 homeowners and environmental health professionals in all 50 states, the District of Columbia, Puerto Rico, and Guam, including more than 1000 in Illinois, have received free online training to improve understanding of proper well care and ensure their private water source remains safe to drink. The Private Well Class has also been adopted by public health agencies across the country as their primary public education tool for private well owners. Roughly 49,000 users since 2009 also have accessed online education resources at WaterOperator.org to provide safe, compliant drinking water and sustainability operate their public water system. This includes individuals from more than 400 Illinois communities.
- The IWRC team leads the communication effort, serving dual functions of marketing the programs and developing new content for their respective audiences. At the beginning of 2016 both programs received upgraded, mobile-responsive websites designed by IWRC. Between March 2016 and February 2017, IWRC facilitated 12 webinars for environmental health professionals and homeowners on private well topics, as well as a series of 4-hour workshops (online and in-person) on outreach best practices and use of an assessment tool. Twelve monthly newsletters and 14 blog posts, both geared towards the professional audience that serves well owners, were also developed and distributed by IWRC during this reporting period. Additionally, IWRC published 48 newsletters and 38 blog posts at WaterOperator.org on public water supply and wastewater issues.
- IWRC conducted stormwater/Green Infrastructure activities included several speaking engagements that reached nearly 200 people including key community decision makers and youth.
    - 10: Common Place Peoria (2/29/16)
    - 39: 4G STEM Camp (6/24/16)
    - 58: Greater Egypt Regional Planning Commission Stormwater Training (7/20/16)
    - 20 or so listening: Illinois State Fair (8/13/16)
    - 40: CU Sunshine Rotary (9/8/16)
    - 37: Master Naturalist Urban Systems Training (10/18/16)

USGS Summer Intern Program

None.

Student Support					
Category	**Section 104 Base Grant**	**Section 104 NCGP Award**	**NIWR-USGS Internship**	**Supplemental Awards**	**Total**
Undergraduate	15	2	0	0	17
Masters	5	1	0	0	6
Ph.D.	2	2	1	0	5
Post-Doc.	0	0	0	0	0
Total	22	5	1	0	28

Notable Awards and Achievements

Since 2012, more than 6,000 homeowners and environmental health professionals in all 50 states, the District of Columbia, Puerto Rico, and Guam, including more than 1000 in Illinois, have received free online training to improve understanding of proper well care and ensure their private water source remains safe to drink. The Private Well Class has also been adopted by public health agencies across the country as their primary public education tool for private well owners. Roughly 49,000 users since 2009 also have accessed online education resources at WaterOperator.org to provide safe, compliant drinking water and sustainability operate their public water system. This includes individuals from more than 400 Illinois communities.

Michael Lydy's 104G project offers compelling evidence that pyrethroid contamination is an important source of toxicity to sediments-dwelling organism in urban streams.

Bruce Rhoads and Quinn Lewis, University of Illinois, found that Large-Scale Particle Image Velocimetry velocity fields are an important complement to traditional river flow velocity measurements especially in complex flows, and cameras deployed both in fixed and UAS configurations can yield rapid, accurate mean flow and discharge measurements in a variety of field conditions.

Publications from Prior Years

1. 2015IL296B ("Modeling and prediction of watershed-scale dynamics of consumptive water reuse for power plant cooling") - Articles in Refereed Scientific Journals - Barker, Zachary A. and Ashlynn S. Stillwell, 2016, “Implications of Transitioning from De Facto to Engineered Water Reuse for Power Plant Cooling,” Environmental Science & Technology. 50(10), 5379-5388. doi:10.1021/acs.est.5b05753